



UNIVERSITÀ DEGLI STUDI DI NAPOLI
FEDERICO II



UNIVERSITÀ DEGLI STUDI DI NAPOLI FEDERICO II

PH.D. THESIS

IN

INFORMATION TECHNOLOGY AND ELECTRICAL ENGINEERING

**BASIS OF SURFACE MODES FOR THE
SCATTERING FROM PENETRABLE OBJECTS**

GIOVANNI GRAVINA

TUTOR: PROF. CARLO FORESTIERE

COORDINATOR: PROF. DANIELE RICCIO

XXXIV CICLO

**SCUOLA POLITECNICA E DELLE SCIENZE DI BASE
DIPARTIMENTO DI INGEGNERIA ELETTRICA E TECNOLOGIE DELL'INFORMAZIONE**

Alla mia famiglia

Abstract

The analysis and design of electromagnetic scattering from a collection of mutually coupled dielectric objects is of great importance for many applications, ranging from antenna arrays to metasurfaces and metalens [1]. In this context, the use of integral formulations is appealing since the unknowns are defined only within the object's volume or - if the object is spatially piecewise homogeneous - on its boundary and internal interfaces by recurring to the surface equivalence theorems. In addition, no extra effort is required to model open boundary conditions, and radiation conditions at infinity are automatically satisfied. Nevertheless, the corresponding discrete problem is characterized by dense matrices, and their inversion is usually associated with high computational burden, even when acceleration techniques [2] like fast multipole algorithms are implemented.

Accurate and efficient solutions of integral formulations heavily depends on the choice of basis functions. Two broad categories of basis functions may be identified: *sub-domain* functions, which are non-zero only over a portion of the object, or *entire-domain* functions, which extend over the entire domain of one or few individual objects. Although the former approach may have a wider applicability, and is arguably more robust when dealing with objects of irregular shape and sharp corners, the latter is very appealing when multiple scattering problems are considered, where the electromagnetic system under investigation is a collection of mutually-coupled identical objects [3, 4].

Representative examples of sub-domain functions are those involved in the finite element method and discontinuous Galerkin method [5]: for instance the Rao-Wilton-Glisson rooftop functions [6], loop-star functions [7, 8, 9, 10], loop-tree functions [11], Trintinalia-Ling functions [12], Buffa-Christiansen functions [13], higher order vector basis functions of the Nedelec type [14], etc..

Dually, classic examples of entire-domain basis functions are the vector spherical wave functions ([15]), vector spheroidal wave functions [16]. A first strategy to generate analytic entire domain basis function is by exploiting coordinate systems where the Helmholtz equation is separable. In particular, it has been observed that this

equation can be solved by separation of variables in eleven coordinate systems [17]. A different but effective strategy to generate entire domain basis function even in irregular domains is by introducing a convenient auxiliary eigenvalue problem. A possible example is represented by the characteristic modes [18, 19, 20, 21], (see [3, 4] for arrays of perfectly conductive particles and [22] for metal metasurfaces). The characteristic modes do not depend on the particular excitation conditions and they are effective to describe the electromagnetic scattering from collections of identical objects of given material at a fixed operating frequency. Nevertheless, characteristic modes do depend on the frequency, and their interesting properties are lost if they are used as a basis at a frequency different from the one at which they are computed. Thus, they may not be the best choice when multiple frequencies are involved since they have to be recalculated at each frequency. The goal of this thesis is to look for different basis sets that can simplify the numerical solution of electromagnetic scattering problems from a given object at multiple frequencies and give physical insights.

In particular, we follow two approaches. In Chapter 4 we introduce longitudinal and transverse static surface modes and use them to solve the surface integral equation governing the full-wave electromagnetic scattering from penetrable objects. The longitudinal modes are the eigenmodes with zero surface curl of the electrostatic surface integral operator, which gives the scalar potential as a function of the surface charge density. The transverse modes are the eigenmodes with zero surface divergence of the magnetostatic surface integral operator, which returns the vector potential as a function of the surface current distribution. These modes are orthogonal. The static modes only depends on the shape of the object, thus, the same static basis can be used regardless of the frequency of operation and of the material constituting the object. We expand the unknown surface currents of the Poggio-Miller-Chang-Harrington-Wu-Tsai surface integral equations in terms of the static surface modes and solve them using the Galerkin-projection scheme. The introduced expansion allows the regularization of the singular integral operators and yields a drastic reduction of the number of unknowns compared to a discretization based on standard sub-domain basis functions.

In Chapter 5 we examine the electromagnetic modes and the resonances of homogeneous, finite size, two-dimensional bodies in the frequency domain by a rigorous full wave approach based on an integro-differential formulation of the electromagnetic scattering problem. Using a modal expansion for the current density that disentangles the geometric and material properties of the body the integro-differential equation for the induced surface (free or polarization) current density field is solved.

The current modes and the corresponding resonant values of the surface conductivity (eigen-conductivities) are evaluated by solving a linear eigenvalue problem with a non-Hermitian operator. They are inherent properties of the body geometry and do not depend on the body material. The material only determines the coefficients of the expansion and hence the frequencies at which their amplitudes are maximum (resonance frequencies). The eigen-conductivities and the current modes are studied in detail as the frequency, the shape and the size of the body vary. Open and closed surfaces are considered. The presence of vortex current modes, in addition to the source-sink current modes (no whirling modes), which characterize plasmonic oscillations, is shown. Important topological features of the current modes, such as the number of sources and sinks, the number of vortices, the direction of the vortices are preserved as the size of the body and the frequency vary. Unlike the source-sink current modes, in open surfaces the vortex current modes can be resonantly excited only in materials with positive imaginary part of the surface conductivity. Eventually, as examples, the scattering by two-dimensional bodies with either positive or negative imaginary part of the surface conductivity is analyzed and the contributions of the different modes are examined.

Author's main contribution

I gave a fundamental contributor to the

- study of the electromagnetic modes and resonances of two-dimensional bodies, which resulted in the publication of Ref. [23]
- use of the static surface mode expansion for the full-wave scattering from penetrable objects, which resulted in the preprint [24] (submitted to IEEE transactions to Antenna and Propagation)

Contents

1	Introduction to nano-optics	1
2	Formulation	3
2.1	Maxwell's Equation	3
2.1.1	Constitutive relations	4
2.1.2	Interface conditions	6
2.2	Electromagnetic Potentials	6
2.2.1	Vector Potential and Scalar Potential	7
2.2.2	Gauge fixing	7
2.2.3	Mixed Potential Formulas	9
2.3	Surface Integral Equation	9
2.3.1	A brief introduction to SIE	9
2.3.2	Scattering Problem	11
2.3.3	Equivalent formulations	11
2.3.4	Electromagnetic field generated by surface sources	12
2.3.5	Surface Integral Equation	14
3	Discretization	21
3.1	RWG Basis Function	21
3.1.1	Finite-dimensional operators	22
3.2	Loop-Star Basis Function	25
3.2.1	Loop basis functions	26
3.2.2	Star basis functions	26
4	Static surface mode expansion	28
4.1	Static current modes	29
4.1.1	Helmholtz decomposition	30
4.1.2	Static longitudinal current modes	30
4.1.3	Static transverse current modes	31

4.2	Poggio-Miller-Chang-Harrington-Wu-Tsai (PMCHWT) surface integral equation	33
4.3	Finite Element Method	35
4.3.1	Numerical generation of the static basis	35
4.3.2	Solution of the PMCWHT surface integral equation	37
4.3.3	Static - Dynamic Green Decomposition	38
4.3.4	Low-frequency analysis	42
4.4	Results and Discussion	44
4.4.1	Scattering from a sphere	44
4.4.2	Rod	49
4.5	Conclusions	55
5	Electromagnetic modes of 2d objects	57
5.1	Motivations	58
5.2	Electromagnetic scattering by two-dimensional objects	61
5.3	Mathematical model	62
5.4	Auxiliary eigenvalue problem	63
5.4.1	Properties	64
5.4.2	Frequency picture and material picture	66
5.5	Results and discussion	67
5.5.1	Source-sink current modes	68
5.5.2	Vortex current modes	68
5.6	Current modes and eigen-conductivities of open surfaces	68
5.6.1	Circle	69
5.6.2	Equilateral triangle	72
5.7	Current modes and eigen-conductivities for a closed surface	79
5.8	Scattering from 2D object and resonant conditions	81
5.8.1	Disk with negative imaginary part of the surface conductivity	82
5.8.2	Disk with positive imaginary part of the surface conductivity	84
5.9	Conclusions	86
A	Galerkin Theory	87
A.1	Hilbert Spaces	87
A.1.1	Hilbert Projection Theorem	88
A.2	Sobolev Space	88
A.2.1	Weak Derivative	89
A.2.2	Sobolev Norm	89
A.3	Galerkin Theory	90

A.3.1	Formulation of Variational Problems	90
A.3.2	Matrix form of Galerkin's equation	91

Chapter 1

Introduction to nano-optics

Over the last decades, particular interest has been raised by the resonant electromagnetic scattering from metal and dielectric nanostructures.

Metal nanostructures can support coherent oscillations of their free electron plasma, known as localized surface plasmons, which generate a high electric field-enhancement [25, 26]. This property makes them particularly effective in light concentration into deep-subwavelength volumes, enabling the boosting of linear and nonlinear optical processes [27]. This fact stimulates a variety of potential applications, including high-sensitivity biosensors [28], nonlinear optics [29], and energy harvesting [30, 31]. Furthermore, due to their control capabilities of electromagnetic fields at the nanoscale, metals are largely employed in electromagnetic metamaterials, i.e., aggregates of elementary deep-subwavelength units arranged in repeating patterns to provide an unconventional electromagnetic response [32, 33, 34], for a plethora of applications, including cloaking devices [35, 36, 37], analog optical computing [38, 39, 40], super-resolution imaging [41, 42, 43, 44]. However, the available metals for these applications, mostly noble metals (e.g., gold and silver), are plagued by high losses at the optical frequencies, inhibiting the development of practical devices [45].

Recently, dielectric resonators are gaining increasing attention in nanotechnology, and many researchers currently suggest that high-index dielectrics may be a feasible alternative to noble metals for many applications [46, 47, 48, 49, 50]. This interest has been prompted by the evidence that the enhancement of electric and magnetic fields in dielectric nanostructures is of the same order of magnitude of the one achievable in their metal counterparts. Dielectric objects of small dimensions compared to the free-space wavelength, in fact, may display a resonant behavior, provided their dielectric permittivity is sufficiently high [51, 52, 53]. This fact is well known at radio frequencies, where low-loss dielectrics with high (≈ 100) relative dielectric permittivity are exploited in several applications, such as resonators and filters [54, 55, 56],

while a series of perovskites has been measured at a relative permittivity larger than 1000 [57, 58, 59]. In the visible and near-infrared frequency ranges of the spectrum, resonances in high-index nanostructures, such as AlGaAs, Si, and Ge nanoparticles, have been experimentally observed, e.g., [60, 61, 49], and have been employed in various applications, e.g., [62, 63, 64, 65, 66, 67, 68]. In the nano-optics community, these resonances are known as “Mie resonances” [49]. The physics governing the scattering from high index dielectric nanoparticles is far richer than the physics behind the scattering from metal nanoparticles, due to the possibility of exciting magnetic modes [61, 60, 69, 70] and due to the presence of multimode interference, which may lead to the formation of Fano-resonances [71, 72].

Chapter 2

Formulation

2.1 Maxwell's Equation

The EM field is governed by Maxwell's equations. This set of coupled partial differential equations describes how electric and magnetic fields are generated by charges, currents and changes of the fields themselves.

$$\left\{ \begin{array}{l} \nabla \times \mathbf{E} = -i\omega\mu\mathbf{H} - \mathbf{J}^m \\ \nabla \times \mathbf{H} = +i\omega\varepsilon\mathbf{E} + \mathbf{J}^e \\ \nabla \cdot (\varepsilon\mathbf{E}) = \rho^e \\ \nabla \cdot (\mu\mathbf{H}) = \rho^m \end{array} \right. \quad (2.1)$$

where

- \mathbf{E} is the electric field
- \mathbf{H} is the magnetic field
- \mathbf{J}^e is the electric current density
- \mathbf{J}^m is the magnetic current density
- ρ^e is the electric charge density
- ρ^m is the magnetic charge density

Although magnetic source do not exist, their introduction to Maxwell's equations provides a useful mathematical tool. The electric and magnetic fields are coupled and the strength of coupling depends on the frequency. While the frequency approaches

zero ($\omega \rightarrow 0$) Maxwell's equations become

$$\begin{cases} \nabla \times \mathbf{E} = -\mathbf{J}^m \\ \nabla \times \mathbf{H} = +\mathbf{J}^e \\ \nabla \cdot (\varepsilon \mathbf{E}) = \rho^e \\ \nabla \cdot (\mu \mathbf{H}) = \rho^m \end{cases} \quad (2.2)$$

and the electric and magnetic fields are completely decoupled so they can be solved for independently (static fields). From Maxwell's equations it is possible to derive charge conservation expressed as continuity equations.

$$\nabla \cdot \mathbf{J}^e = -i\omega\rho^e \quad (2.3)$$

$$\nabla \cdot \mathbf{J}^m = -i\omega\rho^m \quad (2.4)$$

2.1.1 Constitutive relations

Maxwell equations involve a number of unknowns larger than the number of equations, so further information is needed to determine the solution. This is provided by the following constitutive relations that describe interaction of fields and matter from a macroscopic viewpoint

$$\begin{cases} \mathbf{d}(\mathbf{r}, t) = \mathcal{D}(\mathbf{e}(\mathbf{r}, t), \mathbf{h}(\mathbf{r}, t)) \\ \mathbf{b}(\mathbf{r}, t) = \mathcal{B}(\mathbf{e}(\mathbf{r}, t), \mathbf{h}(\mathbf{r}, t)) \\ \mathbf{j}(\mathbf{r}, t) = \mathcal{J}(\mathbf{e}(\mathbf{r}, t), \mathbf{h}(\mathbf{r}, t)) \end{cases} \quad (2.5)$$

where

- $\mathbf{d}(\mathbf{r}, t)$ is the electric induction
- $\mathbf{b}(\mathbf{r}, t)$ is the magnetic induction
- $\mathbf{j}(\mathbf{r}, t)$ is the electric induced current
- $\mathcal{D}(\cdot), \mathcal{B}(\cdot), \mathcal{J}(\cdot)$ are functionals which depend upon the medium and the fields.

These material equations are considerably simplified in cases of interest. First of all for all means that are not-bianisotropic, it is possible to consider as follows

$$\begin{cases} \mathbf{d}(\mathbf{r}, t) = \mathcal{D}(\mathbf{e}(\mathbf{r}, t)) \\ \mathbf{b}(\mathbf{r}, t) = \mathcal{B}(\mathbf{h}(\mathbf{r}, t)) \\ \mathbf{j}(\mathbf{r}, t) = \mathcal{J}(\mathbf{e}(\mathbf{r}, t)) \end{cases} \quad (2.6)$$

The most general relationship for a casual, linear (linear combination of inputs produces the same linear combination of corresponding outputs), continuous (the output depends continuously on the input) system is the following

$$\mathbf{O}(\mathbf{r}, t) = \int_{-\infty}^{+\infty} \int_{-\infty}^{+\infty} \underline{\underline{g}}(\mathbf{r}, \mathbf{r}', t, t') \mathbf{I}(\mathbf{r}', t') dV' dt' \quad (2.7)$$

where $\underline{\underline{g}}(\mathbf{r}, \mathbf{r}', t, t')$ is the Green's function and depends on the features of the medium. For a normal medium (time homogeneous, non-dispersive in space, isotropic), the Green's function is simplified as follows

$$\underline{\underline{g}}(\mathbf{r}, \mathbf{r}', t, t') = g(\mathbf{r}, t - t') \delta(\mathbf{r} - \mathbf{r}') \underline{\underline{I}} \quad (2.8)$$

Electric and magnetic induction fields can be written as

$$\mathbf{d}(\mathbf{r}, t) = \int_{-\infty}^{+\infty} \int_{-\infty}^{+\infty} g_{\varepsilon}(\mathbf{r}, t - t') \mathbf{e}(\mathbf{r}', t') \delta(\mathbf{r} - \mathbf{r}') dV' dt' \quad (2.9)$$

$$\mathbf{d}(\mathbf{r}, t) = \int_{-\infty}^{+\infty} g_{\varepsilon}(\mathbf{r}, t - t') \mathbf{e}(\mathbf{r}, t') dt' \quad (2.10)$$

$$\mathbf{b}(\mathbf{r}, t) = \int_{-\infty}^{+\infty} \int_{-\infty}^{+\infty} g_{\mu}(\mathbf{r}, t - t') \mathbf{h}(\mathbf{r}', t') \delta(\mathbf{r} - \mathbf{r}') dV' dt' \quad (2.11)$$

$$\mathbf{b}(\mathbf{r}, t) = \int_{-\infty}^{+\infty} g_{\mu}(\mathbf{r}, t - t') \mathbf{h}(\mathbf{r}, t') dt' \quad (2.12)$$

As a result of this and by exploiting the convolution theorem, relative electric permittivity and relative magnetic permeability show to be the Fourier transform of Green's function g_{ε} e g_{μ}

$$\begin{cases} \varepsilon(\mathbf{r}, \omega) = \mathcal{F}\{g_{\varepsilon}(\mathbf{r}, t)\} \\ \mu(\mathbf{r}, \omega) = \mathcal{F}\{g_{\mu}(\mathbf{r}, t)\} \end{cases} \quad (2.13)$$

so we will be concerned with relationship of the sort

$$\mathbf{D}(\mathbf{r}, \omega) = \varepsilon_0 \varepsilon(\mathbf{r}, \omega) \mathbf{E}(\mathbf{r}, \omega) \quad (2.14)$$

and, similarly, for the magnetic field

$$\mathbf{B}(\mathbf{r}, \omega) = \mu_0 \mu(\mathbf{r}, \omega) \mathbf{H}(\mathbf{r}, \omega) \quad (2.15)$$

It is important to note that permittivity and permeability are ruled by Kramers-Kronig relations

$$\chi_1(\omega) = +\frac{1}{\pi} \text{p.v.} \int_{-\infty}^{+\infty} \frac{\chi_2(\omega')}{\omega' - \omega} d\omega' \quad (2.16)$$

$$\chi_2(\omega) = -\frac{1}{\pi} \text{p.v.} \int_{-\infty}^{+\infty} \frac{\chi_1(\omega')}{\omega' - \omega} d\omega' \quad (2.17)$$

which link real and imaginary parts of any complex function $\chi(\omega) = \chi_1(\omega) + i\chi_2(\omega)$ that is analytic (p.v. denotes the Cauchy principal value). Since Analyticity implies causality (as can be easily demonstrated using Titchmarsh's Theorem), if the real and imaginary parts of such a function adhere to Kramers-Kronig relations, the causality principle is fulfilled.

2.1.2 Interface conditions

Differential-form Maxwell's equations cannot be applied to discontinuous fields that may occur at interfaces between different media. In order to fulfill this purpose, integral-form Maxwell's equations can be employed to find the relations between the fields \mathbf{E} , \mathbf{H} , \mathbf{D} and \mathbf{B} on the two sides of an interface.

$$\text{Normal interface conditions} \begin{cases} (\mathbf{D}_1 - \mathbf{D}_2) \cdot \hat{\mathbf{n}} = \rho^e \\ (\mathbf{B}_1 - \mathbf{B}_2) \cdot \hat{\mathbf{n}} = \rho^m \end{cases} \quad (2.18)$$

$$\text{Tangential interface conditions} \begin{cases} \hat{\mathbf{n}} \times (\mathbf{H}_1 - \mathbf{H}_2) = +\mathbf{J}^e \\ \hat{\mathbf{n}} \times (\mathbf{E}_1 - \mathbf{E}_2) = -\mathbf{J}^m \end{cases} \quad (2.19)$$

where the subscripts 1 and 2 represent the medium 1 and medium 2, respectively, and $\hat{\mathbf{n}}$ is the unit normal vector on the boundary and is pointing from medium 2 to medium 1. In many cases of interest, Interface conditions can be customized. In particular, when the medium 2 is a perfect electric conductor, the electromagnetic fields have to satisfy the following boundary conditions

$$\text{Normal interface conditions} \begin{cases} \mathbf{D} \cdot \hat{\mathbf{n}} = \rho^e \\ \mathbf{B} \cdot \hat{\mathbf{n}} = 0 \end{cases} \quad (2.20)$$

$$\text{Tangential interface conditions} \begin{cases} \hat{\mathbf{n}} \times \mathbf{H} = \mathbf{J}^e \\ \hat{\mathbf{n}} \times \mathbf{E} = \mathbf{0} \end{cases} \quad (2.21)$$

2.2 Electromagnetic Potentials

The introduction of electromagnetic potentials provides an elegant means to solve Maxwell's equations. In order to develop the potential approach, the electric and

magnetic fields are splitted as follow

$$\begin{cases} \mathbf{E}(\mathbf{r}) = \mathbf{E}^e(\mathbf{r}) + \mathbf{E}^m(\mathbf{r}) \\ \mathbf{H}(\mathbf{r}) = \mathbf{H}^e(\mathbf{r}) + \mathbf{H}^m(\mathbf{r}) \end{cases} \quad (2.22)$$

where \mathbf{E}^e , \mathbf{H}^e are due to electric sources while \mathbf{E}^m , \mathbf{H}^m are due to magnetic sources.

2.2.1 Vector Potential and Scalar Potential

By exploiting the relation

$$\nabla \cdot (\mu \mathbf{H}^e) = 0 \quad (2.23)$$

Magnetic Field \mathbf{H}^e can be written as

$$\mathbf{H}^e = +\frac{1}{\mu} \nabla \times \mathbf{A}^e \quad (2.24)$$

where \mathbf{A}^e is the Vector Potential. Consequently, the relation

$$\nabla \times (\mathbf{E}^e + i\omega \mathbf{A}^e) = \mathbf{0} \quad (2.25)$$

allows to write Electric Field as

$$\mathbf{E}^e + i\omega \mathbf{A}^e = -\nabla \Phi^e \quad (2.26)$$

where Φ^e is the Scalar Potential. Dually, fields produced from magnetic sources can be written as follow

$$\mathbf{E}^m = -\frac{1}{\varepsilon} \nabla \times \mathbf{A}^m \quad (2.27)$$

$$\mathbf{H}^m = -i\omega \mathbf{A}^m - \nabla \Phi^m \quad (2.28)$$

Summarizing, we have

$$\mathbf{E} = -i\omega \mathbf{A}^e - \nabla \Phi^e - \frac{1}{\varepsilon} \nabla \times \mathbf{A}^m \quad (2.29)$$

$$\mathbf{H} = +\frac{1}{\mu} \nabla \times \mathbf{A}^e - i\omega \mathbf{A}^m - \nabla \Phi^m \quad (2.30)$$

2.2.2 Gauge fixing

As mentioned, it is often convenient to reformulate Maxwell's equations in terms of scalar and vector potentials (\mathbf{A} , Φ). However, while the original formulation ensures under some conditions (Uniqueness Theorem) the uniqueness of the fields \mathbf{E} , \mathbf{H} , \mathbf{D} ,

B the same does not apply for potential formulation: when substituting the scalar and vector potentials into Maxwell's equations, those new equations typically have an infinite number of solutions, unless additional equations or conditions are applied. The mathematical procedure for coping with redundant degrees of freedom is called Gauge fixing. For instance, let Ψ be a scalar field, the gauge equations

$$\begin{cases} \tilde{\mathbf{A}} = \mathbf{A} - \nabla\Psi \\ \tilde{\Phi} = \Phi + i\omega\Psi \end{cases} \quad (2.31)$$

identify same fields \mathbf{E} and \mathbf{H} .

$$\tilde{\mathbf{E}} = -i\omega\tilde{\mathbf{A}}^e - \nabla\tilde{\Phi}^e - \frac{1}{\varepsilon}\nabla \times \tilde{\mathbf{A}}^m = \mathbf{E} \quad (2.32)$$

$$\tilde{\mathbf{H}} = +\frac{1}{\mu}\nabla \times \tilde{\mathbf{A}}^e - i\omega\tilde{\mathbf{A}}^m - \nabla\tilde{\Phi}^m = \mathbf{H} \quad (2.33)$$

In order to avoid this, one more condition should be imposed. The choice made in the rest (not the only one possible) is the Lorentz Gauge

$$\nabla \cdot \mathbf{A} + i\omega\varepsilon\mu\Phi = 0 \quad (2.34)$$

This gauge appears to be particularly appealing for the following reason: Maxwell's Equations with Electric Sources reduce to a vector Helmholtz equation for Vector Potential

$$\nabla^2\mathbf{A}^e + k^2\mathbf{A}^e = -\mu\mathbf{J}^e \quad (2.35)$$

and a scalar Helmholtz equation for Scalar Potential.

$$\nabla^2\Phi^e + k^2\Phi^e = -\frac{1}{\varepsilon}\rho^e \quad (2.36)$$

Clearly, the above applies only if the material properties are homogeneous. Solving these equations by convolving the Green's function the expressions for (\mathbf{A}^e, Φ^e) are derived.

$$\mathbf{A}^e(\mathbf{r}) = \mu \int_V g(\mathbf{r}, \mathbf{r}') \mathbf{J}^e(\mathbf{r}') dV' \quad (2.37)$$

$$\Phi^e(\mathbf{r}) = \frac{1}{\varepsilon} \int_V g(\mathbf{r}, \mathbf{r}') \rho^e(\mathbf{r}') dV' \quad (2.38)$$

In an absolutely dual way, the expressions for (\mathbf{A}^m, Φ^m) are obtained.

$$\mathbf{A}^m(\mathbf{r}) = \varepsilon \int_V g(\mathbf{r}, \mathbf{r}') \mathbf{J}^m(\mathbf{r}') dV' \quad (2.39)$$

$$\Phi^m(\mathbf{r}) = \frac{1}{\mu} \int_V g(\mathbf{r}, \mathbf{r}') \rho^m(\mathbf{r}') dV' \quad (2.40)$$

2.2.3 Mixed Potential Formulas

By exploiting Lorentz Gauge

$$\nabla \cdot \mathbf{A} + i\omega\varepsilon\mu\Phi = 0 \rightarrow \Phi = -\frac{1}{i\omega\varepsilon\mu} \nabla \cdot \mathbf{A} \quad (2.41)$$

it is possible to suppress the dependency on the scalar potential and to express fields as function of currents only.

$$\begin{aligned} \mathbf{E}(\mathbf{r}) &= -i\omega\mathbf{A}^e(\mathbf{r}) + \frac{1}{i\omega\varepsilon\mu} \nabla \nabla \cdot \mathbf{A}^e(\mathbf{r}) - \frac{1}{\varepsilon} \nabla \times \mathbf{A}^m(\mathbf{r}) \\ &= -i\omega \left[1 + \frac{1}{k^2} \nabla \nabla \cdot \right] \mathbf{A}^e(\mathbf{r}) - \frac{1}{\varepsilon} \nabla \times \mathbf{A}^m(\mathbf{r}) \\ &= -i\omega\mu \left[1 + \frac{1}{k^2} \nabla \nabla \cdot \right] \int_V g(\mathbf{r}, \mathbf{r}') \mathbf{J}^e(\mathbf{r}') dV' \\ &\quad - \nabla \times \int_V g(\mathbf{r}, \mathbf{r}') \mathbf{J}^e(\mathbf{r}') dV' \quad (2.42) \end{aligned}$$

Similarly, the magnetic field can be written as

$$\begin{aligned} \mathbf{H}(\mathbf{r}) &= \frac{1}{\mu} \nabla \times \mathbf{A}^e(\mathbf{r}) - i\omega\mathbf{A}^m(\mathbf{r}) + \frac{1}{i\omega\varepsilon\mu} \nabla \nabla \cdot \mathbf{A}^m(\mathbf{r}) \\ &= \frac{1}{\mu} \nabla \times \mathbf{A}^e(\mathbf{r}) - i\omega \left[1 + \frac{1}{k^2} \nabla \nabla \cdot \right] \mathbf{A}^m(\mathbf{r}) \\ &= \nabla \times \int_V g(\mathbf{r}, \mathbf{r}') \mathbf{J}^e(\mathbf{r}') dV' \\ &\quad - i\omega\varepsilon \left[1 + \frac{1}{k^2} \nabla \nabla \cdot \right] \int_V g(\mathbf{r}, \mathbf{r}') \mathbf{J}^m(\mathbf{r}') dV' \quad (2.43) \end{aligned}$$

2.3 Surface Integral Equation

2.3.1 A brief introduction to SIE

Before taking into account the SIE formulations and in order to appreciate some of its peculiarities, it is advisable to place them in a general perspective. From a general point of view, whenever an analytical solution cannot be found, the only way is to resort to a numerical technique, which yields an approximate solution. These techniques are typically divided into differential and integral methods. The former involve the discretization of a differential operator and the subsequent creation of a sparse

linear system. Typical examples include the finite difference time domain (FDTD) method (e.g [73]), or the finite element method (FEM). Since these methods require the discretization of the entire domain, they are not the best choice for all those problems (e.g. scattering and radiation problems) where the domain is unbounded. In contrast, the latter, a typical example of which is Integral equation based methods, only require the discretization of the scatterer or the antenna, respectively. Because of their inherent capability to model unbounded domains, Integral-Equation methods are particularly favourable for exterior open-region scattering problems (such as the one considered in the current work). In addition, in all cases where it is possible to exploit the homogeneity of the object, it is possible to have a further reduction in computational effort, by only discretizing the surface and composing a Surface Integral Equation. The main drawback of this second category is that the emerging linear system is dense. Given the computational resources available in the last century, the high computational complexity with respect to the number of freedom has been one of the main reasons why integral equations have not been heavily employed by the scientific community for a long time. It is only with the advent of fast methods that this position has been revalued. For instance, we can consider the Multilevel Fast Multipole Algorithm (MLFMA) which allows to have a computational effort of $N \log N$ with regard to memory and solution time, as opposed to N^2 and N^3 of traditional non-fast methods. There are several formulations that can be used for the same problem and this raises the question of the most-optimal one. It should be noted that in almost all cases of practical interest, iterative methods are used to obtain the solution of the linear system. The consequence of this is the need to deal with convergence issue of the iterative algorithm. The requirement to solve this in parallel with the bad-conditioning problems results in another distinctive feature of these formulations: the integral-equation formulation and the numerical-discretization procedure have to be properly coupled. Before looking in detail at some of the most popular SIE formulations, the steps common to all of them are outlined below

- Pre-processing: Geometrical and material modeling
- Formulation: Formulation of the boundary-value problems as equivalent surface integral equations
- Discretization: Transformation of the continuous integral equations to discrete matrix equations
- Solution: Resolution of the matrix equations
- Post-processing: Visualization and parameter computation

2.3.2 Scattering Problem

Let us consider a linear, non-magnetic, homogeneous, and isotropic object with permittivity and permeability (ε_i, μ_i) embedded in a homogeneous lossless medium with permittivity and permeability (ε_e, μ_e) . The inner and outer regions (indicated with V_i and V_e) are separated by a boundary surface S , with a versor \mathbf{n} directed towards V_e . We assume that the regions V_i and V_e contain the impressed electric sources \mathbf{J}_i^0 and \mathbf{J}_e^0 , respectively. The electromagnetic fields are solution of the problem

$$\begin{cases} \nabla \times \mathbf{E}_\ell &= -i\omega\mu_\ell\mathbf{H}_\ell \\ \nabla \times \mathbf{H}_\ell &= +i\omega\varepsilon_\ell\mathbf{E}_\ell + \mathbf{J}_\ell^0 \end{cases} \text{ in } V_\ell \quad \text{with } \ell = i, e \quad (2.44)$$

with the boundary condition

$$\begin{cases} \mathbf{n} \times (\mathbf{H}_i - \mathbf{H}_e) &= \mathbf{0} \\ \mathbf{n} \times (\mathbf{E}_i - \mathbf{E}_e) &= \mathbf{0} \end{cases} \text{ on } S \quad (2.45)$$

with the radiation condition at infinity. Let $(\mathbf{E}_\ell^{(0)}, \mathbf{H}_\ell^{(0)})$ be the electromagnetic field radiated by the current distribution $\mathbf{J}_\ell^{(0)}$ in the homogeneous medium with parameters $(\varepsilon_\ell, \mu_\ell)$. The scattered electromagnetic fields $(\mathbf{E}_\ell^{(S)}, \mathbf{H}_\ell^{(S)})$ are defined as

$$\begin{cases} \mathbf{E}_\ell^{(S)} &= \mathbf{E}_\ell - \mathbf{E}_\ell^{(0)} \\ \mathbf{H}_\ell^{(S)} &= \mathbf{H}_\ell - \mathbf{H}_\ell^{(0)} \end{cases} \text{ in } V_\ell \quad \text{with } \ell = i, e \quad (2.46)$$

and are solution of the problem:

$$\begin{cases} \nabla \times \mathbf{E}_\ell^{(S)} &= -i\omega\mu_\ell\mathbf{H}_\ell^{(S)} \\ \nabla \times \mathbf{H}_\ell^{(S)} &= i\omega\varepsilon_\ell\mathbf{E}_\ell^{(S)} \end{cases} \text{ in } V_\ell \quad \text{with } \ell = i, e, \quad (2.47)$$

$$\begin{cases} \mathbf{n} \times (\mathbf{H}_e^{(S)} - \mathbf{H}_i^{(S)}) &= -\mathbf{n} \times (\mathbf{H}_e^{(0)} - \mathbf{H}_i^{(0)}) \\ \mathbf{n} \times (\mathbf{E}_e^{(S)} - \mathbf{E}_i^{(S)}) &= -\mathbf{n} \times (\mathbf{E}_e^{(0)} - \mathbf{E}_i^{(0)}) \end{cases} \text{ on } S. \quad (2.48)$$

2.3.3 Equivalent formulations

In the case of EM wave scattering from an homogeneous scatterer, the surface equivalence principle [74] can be applied to simplify the problem. By this principle, the discontinuity is replaced by equivalent sources distributed on the surface that separate the two environments. Before applying the equivalent principle, we remind the expression of the electromagnetic field radiated by a surface current density distributions radiating in an homogeneous space.

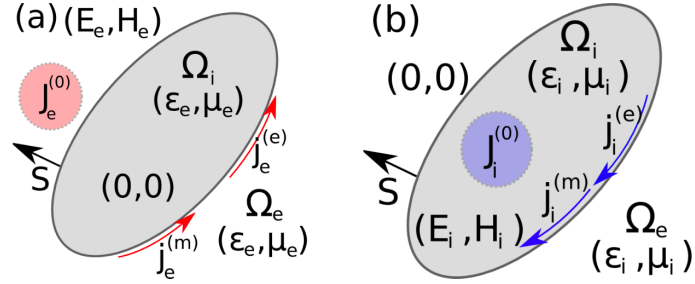


Figure 2.1 – An illustration of the Love principle. Equivalence for the external (a) and the internal (b) problems

2.3.4 Electromagnetic field generated by surface sources

The electromagnetic field $(\mathbf{E}_\ell, \mathbf{H}_\ell)$ generated by a surface distribution of electric and magnetic currents $(\mathbf{J}^e, \mathbf{J}^m)$ defined on S and radiating in a homogeneous medium with constitutive parameters $(\epsilon_\ell, \mu_\ell)$ is given by:

$$\mathbf{E}_\ell(\mathbf{r}) = \mathcal{E}_\ell \{ \mathbf{J}^e, \mathbf{J}^m \}(\mathbf{r}) \quad (2.49a)$$

$$\mathbf{H}_\ell(\mathbf{r}) = \mathcal{H}_\ell \{ \mathbf{J}^e, \mathbf{J}^m \}(\mathbf{r}) \quad (2.49b)$$

where:

$$\begin{aligned} \mathcal{E}_\ell \{ \mathbf{J}^e, \mathbf{J}^m \}(\mathbf{r}) = & \zeta_\ell \mathcal{T}_\ell \{ \mathbf{J}^e \}(\mathbf{r}) + \mathcal{K}_\ell \{ \mathbf{J}^m \}(\mathbf{r}) + \\ & + \begin{cases} \mathbf{0} & \text{if } \mathbf{r} \notin S \\ +\frac{\zeta_\ell}{2ik_\ell} [\nabla_S \cdot \mathbf{J}^e(\mathbf{r})] \mathbf{n} - \frac{1}{2} \mathbf{n} \times \mathbf{J}^m(\mathbf{r}) & \text{if } \mathbf{r} \in S_i, \\ -\frac{\zeta_\ell}{2ik_\ell} [\nabla_S \cdot \mathbf{J}^e(\mathbf{r})] \mathbf{n} + \frac{1}{2} \mathbf{n} \times \mathbf{J}^m(\mathbf{r}) & \text{if } \mathbf{r} \in S_e \end{cases} \end{aligned} \quad (2.50)$$

$$\begin{aligned} \mathcal{H}_\ell \{ \mathbf{J}^e, \mathbf{J}^m \} (\mathbf{r}) = & -\mathcal{K}_\ell \{ \mathbf{J}^e \} (\mathbf{r}) + \frac{1}{\zeta_\ell} \mathcal{T}_\ell \{ \mathbf{J}^m \} (\mathbf{r}) + \\ & + \begin{cases} \mathbf{0} & \text{if } \mathbf{r} \notin S \\ +\frac{1}{2} \mathbf{n} \times \mathbf{J}^e (\mathbf{r}) + \frac{1}{2i\zeta_\ell k_\ell} [\nabla_S \cdot \mathbf{J}^m (\mathbf{r})] \mathbf{n} & \text{if } \mathbf{r} \in S_i, \\ -\frac{1}{2} \mathbf{n} \times \mathbf{J}^e (\mathbf{r}) - \frac{1}{2i\zeta_\ell k_\ell} [\nabla_S \cdot \mathbf{J}^m (\mathbf{r})] \mathbf{n} & \text{if } \mathbf{r} \in S_e \end{cases} \end{aligned} \quad (2.51)$$

$\nabla_S \cdot$ denotes the surface divergence, \mathcal{K}_ℓ and \mathcal{T}_ℓ denote the integral operators: two integral operators have been introduced

$$\mathcal{K}_\ell \{ \mathbf{w} \} (\mathbf{r}) = - \int_S \mathbf{w}(\mathbf{r}') \times \nabla' g_\ell(\mathbf{r} - \mathbf{r}') dS' \quad (2.52)$$

$$\mathcal{T}_\ell \{ \mathbf{w} \} (\mathbf{r}) = -ik \int_S g_\ell(\mathbf{r} - \mathbf{r}') \mathbf{w}(\mathbf{r}') dS' - \frac{1}{ik} \int_S \nabla' g_\ell(\mathbf{r} - \mathbf{r}') \nabla'_S \cdot \mathbf{w}(\mathbf{r}') dS', \quad (2.53)$$

g_ℓ is the homogeneous space Green's function of the region V_ℓ , i.e.

$$g_\ell(\mathbf{r} - \mathbf{r}') = \frac{e^{-ik_\ell |\mathbf{r} - \mathbf{r}'|}}{4\pi |\mathbf{r} - \mathbf{r}'|}, \quad (2.54)$$

$$k_\ell = \omega \sqrt{\mu_e \epsilon_e}, \text{ and } \zeta_\ell = \sqrt{\frac{\mu_\ell}{\epsilon_\ell}}.$$

Equivalence principle for the exterior medium

The region V_i is filled with the same material of the region V_e , i.e. (ϵ_e, μ_e) , and the sources in V_i are removed, as shown in Fig. 2.1 (a). Two equivalent surface currents $(\mathbf{J}_e^e, \mathbf{J}_e^m)$, positioned on the external page S_e of the surface S , produce the original scattered fields $(\mathbf{E}_e^{(S)}, \mathbf{H}_e^{(S)})$ in the region V_e and null fields in the region V_i . The fields are discontinuous across the surface S , so the surface currents $(\mathbf{J}_e^e, \mathbf{J}_e^m)$ account for these discontinuities. By the uniqueness theorem, the fields in V_e are the same of the original problem.

$$\mathcal{E}_e \{ \mathbf{J}_e^e, \mathbf{J}_e^m \} (\mathbf{r}) + \mathbf{E}_e^{(0)} (\mathbf{r}) = \begin{cases} \mathbf{0} & \text{if } \mathbf{r} \in V_i \\ \mathbf{E}_e(\mathbf{r}) & \text{if } \mathbf{r} \in V_e \end{cases} \quad (2.55)$$

$$\mathcal{H}_e \{ \mathbf{J}_e^e, \mathbf{J}_e^m \} (\mathbf{r}) + \mathbf{H}_e^{(0)} (\mathbf{r}) = \begin{cases} \mathbf{0} & \text{if } \mathbf{r} \in V_i \\ \mathbf{H}_e(\mathbf{r}) & \text{if } \mathbf{r} \in V_e \end{cases} \quad (2.56)$$

where the source $(\mathbf{J}_e^e, \mathbf{J}_e^m)$ are defined as

$$\begin{cases} \mathbf{J}_e^e = +\mathbf{n} \times \mathbf{H}_e \\ \mathbf{J}_e^m = -\mathbf{n} \times \mathbf{E}_e \end{cases} \Big|_{S_e} \quad (2.57)$$

Equivalence principle for the interior medium

In a dual formulation, the region V_e is filled up with the same material of the region V_i and the sources in V_e are removed, as shown in Fig. 2.1 (b). Two equivalent currents $(\mathbf{J}_i^e, \mathbf{J}_i^m)$, positioned on the internal page S_i of the surface S , produce the original scattered fields $(\mathbf{E}_i^{(S)}, \mathbf{H}_i^{(S)})$ in the interior region V_i and null fields in the exterior region V_e . The fields are discontinuous across the surface S , and the surface currents $(\mathbf{J}_i^e, \mathbf{J}_i^m)$ account for these discontinuities. By the uniqueness theorem, the fields in V_i are the same.

$$\mathcal{E}_i\{\mathbf{J}_i^e, \mathbf{J}_i^m\}(\mathbf{r}) + \mathbf{E}_i^{(0)}(\mathbf{r}) = \begin{cases} \mathbf{E}_i(\mathbf{r}) & \text{if } \mathbf{r} \in V_i \\ \mathbf{0} & \text{if } \mathbf{r} \in V_e \end{cases} \quad (2.58)$$

$$\mathcal{H}_i\{\mathbf{J}_i^e, \mathbf{J}_i^m\}(\mathbf{r}) + \mathbf{H}_i^{(0)}(\mathbf{r}) = \begin{cases} \mathbf{H}_i(\mathbf{r}) & \text{if } \mathbf{r} \in V_i \\ \mathbf{0} & \text{if } \mathbf{r} \in V_e \end{cases} \quad (2.59)$$

where the source $(\mathbf{J}_i^e, \mathbf{J}_i^m)$ are defined as

$$\begin{cases} \mathbf{J}_i^e = -\mathbf{n} \times \mathbf{H}_i \\ \mathbf{J}_i^m = +\mathbf{n} \times \mathbf{E}_i \end{cases} \Big|_{S_i} \quad (2.60)$$

Analyzing boundary conditions and equivalent currents definitions, $(\mathbf{J}_e^e, \mathbf{J}_e^m)$ and $(\mathbf{J}_i^e, \mathbf{J}_i^m)$ are shown to be not independent

$$\begin{cases} \mathbf{J}_i^e = -\mathbf{J}_e^e \\ \mathbf{J}_i^m = -\mathbf{J}_e^m \end{cases} \quad (2.61)$$

2.3.5 Surface Integral Equation

By using the Love's field equivalence principle, a set of surface integral equations in the unknowns $(\mathbf{J}_e^e, \mathbf{J}_e^m)$ is obtained.

Electric Field Integral Equations (EFIE)

By enforcing the ($\pi/2$ rotated) tangential interface condition of Eqs. 2.55 and 2.58, the N-Electric Field Integral Equations (N-EFIE) is obtained

$$(\text{N-EFIE})_e : \hat{\mathbf{n}} \times (+\mathcal{E}_e\{\mathbf{J}_e^e, \mathbf{J}_e^m\} + \mathbf{E}_e^{(0)}) + \mathbf{J}_e^m = \mathbf{0} \quad (2.62a)$$

$$(\text{N-EFIE})_i : \hat{\mathbf{n}} \times (-\mathcal{E}_i\{\mathbf{J}_e^e, \mathbf{J}_e^m\} + \mathbf{E}_i^{(0)}) + \mathbf{J}_e^m = \mathbf{0} \quad (2.62b)$$

By enforcing the tangential interface condition of Eqs. 2.55 and 2.58, the sets of T-Electric Field Integral Equations (T-EFIE) are obtained

$$(\text{T-EFIE})_e : -\hat{\mathbf{n}} \times \hat{\mathbf{n}} \times (+\mathcal{E}_e\{\mathbf{J}_e^e, \mathbf{J}_e^m\} + \mathbf{E}_e^{(0)}) - \hat{\mathbf{n}} \times \mathbf{J}_e^m = \mathbf{0} \quad (2.63a)$$

$$(\text{T-EFIE})_i : -\hat{\mathbf{n}} \times \hat{\mathbf{n}} \times (-\mathcal{E}_i\{\mathbf{J}_e^e, \mathbf{J}_e^m\} + \mathbf{E}_i^{(0)}) - \hat{\mathbf{n}} \times \mathbf{J}_e^m = \mathbf{0} \quad (2.63b)$$

Magnetic Field Integral Equations (MFIE)

By enforcing the ($\pi/2$ rotated) tangential interface condition of Eqs. 2.56 and 2.59, the sets of T-Magnetic Field Integral Equations (T-MFIE) are obtained

$$(\text{N-MFIE})_e : \hat{\mathbf{n}} \times (+\mathcal{H}_e\{\mathbf{J}_e^e, \mathbf{J}_e^m\} + \mathbf{H}_e^{(0)}) - \mathbf{J}_e^e = \mathbf{0} \quad (2.64a)$$

$$(\text{N-MFIE})_i : \hat{\mathbf{n}} \times (-\mathcal{H}_i\{\mathbf{J}_e^e, \mathbf{J}_e^m\} + \mathbf{H}_i^{(0)}) - \mathbf{J}_e^e = \mathbf{0} \quad (2.64b)$$

By enforcing the tangential interface condition of Eqs. 2.56 and 2.59, the sets of T-Magnetic Field Integral Equations (T-MFIE) are

$$(\text{T-MFIE})_e : -\hat{\mathbf{n}} \times \hat{\mathbf{n}} \times (+\mathcal{H}_e\{\mathbf{J}_e^e, \mathbf{J}_e^m\} + \mathbf{H}_e^{(0)}) + \hat{\mathbf{n}} \times \mathbf{J}_e^e = \mathbf{0} \quad (2.65a)$$

$$(\text{T-MFIE})_i : -\hat{\mathbf{n}} \times \hat{\mathbf{n}} \times (-\mathcal{H}_i\{\mathbf{J}_e^e, \mathbf{J}_e^m\} + \mathbf{H}_i^{(0)}) + \hat{\mathbf{n}} \times \mathbf{J}_e^e = \mathbf{0} \quad (2.65b)$$

Combined Region Integral Equations (CRIE)

Both EFIE and MFIE formulation suffer from internal resonance problems at resonance frequencies, thus they do not show a unique solution at any frequencies. In order to avoid this, an appropriate linear combination of EFIE and MFIE is required.

N-Combined Region Integral Equations (N-CRIE) A linear combination of the N-EFIE and N-MFIE equations in the inner region Ω_i and in the outer region Ω_e

leads to the N-Combined Region Integral Equations.

$$\begin{aligned} a_e(\text{N-MFIE})_e + a_i(\text{N-MFIE})_i \\ b_e(\text{N-EFIE})_e + b_i(\text{N-EFIE})_i \end{aligned} \quad (2.66)$$

By using 2.62 and 2.64 in Eq. 2.66 we obtain:

$$a_e(\mathcal{H}_e^{(n)}\{\mathbf{J}_e^e, \mathbf{J}_e^m\} + \mathbf{h}_e^{(0,n)} - \mathbf{J}_e^e) + a_i(-\mathcal{H}_i^{(n)}\{\bar{\mathbf{J}}_e^e, \mathbf{J}_e^m\} + \mathbf{h}_i^{(0,n)} - \mathbf{J}_e^e) = \mathbf{0} \quad (2.67a)$$

$$b_e(\mathcal{E}_e^{(n)}\{\mathbf{J}_e^e, \mathbf{J}_e^m\} + \mathbf{e}_e^{(0,n)} + \mathbf{J}_e^m) + b_i(-\mathcal{E}_i^{(n)}\{\mathbf{J}_e^e, \mathbf{J}_e^m\} + \mathbf{e}_i^{(0,n)} + \mathbf{J}_e^m) = \mathbf{0} \quad (2.67b)$$

where we have introduced the following operators

$$\mathcal{E}_\ell^{(n)}\{\mathbf{J}^e, \mathbf{J}^m\} = \hat{\mathbf{n}} \times \mathcal{E}_\ell\{\mathbf{J}^e, \mathbf{J}^m\} \quad (2.68)$$

$$\mathcal{H}_\ell^{(n)}\{\mathbf{J}^e, \mathbf{J}^m\} = \hat{\mathbf{n}} \times \mathcal{H}_\ell\{\mathbf{J}^e, \mathbf{J}^m\} \quad (2.69)$$

and

$$\begin{aligned} \mathbf{e}_\ell^{(0,n)} &= \hat{\mathbf{n}} \times \mathbf{E}_\ell^{(0)} \\ \mathbf{h}_\ell^{(0,n)} &= \hat{\mathbf{n}} \times \mathbf{H}_\ell^{(0)} \end{aligned} \quad (2.70)$$

The system of equations 2.66 can be recast in the compact form:

$$\mathcal{C}^{(n)} \mathbf{x} = \mathbf{y}^{(n)} \quad (2.71)$$

where we have introduced the following operator:

$$\mathcal{C}^{(n)} = \begin{vmatrix} a_e \left(\frac{1}{2} \mathcal{I} + \mathcal{K}_e^{(n)} \right) & -a_e \zeta_e^{-1} \mathcal{T}_e^{(n)} & a_i \left(\frac{1}{2} \mathcal{I} - \mathcal{K}_i^{(n)} \right) & a_i \zeta_i^{-1} \mathcal{T}_i^{(n)} \\ b_e \zeta_e \mathcal{T}_e^{(n)} & b_e \left(\frac{1}{2} \mathcal{I} + \mathcal{K}_e^{(n)} \right) & -b_i \zeta_i \mathcal{T}_i^{(n)} & b_i \left(\frac{1}{2} \mathcal{I} - \mathcal{K}_i^{(n)} \right) \end{vmatrix}, \quad (2.72)$$

the identity operator \mathcal{I} , the operators:

$$\mathcal{K}_\ell^{(n)}\{\cdot\} = \mathbf{n} \times \mathcal{K}_\ell\{\cdot\}|_{S_\ell}, \quad (2.73a)$$

$$\mathcal{T}_\ell^{(n)}\{\cdot\} = \mathbf{n} \times \mathcal{T}_\ell\{\cdot\}|_{S_\ell}. \quad (2.73b)$$

Furthermore, we have introduced the vector of unknowns:

$$\mathbf{x} = \begin{vmatrix} \mathbf{j}_e^e \\ \mathbf{j}_e^m \end{vmatrix}, \quad (2.74)$$

and the excitation vector:

$$\mathbf{y}^{(n)} = \begin{vmatrix} a_e \mathbf{h}_e^{(0,n)} + a_i \mathbf{h}_i^{(0,n)} \\ -b_e \mathbf{e}_e^{(0,n)} - b_i \mathbf{e}_i^{(0,n)} \end{vmatrix}. \quad (2.75)$$

Several surface integral equations can be derived from eq. 2.71 depending on the choice of the coefficient set $\{a_e, a_i, b_e, b_i\}$. In particular, providing that $(a_e/a_i)(b_e/b_i)^* \in \mathbb{R}_+$ the corresponding N-CRIE formulation has a unique solution at any frequency [75]. Some of the possible N-CRIE formulations are:

$$\begin{array}{ll} \text{N-PMCHWT} & (a_e = 1, a_i = -1, b_e = 1, b_i = -1); \\ \text{CNF} & (a_e = 1, a_i = 1, b_e = 1, b_i = 1); \\ \text{N-Muller} & \left(\begin{array}{ll} a_e = \mu_e(\mu_e + \mu_i)^{-1}, & a_i = \mu_i(\mu_e + \mu_i)^{-1}, \\ b_e = \epsilon_e(\epsilon_e + \epsilon_i)^{-1}, & b_i = \epsilon_i(\epsilon_e + \epsilon_i)^{-1} \end{array} \right); \\ \text{mN-Muller} & (a_e = \mu_e, a_i = \mu_i, b_e = \epsilon_e, b_i = \epsilon_i). \end{array} \quad (2.76)$$

The N-PMCHWT is very ill conditioned since the operator \mathcal{I} on the diagonal cancels. The CNF has been proven to be inaccurate in the case of objects with high permittivity contrast [76]. The N-Muller [77] and the mN-Muller [78] formulations have good performances especially when low contrast bodies are considered [79], in particular the latter one is faster when iterative solvers are used [76].

T-Combined Region Integral Equations (T-CRIE) A linear combination of the T-EFIE and T-MFIE equations in the inner region V_i and in the outer region V_e constitutes the T-Combined Region Integral Equations.

$$c_e(\text{T-EFIE})_e + c_i(\text{T-EFIE})_i \quad (2.77a)$$

$$d_e(\text{T-MFIE})_e + d_i(\text{T-MFIE})_i \quad (2.77b)$$

By using 2.63 and 2.65 in Eq. 2.78 we obtain:

$$c_e(\mathcal{E}_e^{(t)}\{\mathbf{J}_e^e, \mathbf{J}_e^m\} + \mathbf{e}_e^{(0,t)} - \mathcal{N}\{\mathbf{J}_e^m\}) + c_i(-\mathcal{E}_i^{(t)}\{\mathbf{J}_e^e, \mathbf{J}_e^m\} + \mathbf{e}_i^{(0,t)} - \mathcal{N}\{\mathbf{J}_e^m\}) = \mathbf{0} \quad (2.78a)$$

$$d_e(\mathcal{H}_e^{(t)}\{\mathbf{J}_e^e, \mathbf{J}_e^m\} + \mathbf{h}_e^{(0,t)} + \mathcal{N}\{\mathbf{J}_e^e\}) + d_i(-\mathcal{H}_i^{(t)}\{\mathbf{J}_e^e, \mathbf{J}_e^m\} + \mathbf{h}_i^{(0,t)} + \mathcal{N}\{\mathbf{J}_e^e\}) = \mathbf{0} \quad (2.78b)$$

where the following operators have been introduced

$$\mathcal{E}_\ell^{(t)}\{\mathbf{J}^e, \mathbf{J}^m\} = -\hat{\mathbf{n}} \times \hat{\mathbf{n}} \times \mathcal{E}_\ell\{\mathbf{J}^e, \mathbf{J}^m\} \quad (2.79a)$$

$$\mathcal{H}_\ell^{(t)}\{\mathbf{J}^e, \mathbf{J}^m\} = -\hat{\mathbf{n}} \times \hat{\mathbf{n}} \times \mathcal{H}_\ell\{\mathbf{J}^e, \mathbf{J}^m\} \quad (2.79b)$$

$$\mathcal{N}\{\cdot\} = \hat{\mathbf{n}} \times \{\cdot\} \quad (2.80)$$

and the incident fields have been rewritten as follows

$$\mathbf{e}_\ell^{(0,t)} = -\hat{\mathbf{n}} \times \hat{\mathbf{n}} \times \mathbf{E}_\ell^{(0)} \quad (2.81)$$

$$\mathbf{h}_\ell^{(0,t)} = -\hat{\mathbf{n}} \times \hat{\mathbf{n}} \times \mathbf{H}_\ell^{(0)} \quad (2.82)$$

Depending on the choice of the coefficient set $\{c_e, c_i, d_e, d_i\}$, several surface integral equations can be derived. The system of equations 2.78 can be recast in the compact form:

$$\mathcal{C}^{(t)}\mathbf{x} = \mathbf{y}^{(t)} \quad (2.83)$$

where we have introduced the operators:

$$\mathcal{C}^{(t)} = \begin{vmatrix} c_e \zeta_e \mathcal{T}_e^{(t)} & -c_e \left(\frac{1}{2}\mathcal{N} - \mathcal{K}_e^{(t)}\right) \\ d_e \left(\frac{1}{2}\mathcal{N} - \mathcal{K}_e^{(t)}\right) & d_e \zeta_e^{-1} \mathcal{T}_e^{(t)} \end{vmatrix} + \begin{vmatrix} -c_i \zeta_i \mathcal{T}_i^{(t)} & -c_i \left(\frac{1}{2}\mathcal{N} + \mathcal{K}_i^{(t)}\right) \\ d_i \left(\frac{1}{2}\mathcal{N} + \mathcal{K}_i^{(t)}\right) & -d_i \zeta_i^{-1} \mathcal{T}_i^{(t)} \end{vmatrix}, \quad (2.84)$$

$$\mathcal{K}_\ell^{(t)}\{\cdot\} = -\mathbf{n} \times \mathbf{n} \times \mathcal{K}_\ell\{\cdot\}|_{S_\ell}, \quad (2.85a)$$

$$\mathcal{T}_\ell^{(t)}\{\cdot\} = -\mathbf{n} \times \mathbf{n} \times \mathcal{T}_\ell\{\cdot\}|_{S_\ell}, \quad (2.85b)$$

Furthermore, we have introduced the excitation vector:

$$\mathbf{y}^{(t)} = - \begin{vmatrix} c_e \mathbf{e}_e^{(0,t)} + c_i \mathbf{e}_i^{(0,t)} \\ d_e \mathbf{h}_e^{(0,t)} + d_i \mathbf{h}_i^{(0,t)} \end{vmatrix}. \quad (2.86)$$

Several surface integral equations can be derived from eq. 2.83 depending on the choice of the coefficients $\{c_e, c_i, d_e, d_i\}$. In particular, if $(c_e/c_i)(d_e/d_i)^* \in \mathbb{R}_+$ the corresponding T-CRIE formulation has a unique solution at any frequency [75]. Some

of the possible T-CRIE formulations are:

$$\begin{aligned}
\text{T-PMCHWT} & \quad (c_e = 1, c_i = -1, d_e = 1, d_i = -1); \\
\text{CTF} & \quad (c_e = \zeta_e^{-1}, c_i = -\zeta_i^{-1}, d_e = \zeta_e, d_i = -\zeta_i); \\
\text{T-Muller} & \quad (c_e = \epsilon_e, c_i = \epsilon_i, d_e = \mu_e, d_i = \mu_i);
\end{aligned} \tag{2.87}$$

The PMCHWT [75] and the CTF are among the most popular formulations and are known to be more accurate in the far field region compared to the N-Muller formulation, especially in presence of object with high permittivity contrast [80]. Nevertheless, they features lower convergence rates with respect to N-formulations when iterative solvers are used [76]. The T-Muller has been proved to be unstable [78].

Combined Field Integral Equations (CFIE)

As an alternative, the CFIE formulations are obtained by a linear combination of the equations T-EFIE, N-EFIE, T-MFIE and N-MFIE equations in each region

$$\alpha_e \zeta_e^{-1} (\text{T-EFIE})_e + \beta_e \zeta_e^{-1} (\text{N-EFIE})_e + \gamma_e (\text{T-MFIE})_e + \delta_e (\text{N-MFIE})_e \tag{2.88a}$$

$$\alpha_i (\text{T-EFIE})_i + \beta_i (\text{N-EFIE})_i + \gamma_i \zeta_i (\text{T-MFIE})_i + \delta_i \zeta_i (\text{N-MFIE})_i \tag{2.88b}$$

Not all CFIE produce an accurate solution. A choice that ensures uniqueness of solution and accuracy is to cut one and only one of the four weighting coefficients.

As a result of this, four classes are determined

NE-THNH ($\alpha_e = \alpha_i = 0$)

$$\beta_e \zeta_e^{-1} (\text{N-EFIE})_e + \gamma_e (\text{T-MFIE})_e + \delta_e (\text{N-MFIE})_e \tag{2.89}$$

$$\beta_i (\text{N-EFIE})_i + \gamma_i \zeta_i (\text{T-MFIE})_i + \delta_i \zeta_i (\text{N-MFIE})_i \tag{2.90}$$

TE-THNH ($\beta_e = \beta_i = 0$)

$$\alpha_e \zeta_e^{-1} (\text{T-EFIE})_e + \gamma_e (\text{T-MFIE})_e + \delta_e (\text{N-MFIE})_e \tag{2.91a}$$

$$\alpha_i (\text{T-EFIE})_i + \gamma_i \zeta_i (\text{T-MFIE})_i + \delta_i \zeta_i (\text{N-MFIE})_i \tag{2.91b}$$

TENE-NH ($\gamma_e = \gamma_i = 0$)

$$\alpha_e \zeta_e^{-1} (\text{T-EFIE})_e + \beta_e \zeta_e^{-1} (\text{N-EFIE})_e + \delta_e (\text{N-MFIE})_e \tag{2.92}$$

$$\alpha_i (\text{T-EFIE})_i + \beta_i (\text{N-EFIE})_i + \delta_i \zeta_i (\text{N-MFIE})_i \tag{2.93}$$

TENE-TM ($\delta_e = \delta_i = 0$)

$$\alpha_e \zeta_e^{-1} (\text{T-EFIE})_e + \beta_e \zeta_e^{-1} (\text{N-EFIE})_e + \gamma_e (\text{T-MFIE})_e \quad (2.94)$$

$$\alpha_i (\text{T-EFIE})_i + \beta_i (\text{N-EFIE})_i + \gamma_i \zeta_i (\text{T-MFIE})_i \quad (2.95)$$

Yla-Oijala and Taskinen have recently presented a novel CFIE formulation, named JMCFIE [81]. The first equation (called JCFIE) is obtained by assuming $\alpha_e = \delta_e = 1$, $\beta_e = \gamma_e = 0$, $\alpha_i = -\zeta_i^{-1}$, $\delta_i = \zeta_i^{-1}$, $\beta_i = \gamma_i = 0$, while the second equation (JMFIE) is obtained by assuming $\alpha_e = \delta_e = 0$, $\beta_e = \gamma_e = \zeta_e$, $\beta_i = \gamma_i = 0$, $\beta_i = \gamma_i = -1$ namely:

$$(\text{N-MFIE})_e + (\text{N-MFIE})_i + \zeta_e^{-1} (\text{T-EFIE})_e - \zeta_i^{-1} (\text{T-EFIE})_i \quad (2.96a)$$

$$(\text{N-EFIE})_e + (\text{N-EFIE})_i + \zeta_e (\text{T-MFIE})_e - \zeta_i (\text{T-MFIE})_i \quad (2.96b)$$

The system of equations 2.96 can be recast in the form:

$$\mathcal{C}_{\text{JMCFIE}} \mathbf{x} = \left(\mathcal{C}_{\text{JMCFIE}}^{(t)} + \mathcal{C}_{\text{JMCFIE}}^{(n)} \right) \mathbf{x} = \left(\mathbf{y}_{\text{JMCFIE}}^{(n)} + \mathbf{y}_{\text{JMCFIE}}^{(t)} \right) = \mathbf{y}_{\text{JMCFIE}} \quad (2.97)$$

where we have introduced the operators $\mathcal{C}_{\text{JMCFIE}}^{(t,n)}$:

$$\begin{aligned} \mathcal{C}_{\text{JMCFIE}}^{(t)} &= \mathcal{C}^{(n)} \left\{ c_e = \zeta_e^{-1}, c_i = -\zeta_i^{-1}, d_e = \zeta_e, d_i = -\zeta_i \right\}, \\ \mathcal{C}_{\text{JMCFIE}}^{(n)} &= \mathcal{C}^{(t)} \left\{ a_e = a_i = b_e = 1 = b_i = 1 \right\}, \end{aligned} \quad (2.98)$$

and the quantities $\mathbf{y}_{\text{JMCFIE}}^{(t,n)}$ on the RHS:

$$\begin{aligned} \mathbf{y}_{\text{JMCFIE}}^{(t)} &= \mathbf{y}^{(t)} \left\{ c_e = \zeta_e^{-1}, c_i = -\zeta_i^{-1}, d_e = \zeta_e, d_i = -\zeta_i \right\}, \\ \mathbf{y}_{\text{JMCFIE}}^{(n)} &= \mathbf{y}^{(n)} \left\{ a_e = a_i = b_e = 1 = b_i = 1 \right\}. \end{aligned} \quad (2.99)$$

The JMCFIE has been proven to be a very robust formulation, featuring a good far-field accuracy and fast iterative convergence for a wide range of test cases [78]. In particular, it is very effective to tackle the problems of composite objects with junctions [81].

Chapter 3

Discretization

Numerical Formulations of the Integral Equations are necessary to find solutions for non-canonical scattering problems. The metric spaces necessary for numerical handling and the main results are briefly introduced in Appendix A. The basic functions used in this work are presented below.

3.1 RWG Basis Function

Accurate and efficient solutions of integral formulations heavily depends on the choice of basis functions. Two broad categories of basis functions may be identified:

- sub-domain functions, which are non-zero only over a portion of the object
- entire-domain functions, which extend over the entire domain of one or few individual objects

First, we introduce probably the best known local basis function, namely the Rao-Wilton-Glisson functions, or rooftop functions [6]. We consider a triangular mesh \mathcal{M} of the domain V_i having N_e edges. The length of the p^{th} edge is denoted with ℓ_p and the two triangles sharing the edge as T_p^+ and T_p^- . They have an area of A_p^+ and A_p^- . In addition, the vertices of T_p^+ and T_p^- which are opposite to the p^{th} edge are indicated by v_p^+ and v_p^- respectively.

The unknown electric \mathbf{J}_e^e and magnetic currents \mathbf{J}_e^m are expanded in terms of the Rao-Wilton-Glisson (RWG) function set $\{\mathbf{W}_1, \mathbf{W}_2, \dots, \mathbf{W}_{N_e}\}$ as

$$\mathbf{J}_e^e \simeq \sum_{p=1}^{N_e} \alpha_p \mathbf{W}_p(\mathbf{r}) \quad (3.1)$$

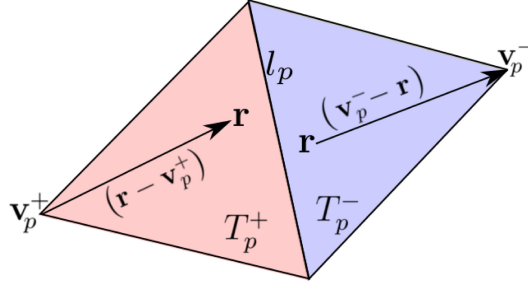


Figure 3.1 – Illustration of the RWG basis function associated to the p^{th} edge and defined on the triangle pair T_p^+, T_p^- . In T_p^+ and T_p^- \mathbf{f}_p is proportional to the vector $(\mathbf{r} - \mathbf{v}_p^+)$ and $(\mathbf{v}_p^- - \mathbf{r})$, respectively.

$$\mathbf{J}_e^m \simeq \sum_{p=1}^{N_e} \beta_p \mathbf{W}_p(\mathbf{r}) \quad (3.2)$$

where the RWG relative to the p^{th} edge is given by

$$\mathbf{W}_p(\mathbf{r}) = \begin{cases} +\frac{\ell_p}{2A_p^+}(\mathbf{r} - \mathbf{v}_p^+) & \mathbf{r} \in T_p^+ \\ -\frac{\ell_p}{2A_p^-}(\mathbf{r} - \mathbf{v}_p^-) & \mathbf{r} \in T_p^- \\ \mathbf{0} & \text{otherwise} \end{cases} \quad (3.3)$$

and the corresponding divergence is

$$\nabla \cdot \mathbf{W}_p(\mathbf{r}) = \begin{cases} +\frac{\ell_p}{A_p^+} & \mathbf{r} \in T_p^+ \\ -\frac{\ell_p}{A_p^-} & \mathbf{r} \in T_p^- \\ \mathbf{0} & \text{otherwise} \end{cases} \quad (3.4)$$

where the support of \mathbf{W}_p is $S_p = T_p^+ \cup T_p^-$

3.1.1 Finite-dimensional operators

Once introduced the symmetric product for the space of square integrable vector functions defined on S

$$\langle \mathbf{f}, \mathbf{g} \rangle = \int_S \mathbf{f} \cdot \mathbf{g} dS \quad (3.5)$$

we assembly the finite-dimensional operators recurring in SIE formulations by using the Galerkin method.

$$K_{l,pq}^{(n)} = \langle \mathbf{W}_p, K_l^{(n)}\{\mathbf{W}_q\} \rangle = \langle \mathbf{W}_q, \mathbf{n} \times K_l\{\mathbf{W}_q\} \rangle \quad (3.6)$$

$$T_{l,pq}^{(n)} = \langle \mathbf{W}_p, T_l^{(n)}\{\mathbf{W}_q\} \rangle = \langle \mathbf{W}_q, \mathbf{n} \times T_l\{\mathbf{W}_q\} \rangle \quad (3.7)$$

$$\mathbf{K}_{l,pq}^{(t)} = \langle \mathbf{W}_p, K_l^{(t)}\{\mathbf{W}_q\} \rangle = \langle \mathbf{W}_q, \mathbf{n} \times \mathbf{n} \times K_l\{\mathbf{W}_q\} \rangle \quad (3.8)$$

$$\mathbf{T}_{l,pq}^{(t)} = \langle \mathbf{W}_p, T_l^{(t)}\{\mathbf{W}_q\} \rangle = \langle \mathbf{W}_p, \mathbf{n} \times \mathbf{n} \times T_l\{\mathbf{W}_q\} \rangle \quad (3.9)$$

$$\mathbf{I}_{l,pq} = \langle \mathbf{W}_p, I_l\{\mathbf{W}_q\} \rangle = \langle \mathbf{W}_p, \mathbf{W}_q \rangle \quad (3.10)$$

$$\mathbf{N}_{l,pq} = \langle \mathbf{W}_p, N_l\{\mathbf{W}_q\} \rangle = \langle \mathbf{W}_p, \mathbf{n} \times \mathbf{W}_q \rangle \quad (3.11)$$

Similarly, we assemble the discrete excitation vectors

$$h_{l,p}^{(0,n)} = \langle \mathbf{W}_p, \mathbf{h}_l^{(0,n)} \rangle = \langle \mathbf{W}_p, \mathbf{n} \times \mathbf{h}_l^{(0)} \rangle \quad (3.12)$$

$$e_{l,p}^{(0,n)} = \langle \mathbf{W}_p, \mathbf{e}_l^{(0,n)} \rangle = \langle \mathbf{W}_p, \mathbf{n} \times \mathbf{e}_l^{(0)} \rangle \quad (3.13)$$

$$h_{l,p}^{(0,t)} = \langle \mathbf{W}_p, \mathbf{h}_l^{(0,t)} \rangle = \langle \mathbf{W}_p, \mathbf{n} \times \mathbf{n} \times \mathbf{h}_l^{(0)} \rangle \quad (3.14)$$

$$e_{l,p}^{(0,t)} = \langle \mathbf{W}_p, \mathbf{e}_l^{(0,t)} \rangle = \langle \mathbf{W}_p, \mathbf{n} \times \mathbf{n} \times \mathbf{e}_l^{(0)} \rangle \quad (3.15)$$

In the below, we will explicitly look at the form of the assembled operators κ and τ as in [82].

$\mathbf{K}_{\ell,pq}^{(n)}$ discrete operator

Starting from the definition of $\mathbf{K}_{\ell,pq}^{(n)}$, by using 2.52, we have

$$\mathbf{K}_{\ell,pq}^{(n)} = - \int_{S_p} \mathbf{W}_p(\mathbf{r}) \cdot \mathbf{n} \times \left[\int_{S_q} \mathbf{W}_q(\mathbf{r}') \times \nabla' g_\ell(\mathbf{r} - \mathbf{r}') dS' \right] dS \quad (3.16)$$

$S_p = T_p^- \cup T_p^+$ and $S_q = T_q^- \cup T_q^+$ are the support of the RWG functions \mathbf{W}_p and \mathbf{W}_q , respectively. This expression can be further elaborated by splitting the integral domains S_p and S_q into the two constitutive triangular facets and by substituting the expressions of the RWGs given in 3.3.

$$\mathbf{K}_{\ell,pq}^{(n)} = \frac{\ell_p \ell_q}{4} \sum_{r=\pm} \sum_{s=\pm} \frac{rs}{A_p^r A_q^s} \int_{T_p^r} (\mathbf{r} - \mathbf{v}_p^r) \times \mathbf{n} \cdot \left[\int_{T_q^s} (\mathbf{r}' - \mathbf{v}_q^s) \times \nabla g_\ell(\mathbf{r} - \mathbf{r}') dS' \right] dS \quad (3.17)$$

Two different problems concern this discrete formulation: firstly, the operator is nonsingular when $p = q$. In addition, when the observation point $\mathbf{r}_p \notin T_q$ is within a certain critical distance from the source triangular element (T_q) the Gauss integration method can fail to evaluate the term. As a consequence of this, singularity extraction techniques and closed form expressions for the singular terms are needed.

$\mathbb{T}_{\ell,pq}^{(n)}$ **discrete operator**

Starting from the definition of $\mathbb{T}_{\ell,pq}^{(n)}$, by using 2.53, we have

$$\begin{aligned} \mathbb{T}_{\ell,pq}^{(n)} = & -ik_\ell \int_{S_p} \mathbf{W}_p(\mathbf{r}) \cdot \mathbf{n} \times \left[\int_{S_q} g_\ell(\mathbf{r} - \mathbf{r}') \mathbf{W}_q(\mathbf{r}') dS' \right] dS \\ & - \frac{1}{ik_\ell} \int_{S_p} \mathbf{W}_p(\mathbf{r}) \cdot \mathbf{n} \times \left[\int_{S_q} \nabla' g_\ell(\mathbf{r} - \mathbf{r}') \nabla'_S \cdot \mathbf{W}_q(\mathbf{r}') dS' \right] dS \end{aligned} \quad (3.18)$$

This expression can be further elaborated by splitting the integral domains S_p and S_q into the two constitutive triangular facets and by substituting the expressions of the RWGs given in 3.3 and their divergence.

$$\begin{aligned} \mathbb{T}_{\ell,pq}^{(n)} = & i \frac{\ell_p \ell_q}{4} \sum_{r=\pm} \sum_{s=\pm} \frac{rs}{A_p^r A_q^s} \left\{ -k_\ell \int_{T_p^r} (\mathbf{r} - \mathbf{v}_p^r) \times \mathbf{n} \cdot \left[\int_{T_q^s} g_\ell(\mathbf{r} - \mathbf{r}') (\mathbf{r} - \mathbf{v}_q^s) dS' \right] dS + \right. \\ & \left. - \frac{2}{k_\ell} \int_{T_p^r} (\mathbf{r} - \mathbf{v}_p^r) \times \mathbf{n} \cdot \nabla_S \left[\int_{T_q^s} g_\ell(\mathbf{r} - \mathbf{r}') dS' \right] dS \right\} \end{aligned} \quad (3.19)$$

By exploiting the identity $\nabla_S \cdot (\alpha \mathbf{v}) = \mathbf{v} \cdot \nabla_S \alpha + \alpha \nabla_S \cdot \mathbf{v}$ and the RWG property $\nabla_S \cdot [\mathbf{W}_p(\mathbf{r}) \times \mathbf{n}] = \mathbf{0}$, we arrive at the following expression

$$\begin{aligned} \mathbb{T}_{\ell,pq}^{(n)} = & i \frac{\ell_p \ell_q}{4} \sum_{r=\pm} \sum_{s=\pm} \frac{rs}{A_p^r A_q^s} \left\{ -k_\ell \int_{T_p^r} (\mathbf{r} - \mathbf{v}_p^r) \times \mathbf{n} \cdot \left[\int_{T_q^s} g_\ell(\mathbf{r} - \mathbf{r}') (\mathbf{r}' - \mathbf{v}_q^s) dS' \right] dS + \right. \\ & \left. - \frac{2}{k_\ell} \oint_{\partial T_p^r} \left[\int_{T_q^s} g_\ell(\mathbf{r} - \mathbf{r}') dS' \right] (\mathbf{r} - \mathbf{v}_p^r) \cdot d\mathbf{l} \right\} \end{aligned} \quad (3.20)$$

Again, when the observation point $\mathbf{r}_p \notin T_q$ is within a certain critical distance from the source triangular element (T_q) the Gauss integration method can fail to evaluate the term. In order to manage singularities of both integrals, the techniques introduced by Graglia have been used.

 $\mathbb{K}_{\ell,pq}^{(t)}$ **discrete operator**

Starting from the definition of $\mathbb{K}_{\ell,pq}^{(t)}$, by using 2.52, we have

$$\mathbb{K}_{\ell,pq}^{(t)} = \int_{S_p} \mathbf{W}_p(\mathbf{r}) \cdot \mathbf{n} \times \mathbf{n} \times \left[\int_{S_q} \mathbf{W}_q(\mathbf{r}') \times \nabla' g_\ell(\mathbf{r} - \mathbf{r}') dS' \right] dS \quad (3.21)$$

By splitting the integral domains S_p and S_q into the two constitutive triangular facets and by exploiting the fact that $\mathbf{W}_p(\mathbf{r}) \cdot \mathbf{n} = 0$ in T_p^\pm we obtain

$$\mathbf{K}_{\ell,pq}^{(t)} = \frac{\ell_p \ell_q}{4} \sum_{r=\pm} \sum_{s=\pm} \frac{rs}{A_p^r A_q^s} \int_{T_p^r} (\mathbf{r} - \mathbf{v}_p^r) \cdot \left[\int_{T_q^s} (\mathbf{r}' - \mathbf{v}_q^s) \times \nabla g_\ell(\mathbf{r} - \mathbf{r}') dS' \right] dS \quad (3.22)$$

As before, the integral needs to be numerically evaluated using the techniques presented in...

$\mathbf{T}_{\ell,pq}^{(t)}$ **discrete operator**

$$\begin{aligned} \mathbf{T}_{\ell,pq}^{(t)} &= ik_\ell \int_{S_p} \mathbf{f}_p(\mathbf{r}) \cdot \mathbf{n} \times \mathbf{n} \times \left[\int_{S_q} g_\ell(\mathbf{r} - \mathbf{r}') \mathbf{f}_q(\mathbf{r}') dS' \right] dS \\ &\quad + \frac{1}{ik_\ell} \int_{S_p} \mathbf{f}_p(\mathbf{r}) \cdot \mathbf{n} \times \mathbf{n} \times \left[\int_{S_q} \nabla'_S g_\ell(\mathbf{r} - \mathbf{r}') \nabla'_S \cdot \mathbf{f}_q(\mathbf{r}') dS' \right] dS \end{aligned} \quad (3.23)$$

$$\begin{aligned} \mathbf{T}_{\ell,pq}^{(t)} &= -ik_\ell \int_{S_p} \mathbf{W}_p(\mathbf{r}) \cdot \left[\int_{S_q} g_\ell(\mathbf{r} - \mathbf{r}') \mathbf{W}_q(\mathbf{r}') dS' \right] dS \\ &\quad + \frac{1}{ik_\ell} \int_{S_p} \int_{S_q} [\mathbf{W}_p(\mathbf{r}) \cdot \nabla_S g_\ell(\mathbf{r} - \mathbf{r}')] \nabla'_S \cdot \mathbf{W}_q(\mathbf{r}') dS' dS \end{aligned} \quad (3.24)$$

$$\begin{aligned} \mathbf{T}_{\ell,pq}^{(t)} &= -ik_\ell \int_{S_p} \mathbf{W}_p(\mathbf{r}) \cdot \left[\int_{S_q} g_\ell(\mathbf{r} - \mathbf{r}') \mathbf{W}_q(\mathbf{r}') dS' \right] dS \\ &\quad - \frac{1}{ik_\ell} \int_{S_p} \int_{S_q} g_\ell(\mathbf{r} - \mathbf{r}') [\nabla_S \cdot \mathbf{W}_p(\mathbf{r})] [\nabla'_S \cdot \mathbf{W}_q(\mathbf{r}')] dS dS' \end{aligned} \quad (3.25)$$

$$\begin{aligned} \mathbf{T}_{\ell,pq}^{(t)} &= i \frac{\ell_p \ell_q}{4} \sum_{r=\pm} \sum_{s=\pm} \frac{rs}{A_p^r A_q^s} \left[-k_\ell \int_{T_p^r} (\mathbf{r} - \mathbf{v}_p^r) \cdot \int_{T_q^s} g_\ell(\mathbf{r} - \mathbf{r}') (\mathbf{r} - \mathbf{v}_q^s) dS' dS \right. \\ &\quad \left. + \frac{4}{k_\ell} \int_{T_p^r} \int_{T_q^s} g_\ell(\mathbf{r} - \mathbf{r}') dS' dS \right] \end{aligned} \quad (3.26)$$

3.2 Loop-Star Basis Function

Surface integral formulations may suffer from ill-conditioning due to low frequency breakdown. The low frequency breakdown phenomenon manifests when the operating wavelength is much larger than the dimension of the object [83], and originates from the different frequency-scaling of the terms associated with the vector and the scalar potentials. This is a common scenario which may be encountered in several applications, including metamaterials and electromagnetic bandgap (EBG) structures, or in the analysis of interconnects and packaging. This problem has been addressed by using quasi-Helmholtz decompositions, such as loop-star [83, 84, 85], loop-tree [11, 86], or null-pinv [87] decomposition, followed by a basis rearrangement [88, 89].

It is also worth to point out that some formulations are immune from this problem, such as the N-Müller formulation [90], or the formulation obtained by augmenting [91, 92] the traditional EFIE by including charge as extra unknown.

Another very important sub-domain basis function is represented by the loop and star basis functions introduced by Wilton, Lim, and Rao [10, 84]. Again, let us consider a surface triangulation of S , with N_n vertices (nodes), N_t elements and N_e edges.

3.2.1 Loop basis functions

First, we introduce a set of solenoidal basis functions, the *loop* basis functions, denoted as $\{\mathbf{j}_q^\circ, q = 1, 2, \dots, N_n\}$, which are associated with the inner nodes of the mesh. Each function represents the current that flows around a certain node of the surface triangular mesh. The loop function \mathbf{j}_q° associated to the q -th node of the mesh, has the following representation in terms of a linear combination of RWG basis functions $\{\mathbf{W}_r\}$ associated to the edges attached to the anchor node q :

$$\mathbf{j}_q^\circ = \sum_{r \in \text{loop}_q} \beta_{q,r}^{\circ\text{RWG}} \mathbf{W}_r, \quad (3.27)$$

where

$$\beta_{q,r}^{\circ\text{RWG}} = \begin{cases} +1/\ell_r & \text{the direction of } \mathbf{W}_r \text{ is coherent with the orientation of the loop} \\ -1/\ell_r & \text{the direction of } \mathbf{W}_r \text{ is opposite to the orientation of the loop} \end{cases} \quad (3.28)$$

where ℓ_r is the length of the r -th edge attached to the node q . From the coefficients $\beta_{i,j}^{\circ\text{RWG}}$ it is possible to construct a transformation matrix that connects a representation in terms of RWG to a representation in terms of Loop basis functions. Given the fact that the divergence of the adjacent RWG basis on the same patch cancels each other (3.4), it is easy to point out that

$$\nabla \cdot \mathbf{j}_q^\circ = 0 \quad (3.29)$$

3.2.2 Star basis functions

The identification of the solenoidal part brings to the attention the dual, equally important issue of finding a basis that spans the remaining non-solenoidal part of the solution. The *star* functions, denoted as $\{\mathbf{j}_i^*, i = 1, 2, \dots, N_t\}$ instead, are associated with the triangular elements of the mesh. Each function represents the current

that flows out from the triangle T_q . The star function \mathbf{J}_q can be expressed as a superposition of RWG basis functions supported by the common triangle T_q

$$\mathbf{j}_q^* = \sum_r \beta_{q,r}^{\text{RWG}} \mathbf{W}_r, \quad (3.30)$$

where

$$\beta_{q,r}^{\text{RWG}} = \begin{cases} +1/\ell_r & \text{the triangle } r \text{ is the } T_r^+ \text{ for the } r\text{-th RWG} \\ -1/\ell_r & \text{the triangle } r \text{ is the } T_r^- \text{ for the } r\text{-th RWG} \end{cases} \quad (3.31)$$

where the summation runs only on the RWG having as common face the triangle T_q .

From the coefficients $\beta_{q,r}^{\text{RWG}}$, it is possible to construct the RWG to Star transformation matrix, denoted by $\underline{\underline{B}}^{\text{RWG}}$. The star basis functions are not curl free

$$\nabla \times \mathbf{j}_q^* \neq 0 \quad (3.32)$$

but contain a subspace of the irrotational component of the surface current. For this reason the loop-star decomposition is also called "incomplete Helmholtz decomposition".

Both loop and star basis functions can be written as a linear combination of RWG basis functions [6] so they span the same space. Therefore, it is necessary that the total degree of freedom in the loop-star formulation is the same as that of the usual RWG approach. Consequently, for closed surface with no handles, the Loop-Star set is not a linearly independent set: a Loop function corresponding to an arbitrary inner node and a Star function corresponding to an arbitrary cell should be eliminated to obtain a linearly independent set with, respectively, $(N_n - 1)$ and $(N_t - 1)$ elements.

Chapter 4

Static surface mode expansion for the full-wave scattering from penetrable objects

In this chapter, we investigate the use of a very peculiar set of entire domain basis functions that can simplify the numerical solution of electromagnetic scattering problems from a given object at multiple frequencies. We investigate the use of static surface current modes as an entire-domain basis set to represent the unknown current densities in surface integral equation formulations. These modes are the union of two sets: longitudinal and transverse modes, exhibiting vanishing surface curl and surface divergence, respectively. We assemble these two sets by solving two auxiliary frequency-independent eigenvalue problems, involving Hermitian and positive-definite surface-integral operators, having the *static* Green function as kernel. We demonstrate that the use of these modes in the Galerkin projection of the Poggio-Miller-Chang-Harrington-Wu-Tsai surface integral formulation [93] leads to a drastic reduction of the number of unknowns with respect to sub-domain basis functions without deteriorating the accuracy of the solution. The static modes are the low-frequency limit of resonance modes of surfaces of finite conductivity [23]. Their volume counterparts have been presented in Ref. [94, 95] (longitudinal) and in Ref. [96] (transverse) where they have been already used to expand the electromagnetic field [97, 98, 99]. The proposed approach shares similarities with the one introduced by Vecchi et al. and used in a hybrid spectral-spatial method for the analysis of printed antennas [100, 101]. There are several attributes that make the static surface modes particularly interesting

- For objects of size comparable to the wavelength of operation, only few modes

are sufficient to describe the emergent scattering response. This property also holds true when multiple scattering problems are considered, namely when the electromagnetic system is a collection of mutually-coupled objects as long as the objects are not too close to each other. These characteristics are particularly appealing for the numerical modeling of metasurfaces and metalens.

- The retarded Green function, constituting the kernel of integral operators recurring in surface integral formulations such as the PMCHWT, may be decomposed as the sum of the static Green function (with integrable singularity) and a proper difference (which is a regular function); the resulting integral operators containing the static Green function are diagonalized by the static modes, thus the overall problem is regularized [102].
- The use of the static modes expansion combined with an appropriate rescaling and rearranging of the unknowns makes the PMCHWT formulation immune from the low-frequency breakdown problem, which otherwise plagues it due to the different frequency scaling of the involved operators.
- The static modes only depend on the shape of the object, thus, the same static basis can be used (and has the same advantages) regardless of the operating frequency and material of object. This fact enables the description of any scattering scenario involving one or more objects of a given shape, in terms of the same “alphabet” of basis function, regardless of the frequency of operation. This fact constitutes a great advantage compared to other basis sets (e.g., characteristic modes), where the modes depend on frequency and materials, thus the alphabet of basis functions, in which the scattering process is described, changes every time one of these parameters is varied, thus preventing a unified description.

4.1 Static current modes

We denote with V the region occupied by the particle, with S the boundary of V , with $\hat{\mathbf{n}}$ the normal to the surface S pointing outward. Hereafter, in order to define the metric spaces necessary for the numerical resolution of the problem, we define the scalar product as

$$\langle \mathbf{C}, \mathbf{D} \rangle = \int \mathbf{C}^*(\mathbf{r}) \cdot \mathbf{D}(\mathbf{r}) dS \quad (4.1)$$

and the norm induced

$$\|\mathbf{C}\| = \sqrt{\langle \mathbf{C}, \mathbf{C} \rangle} \quad (4.2)$$

If the integration domain is not explicitly indicated, the scalar product is defined over S .

4.1.1 Helmholtz decomposition

Any sufficiently smooth vector field \mathbf{C} defined on the surface S can be resolved into the sum of two terms:

- an irrotational and non-solenoidal vector field \mathbf{C}^{\parallel}
- a solenoidal and rotational (non zero curl) vector field \mathbf{C}^{\perp}

This is a particular case of the Helmholtz decomposition for vector fields defined on a closed surface. The vector fields \mathbf{C}^{\parallel} and \mathbf{C}^{\perp} are orthogonal according to the scalar product $\langle \cdot, \cdot \rangle$. The components \mathbf{C}^{\parallel} and \mathbf{C}^{\perp} belong to the functional spaces

$$\mathcal{L}^{\perp} = \{ \nabla_S \cdot \mathbf{w} = 0 | \forall \mathbf{r} \in S \} \quad (4.3)$$

$$\mathcal{L}^{\parallel} = \{ \nabla_S \times \mathbf{w} = \mathbf{0} | \forall \mathbf{r} \in S \} \quad (4.4)$$

We may build a basis for the functional spaces \mathcal{L}^{\perp} and \mathcal{L}^{\parallel} by considering the following problems.

4.1.2 Static longitudinal current modes

The static longitudinal surface current modes (called in the following *longitudinal modes* for brevity) are the solution of the auxiliary eigenvalue problem:

$$\mathcal{T}_0^{\parallel} \{ \mathbf{j}_k^{\parallel} \} (\mathbf{r}) = \gamma_k^{\parallel} \mathbf{j}_k^{\parallel} \quad \text{on } S, \quad (4.5)$$

with

$$\mathcal{T}_0^{\parallel} \{ \mathbf{w} \} (\mathbf{r}) = \hat{\mathbf{n}} \times \hat{\mathbf{n}} \times \nabla \int_S g_0(\mathbf{r} - \mathbf{r}') \nabla'_S \cdot \mathbf{w}(\mathbf{r}') dS', \quad (4.6)$$

being g_0 the homogeneous space static Green's function

$$g_0(\mathbf{r} - \mathbf{r}') = \frac{1}{4\pi} \frac{1}{|\mathbf{r} - \mathbf{r}'|}. \quad (4.7)$$

Apart from the factor $1/\varepsilon_0$, the integral operator 4.6 gives the tangential component of the static electric field generated by a surface charge density distribution $(\nabla'_S \cdot \mathbf{w})$. Its spectrum has the following properties:

- the set of eigenvalues $\{\gamma_k^{\parallel}\}$ and the set of eigenfunctions $\{\mathbf{j}_k^{\parallel}\}$ are infinite countable
- the eigenvalues are real and positive;
- the eigenfunctions associated to non-degenerate eigenvalues are orthogonal according to the scalar product $\langle \cdot, \cdot \rangle$;
- the eigenvalues $\{\gamma_k^{\parallel}\}$ and the modes $\{\mathbf{j}_k^{\parallel}\}$ depend on the shape of the particle, but are independent of both particle material (assumed to be homogeneous) and frequency of operation;
- for a spherical surface of unit radius the eigenvalues have the following analytical expression

$$\frac{1}{\gamma_k^{\parallel}} = \frac{(2n+1)}{n(n+1)}. \quad (4.8)$$

The comparison between the analytical eigenvalues and those obtained numerically allows to verify the correctness of the eigenvalues (4.1)

In the following we employ the set $\{\mathbf{j}_k^{\parallel}\}$ for the representation of square integrable irrotational vector fields defined on S.

4.1.3 Static transverse current modes

The static transverse surface current modes (called *transverse modes* in the following for brevity) are solution of the auxiliary eigenvalue problem:

$$\mathcal{T}_0^{\perp} \{\mathbf{j}_k^{\perp}\}(\mathbf{r}) = \gamma_k^{\perp} \mathbf{j}_k^{\perp} \quad \text{on } S, \quad (4.9)$$

with

$$\mathcal{T}_0^{\perp} \{\mathbf{w}\}(\mathbf{r}) = -\hat{\mathbf{n}} \times \hat{\mathbf{n}} \times \int_S g_0(\mathbf{r} - \mathbf{r}') \mathbf{w}(\mathbf{r}') dS'. \quad (4.10)$$

Apart from the factor μ_0 the above integral operator gives the vector potential generated by a surface current distribution. Its spectrum has among others the following properties:

- the set of eigenvalues $\{\gamma_k^{\perp}\}$ and the set of eigenfunctions $\{\mathbf{j}_k^{\perp}\}$ are infinite countable
- the eigenvalues are real and positive;
- the eigenfunctions associated to non-degenerate eigenvalues are orthogonal according to the scalar product $\langle \cdot, \cdot \rangle$;

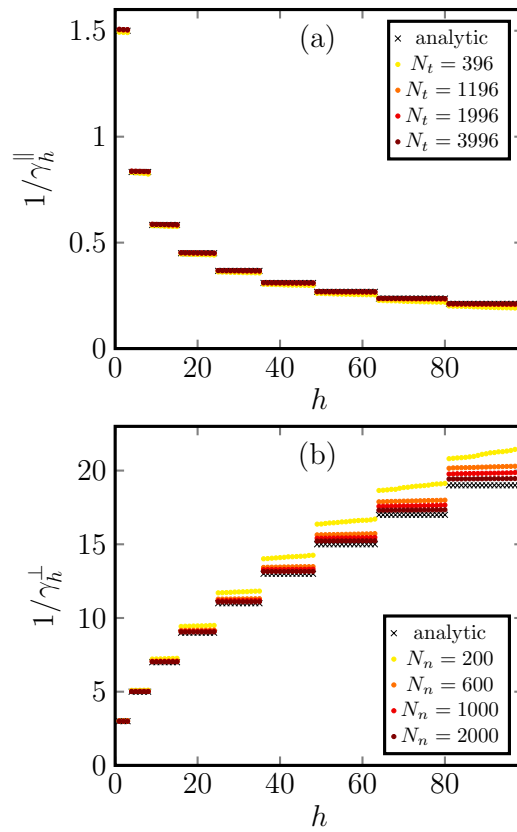


Figure 4.1 – Reciprocal of the first 100 eigenvalues γ_k^{\parallel} (a) and γ_k^{\perp} (b) associated with the longitudinal and transverse static modes of a sphere, respectively, and evaluated for several densities of the triangular surface mesh (filled circles of different colors) having N_t elements and N_n nodes. The eigenvalues are compared with their analytical counterpart.

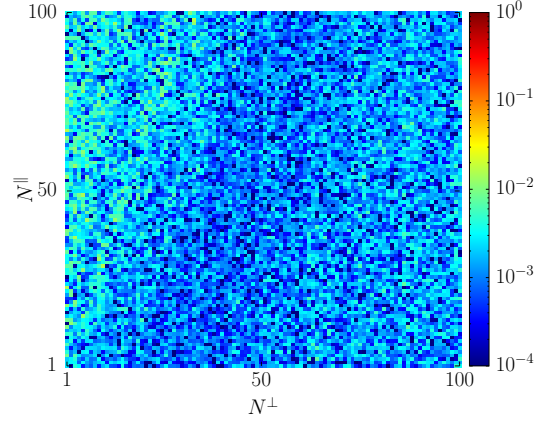


Figure 4.2 – "Mutual" Gram matrix $g_{hk} = \langle \mathbf{j}_h^\parallel, \mathbf{j}_k^\perp \rangle$, which tests the orthogonality among the discrete longitudinal and transverse static modes. The maximum occurrence of the computed Gram matrix is (in absolute value) is 0.024. Only the first 100×100 occurrences of the Gram Matrix are shown.

- the eigenvalues $\{\gamma_k^\perp\}$ and the modes $\{\mathbf{j}_k^\perp\}$ depend on the shape of the particle, but are independent of both particle material (assumed to be homogeneous) and frequency of operation;
- for a spherical surface of unit radius the eigenvalues have the following analytical expression

$$\frac{1}{\gamma_k^\perp} = 2n + 1. \quad (4.11)$$

The comparison between the analytical eigenvalues and those obtained numerically allows to verify the correctness of the eigenvalues (4.1)

In the following we employ the set $\{\mathbf{j}_k^\perp\}$ for the representation of square integrable solenoidal vector fields defined on S with zero surface divergence.

4.2 Poggio-Miller-Chang-Harrington-Wu-Tsai (PMCHWT) surface integral equation

Let us consider the scattering problem presented in Sec. 2.3.2: an object is illuminated by a time harmonic electromagnetic field $\text{Re}\{\mathbf{E}^{(0)} e^{i\omega t}\}$. The material has permittivity $\varepsilon^+(\omega)$, permeability $\mu^+(\omega)$ and it is surrounded by a background medium with permittivity $\varepsilon^-(\omega)$ and permeability $\mu^-(\omega)$. As mentioned above, in order to

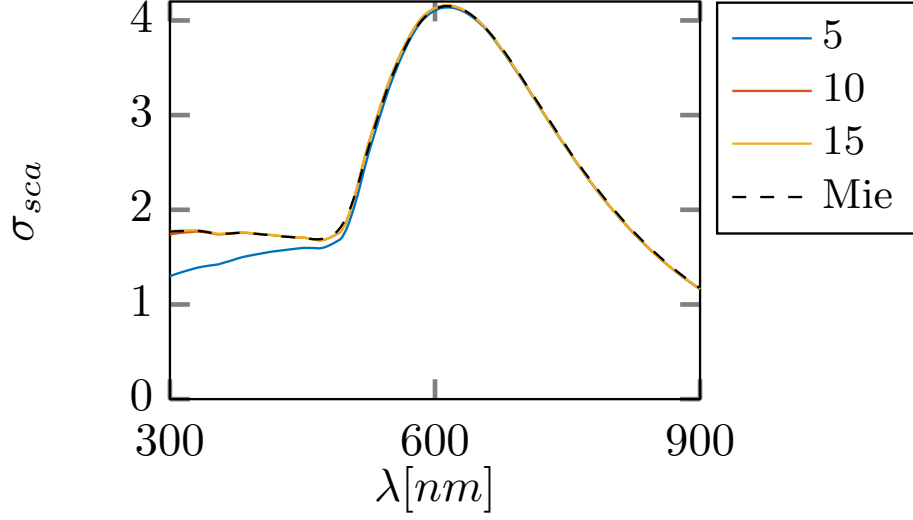


Figure 4.3 – Scattering efficiency σ_{sca} of a gold particle $R = 100\text{nm}$ excited by a linearly polarized plane wave in the visible and near infrared spectral range. σ_{sca} is evaluated using the PMCHWT employing an increasing number of longitudinal and transverse static modes ($N^{\parallel} = N^{\perp} = 5, 10, 15$). The reference Mie solution (black dashed line) is also shown for comparison.

avoid the non-uniqueness of the solution, a linear combination of EFIE and MFIE is used. From T-Combined Region Integral Equations (see Sec. 2.3.5)

$$\begin{cases} c_e(\text{T-EFIE})_e + c_i(\text{T-EFIE})_i \\ d_e(\text{T-MFIE})_e + d_i(\text{T-MFIE})_i \end{cases} \quad (4.12)$$

it is placed $(c_e, c_i, d_e, d_i) = (1, -1, 1, -1)$. The equivalent electric \mathbf{j}^e and magnetic \mathbf{j}^m surface current densities, defined on S , are solution of the following surface integral problem formulated by Poggio-Miller-Chang-Harrington-Wu-Tsai [19]:

$$\mathcal{Z} \mathbf{X} = \mathbf{Y}, \quad (4.13)$$

where

$$\mathcal{Z} = \begin{pmatrix} \zeta^- \mathcal{T}_- + \zeta^+ \mathcal{T}_+ & \boldsymbol{\kappa}_- + \boldsymbol{\kappa}_+ \\ -(\boldsymbol{\kappa}_- + \boldsymbol{\kappa}_+) & \mathcal{T}_- / \zeta^- + \mathcal{T}_+ / \zeta^+ \end{pmatrix}, \quad (4.14)$$

$$\mathbf{X} = [\mathbf{J}^e, \mathbf{J}^m]^\top, \quad \mathbf{Y} = [\mathbf{e}^{(0,t)}, \mathbf{h}^{(0,t)}]^\top, \quad (4.15)$$

$$\mathbf{e}^{(0,t)} = -\hat{\mathbf{n}} \times \hat{\mathbf{n}} \times \mathbf{E}^{(0)}|_S, \quad \mathbf{h}^{(0,t)} = -\hat{\mathbf{n}} \times \hat{\mathbf{n}} \times \mathbf{H}^{(0)}|_S, \quad (4.16)$$

Again, the operators \mathcal{K}_\pm and \mathcal{T}_\pm are the MFIE and EFIE integral operators:

$$\mathcal{K}_\pm \{\mathbf{w}\}(\mathbf{r}) = \hat{\mathbf{n}} \times \hat{\mathbf{n}} \times \int_S \mathbf{w}(\mathbf{r}') \times \nabla' g^\pm(\mathbf{r} - \mathbf{r}') dS', \quad (4.17a)$$

$$\begin{aligned} \mathcal{T}_\pm \{\mathbf{w}\}(\mathbf{r}) &= ik^\pm \hat{\mathbf{n}} \times \hat{\mathbf{n}} \times \int_S g^\pm(\mathbf{r} - \mathbf{r}') \mathbf{w}(\mathbf{r}') dS' \\ &+ \frac{1}{ik^\pm} \hat{\mathbf{n}} \times \hat{\mathbf{n}} \times \int_S \nabla' g^\pm(\mathbf{r} - \mathbf{r}') \nabla'_S \cdot \mathbf{w}(\mathbf{r}') dS' \end{aligned} \quad (4.17b)$$

$\nabla_S \cdot$ denotes the surface divergence, g^\pm is the homogeneous space Green's function of the region V_l , i.e.

$$g^\pm(\mathbf{r} - \mathbf{r}') = \frac{e^{-ix^\pm |\mathbf{r} - \mathbf{r}'|}}{4\pi |\mathbf{r} - \mathbf{r}'|}, \quad (4.18)$$

$x^\pm = k^\pm \ell_c$, $k^\pm = \omega \sqrt{\mu^\pm \varepsilon^\pm}$, and $\zeta^\pm = \sqrt{\mu^\pm / \varepsilon^\pm}$. We anticipate that, by decomposing the Green function 4.18 as the sum of the static Green function and a regular difference term, the choice of static basis expansion regularizes the scattering operators, leading to an effective way to diagonalize the block-diagonal operators of the impedance matrix which are associated with the static Green function.

4.3 Finite Element Method

Let us introduce a surface triangulation of S with N_n vertices (nodes), N_t elements and N_e edges.

4.3.1 Numerical generation of the static basis

Specifically, the generic transverse mode \mathbf{j}_h^\perp is expanded in terms of (solenoidal) loop basis functions $\{\mathbf{j}_q^\circ\}$, introduced in Sec. 3.2.1 with coefficients $\alpha_{h,q}^{\perp,\circ}$. Dually, the generic longitudinal mode \mathbf{j}_h^\parallel is expanded in terms of Star basis functions $\{\mathbf{j}_p^*\}$, introduced in Sec. 3.2.2 with coefficients $\alpha_{h,p}^{\parallel,*}$:

$$\mathbf{j}_h^\parallel = \sum_{p=1}^{N_t-1} \alpha_{h,p}^{\parallel,*} \mathbf{j}_p^*, \quad \mathbf{j}_h^\perp = \sum_{q=1}^{N_n-1} \alpha_{h,q}^{\perp,\circ} \mathbf{j}_q^\circ. \quad (4.19)$$

Thus, the numerical auxiliary eigenvalue problems are respectively, for longitudinal modes

$$\underline{\mathbb{T}}_0^{\parallel,**} \mathbf{J}_h^* = \gamma_h^\parallel \underline{\mathbb{R}}^{**} \mathbf{J}_h^*, \quad (4.20)$$

where

$$(\underline{\mathbb{T}}_0^{\parallel,**})_{pq} = \langle \mathbf{j}_p^*, \mathcal{T}_0^\parallel \mathbf{j}_q^* \rangle, \quad (\underline{\mathbb{R}}^{**})_{pq} = \langle \mathbf{j}_p^*, \mathbf{j}_q^* \rangle,$$

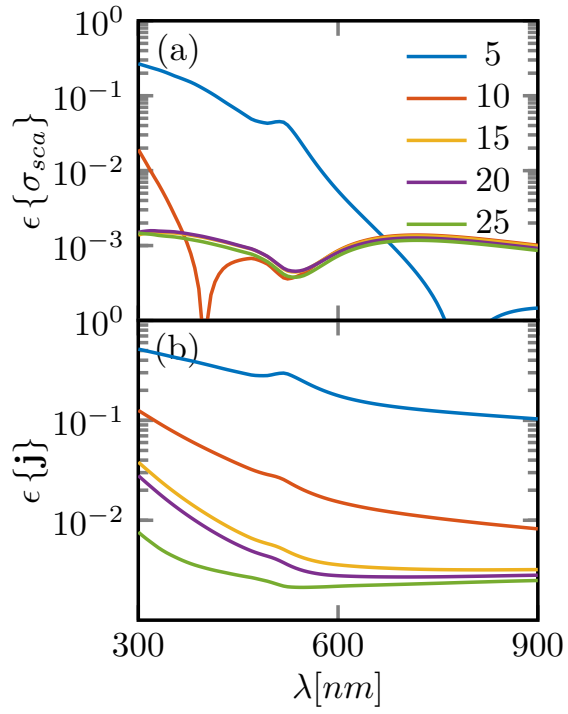


Figure 4.4 – Error made in the evaluation of the scattering efficiency $\epsilon[\sigma_{sca}]$ (a) and of the equivalent surface currents $\epsilon[\mathbf{j}]$ (b) obtained in the scattering from a gold particle $R = 100\text{nm}$ by using $N^{\parallel} = N^{\perp} = 5, 10, 15$ static modes (20, 40, 60 degrees of freedom) against corresponding quantities evaluated by using 999 loop and 1996 star functions (5998 degrees of freedom). In both cases a PMCHWT formulation is used. The sphere is excited by a linearly polarized plane wave as a function of the wavelength λ .

and for transverse modes

$$\underline{\mathbf{T}}_0^{\perp \circ \circ} \mathbf{J}_h^{\circ} = \gamma_h^{\perp} \underline{\mathbf{R}}^{\circ \circ} \mathbf{J}^{\circ}, \quad (4.21)$$

where

$$\left(\mathbf{T}^{\perp \circ \circ}\right)_{pq} = \langle \mathbf{j}_p^{\circ}, \mathcal{T}_0^{\perp} \mathbf{j}_q^{\circ} \rangle, \quad \left(\mathbf{R}^{\circ \circ}\right)_{pq} = \langle \mathbf{j}_p^{\circ}, \mathbf{j}_q^{\circ} \rangle.$$

Since the loop and star functions are not orthogonal, the matrices \mathbf{R}^{**} and $\mathbf{R}^{\circ \circ}$ and not identity matrices, thus problems 4.20 and 4.21 are generalized eigenvalue problems. Nevertheless, the involved matrices are real, symmetric, and positive definite. Thus, efficient numerical algorithms for the eigenvalue calculation do apply, such as the Cholesky factorization [103]. Moreover, the matrices properties also determine the orthogonality, at the discrete level, of any pair of longitudinal modes, and any pair of transverse modes. The numerical integration of shape functions times the Green's functions or its gradient are evaluated using the techniques introduced by R. Graglia [104].

4.3.2 Solution of the PMCWHT surface integral equation

Aiming at the solution of the PMCWHT surface integral equation 4.14, we represent any element of the space of transverse functions in term of the N^{\perp} transverse static modes $\{\mathbf{j}_p^{\perp}\}_{p=1 \dots N^{\perp}}$, associated with the low-order eigenvalues. Analogously, we represent any element of the space of longitudinal modes by the N^{\parallel} longitudinal static modes $\{\mathbf{j}_q^{\parallel}\}_{q=1 \dots N^{\parallel}}$ associated with low-order eigenvalues, namely:

$$\begin{cases} \mathbf{j}^e(\mathbf{r}) \approx \sum_{p=1}^{N^{\perp}} \alpha_p^{\perp} \mathbf{j}_p^{\perp}(\mathbf{r}) + \sum_{q=1}^{N^{\parallel}} \alpha_q^{\parallel} \mathbf{j}_q^{\parallel}(\mathbf{r}), \\ \mathbf{j}^m(\mathbf{r}) \approx \sum_{p=1}^{N^{\perp}} \beta_p^{\perp} \mathbf{j}_p^{\perp}(\mathbf{r}) + \sum_{q=1}^{N^{\parallel}} \beta_q^{\parallel} \mathbf{j}_q^{\parallel}(\mathbf{r}). \end{cases} \quad (4.22)$$

The reason behind this criterion is to select the modes according to the energy. We call N^{\parallel} and N^{\perp} longitudinal and transverse truncation numbers. Therefore, we define the unknown block vectors

$$\mathbf{J}_e = \left(\boldsymbol{\alpha}^{\perp} | \boldsymbol{\alpha}^{\parallel}\right)^{\mathbf{T}}, \quad \mathbf{J}_m = \left(\boldsymbol{\beta}^{\perp} | \boldsymbol{\beta}^{\parallel}\right)^{\mathbf{T}} \quad (4.23)$$

with

$$\left(\boldsymbol{\alpha}^a\right)_p = \alpha_p^a \quad p = 1 \dots N^a, \quad , \left(\boldsymbol{\beta}^a\right)_q = \beta_q^a \quad q = 1 \dots N^a, \quad (4.24)$$

with $a = \parallel, \perp$. We find the finite dimensional approximation of the PMCHWT problem (Eq. 4.14), by expanding the unknown surface current in terms of static longitudinal and transverse modes through Eq. 4.22 and by projecting along the same set of modes, accordingly to a Galerkin projection scheme. Eventually, we obtain:

$$\underline{\underline{\mathbf{Z}}}\mathbf{J} = \begin{pmatrix} \mathbf{E}_0 \\ \mathbf{H}_0 \end{pmatrix}, \quad (4.25)$$

where

$$\mathbf{J} = \begin{pmatrix} \mathbf{J}_e \\ \mathbf{J}_m \end{pmatrix}, \quad (4.26)$$

$$\underline{\underline{\mathbf{Z}}} = \begin{pmatrix} \zeta^- \underline{\underline{\mathbf{T}}}_- + \zeta^+ \underline{\underline{\mathbf{T}}}_+ & \underline{\underline{\mathbf{K}}}_- + \underline{\underline{\mathbf{K}}}_+ \\ -(\underline{\underline{\mathbf{K}}}_- + \underline{\underline{\mathbf{K}}}_+) & \underline{\underline{\mathbf{T}}}_-/\zeta^- + \underline{\underline{\mathbf{T}}}_+/\zeta^+ \end{pmatrix}, \quad (4.27)$$

$$\underline{\underline{\mathbf{T}}}_\pm = \begin{pmatrix} \underline{\underline{\mathbf{T}}}_\pm^{\perp,\perp} & | & \underline{\underline{\mathbf{T}}}_\pm^{\perp,\parallel} \\ \underline{\underline{\mathbf{T}}}_\pm^{\parallel,\perp} & | & \underline{\underline{\mathbf{T}}}_\pm^{\parallel,\parallel} \end{pmatrix}, \quad \underline{\underline{\mathbf{K}}}_\pm = \begin{pmatrix} \underline{\underline{\mathbf{K}}}_\pm^{\perp,\perp} & | & \underline{\underline{\mathbf{K}}}_\pm^{\perp,\parallel} \\ \underline{\underline{\mathbf{K}}}_\pm^{\parallel,\perp} & | & \underline{\underline{\mathbf{K}}}_\pm^{\parallel,\parallel} \end{pmatrix}, \quad (4.28)$$

$$(\underline{\underline{\mathbf{K}}}_\pm^{ab})_{pq} = \langle \mathbf{j}_p^a | \underline{\underline{\mathbf{K}}}_\pm | \mathbf{j}_q^b \rangle, \quad (\underline{\underline{\mathbf{T}}}_\pm^{ab})_{pq} = \langle \mathbf{j}_p^a | \underline{\underline{\mathbf{T}}}_\pm | \mathbf{j}_q^b \rangle, \quad (4.29)$$

$$\mathbf{E}_0 = (\mathbf{E}_0^\perp | \mathbf{E}_0^\parallel)^\top, \quad \mathbf{H}_0 = (\mathbf{H}_0^\perp | \mathbf{H}_0^\parallel)^\top, \quad (4.30)$$

and

$$(\mathbf{E}_0^a)_p = \langle \mathbf{j}_p^a, \mathbf{e}^{(0,t)} \rangle \quad (\mathbf{H}_0^a)_p = \langle \mathbf{j}_p^a, \mathbf{h}^{(0,t)} \rangle. \quad (4.31)$$

with $a, b = \parallel, \perp$. In conclusion, the finite dimensional system has $2(N^\parallel + N^\perp)$ degrees of freedom.

4.3.3 Static - Dynamic Green Decomposition

One of the main advantages in the use of the static basis can be understood if the Green function is decomposed as the sum of the static Green function and a regular difference term $g_{d\pm}$:

$$g_\pm(\mathbf{r} - \mathbf{r}') = g_0(\mathbf{r} - \mathbf{r}') + g_{d\pm}(\mathbf{r} - \mathbf{r}'), \quad (4.32)$$

where

$$g_{d\pm}(\mathbf{r} - \mathbf{r}') = \frac{e^{-i\frac{k^\pm}{2}|\mathbf{r}-\mathbf{r}'|}}{4\pi i} k_\pm \text{sinc} \left\{ \frac{k^\pm}{2} |\mathbf{r} - \mathbf{r}'| \right\}. \quad (4.33)$$

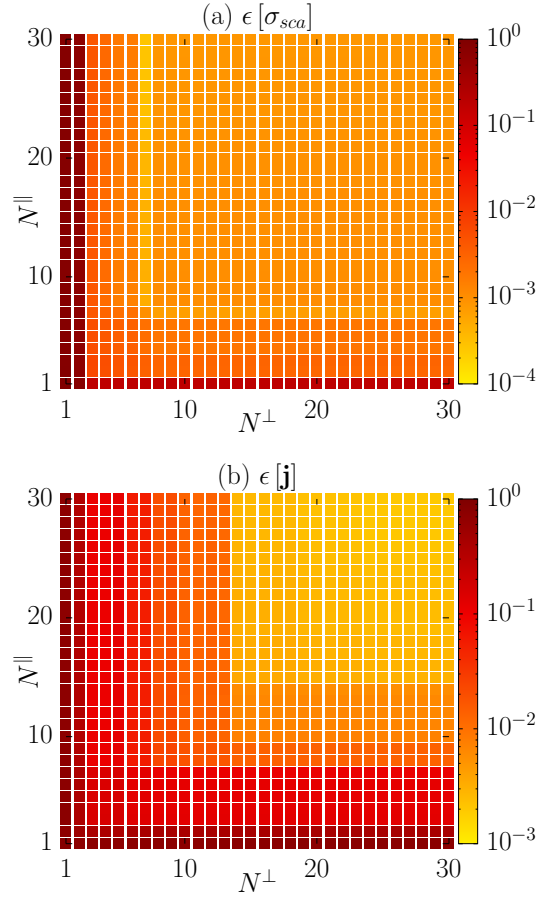


Figure 4.5 – Error in the evaluation of the scattering efficiency $\epsilon[\sigma_{sca}]$ (a) and of the equivalent surface currents $\epsilon[\mathbf{j}]$ (b) of the solution of the scattering problem from a gold particle $R = 100\text{nm}$ obtained by using an entire-domain basis constituted by N^{\parallel} longitudinal function and N^{\perp} transverse function against corresponding quantities evaluated by using loop-star basis functions (5998 degrees of freedom). In both cases a PMCHWT formulation is used. The sphere is excited by a linearly polarized plane wave at 620nm.

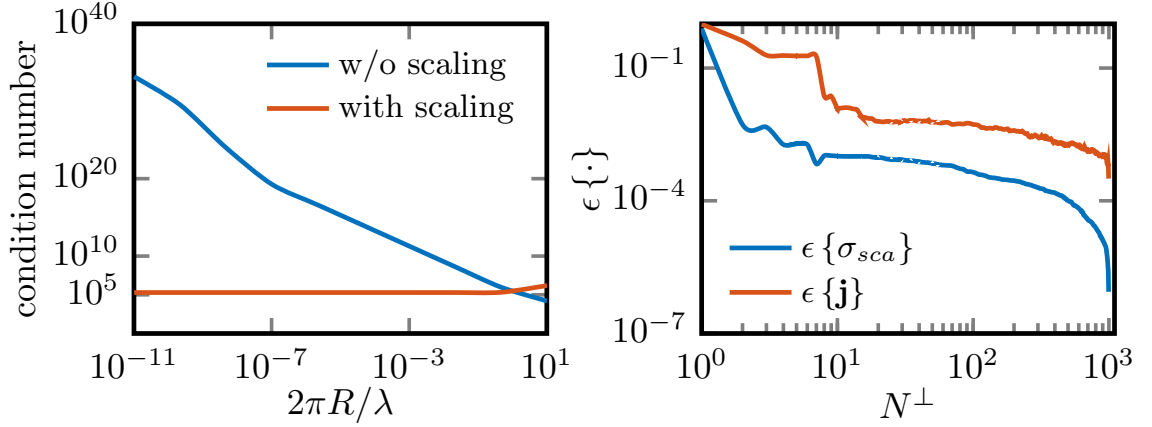


Figure 4.6 – (a) Condition number with and without basis rearrangement, as a function of the size parameter $2\pi R/\lambda$, assuming $N^{\parallel} = N^{\perp} = 15$. (b) Error $\epsilon[\sigma_{sca}]$ in the evaluation of the scattering efficiency (a) and of the equivalent currents $\epsilon[\mathbf{j}]$ (b) as a function of the number of static modes. The errors are evaluated against corresponding quantities evaluated by using 5998 loop-star basis functions. In both panels, we considered a gold sphere excited by a linearly polarized plane wave at $\lambda = 620nm$.

By applying the Green decomposition 4.32 into the operators \mathcal{T}_{\pm} and \mathcal{K}_{\pm} , defined in 4.17a and 4.17b, we obtain:

$$\begin{aligned}\mathcal{T}_{\pm} &= +\frac{1}{ik^{\pm}}\mathcal{T}_0^{\parallel} - ik^{\pm}\mathcal{T}_0^{\perp} + \mathcal{T}_{d\pm}, \\ \mathcal{K}_{\pm} &= \mathcal{K}_0 + \mathcal{K}_{d\pm},\end{aligned}\quad (4.34)$$

where $\mathcal{T}_0^{\parallel}$ and \mathcal{T}_0^{\perp} are the static operators defined in Eqs. 4.10 and 4.6, while we now define

$$\begin{aligned}\mathcal{T}_{d\pm}\{\mathbf{w}\}(\mathbf{r}) &= ik^{\pm}\hat{\mathbf{n}}\times\hat{\mathbf{n}}\times\int_S g_{d\pm}(\mathbf{r}-\mathbf{r}')\mathbf{w}(\mathbf{r}')dS' \\ &\quad -\frac{1}{ik^{\pm}}\hat{\mathbf{n}}\times\hat{\mathbf{n}}\times\int_S\nabla g_{d\pm}(\mathbf{r}-\mathbf{r}')\nabla'_S\cdot\mathbf{w}(\mathbf{r}')dS',\end{aligned}\quad (4.35)$$

$$\mathcal{K}_0\{\mathbf{w}\}(\mathbf{r}) = \hat{\mathbf{n}}\times\hat{\mathbf{n}}\times\int_S\mathbf{w}(\mathbf{r}')\times\nabla'g_0(\mathbf{r}-\mathbf{r}')dS',\quad (4.36)$$

$$\mathcal{K}_{d\pm}\{\mathbf{w}\}(\mathbf{r}) = \hat{\mathbf{n}}\times\hat{\mathbf{n}}\times\int_S\mathbf{w}(\mathbf{r}')\times\nabla'g_{d\pm}(\mathbf{r}-\mathbf{r}')dS'.\quad (4.37)$$

The above decomposition considerably simplifies the calculation of the finite dimensional operators \mathbb{T}_{\pm}^{ab} with $a, b = \parallel, \perp$, which are obtained by projecting the operator \mathcal{T}_{\pm} along the longitudinal and transverse static modes because the static modes \mathbf{j}_k^{\parallel}

and \mathbf{j}_k^\perp diagonalize the static operators \mathcal{T}_0^\perp and \mathcal{T}_0^\parallel :

$$\underline{\mathbb{T}} = \left(\begin{array}{c|c} \underline{\mathbb{T}}^{\perp\perp} & \underline{\mathbb{T}}^{\perp\parallel} \\ \hline \underline{\mathbb{T}}^{\parallel\perp} & \underline{\mathbb{T}}^{\parallel\parallel} \end{array} \right) = \quad (4.38)$$

$$\left(\frac{\langle \mathbf{j}_p^\perp, \mathcal{T}_\pm^\parallel \mathbf{j}_q^\perp \rangle}{\langle \mathbf{j}_p^\parallel, \mathcal{T}_\pm^\parallel \mathbf{j}_q^\perp \rangle} \middle| \frac{\langle \mathbf{j}_p^\perp, \mathcal{T}_\pm^\parallel \mathbf{j}_q^\parallel \rangle}{\langle \mathbf{j}_p^\parallel, \mathcal{T}_\pm^\parallel \mathbf{j}_q^\parallel \rangle} \right) + \left(\frac{\langle \mathbf{j}_p^\perp, \mathcal{T}_\pm^\perp \mathbf{j}_q^\perp \rangle}{\langle \mathbf{j}_p^\parallel, \mathcal{T}_\pm^\perp \mathbf{j}_q^\perp \rangle} \middle| \frac{\langle \mathbf{j}_p^\perp, \mathcal{T}_\pm^\perp \mathbf{j}_q^\parallel \rangle}{\langle \mathbf{j}_p^\parallel, \mathcal{T}_\pm^\perp \mathbf{j}_q^\parallel \rangle} \right) \quad (4.39)$$

Regarding the first term, the following simplifications can be made

$$\begin{aligned} \langle \mathbf{j}_p^\perp, \mathcal{T}_\pm^\parallel \{ \mathbf{j}_q^\perp \} \rangle &= \langle \mathbf{j}_p^\perp, \mathcal{T}_{d\pm}^\parallel \{ \mathbf{j}_q^\perp \} \rangle + \langle \mathbf{j}_p^\perp, \mathcal{T}_0^\parallel \{ \mathbf{j}_q^\perp \} \rangle \\ \nabla_S \cdot \mathbf{j}_q^\perp &= 0 \rightarrow \mathcal{T}_\pm^\parallel \{ \mathbf{j}_q^\perp \} = 0 \\ &= 0 \end{aligned} \quad (4.40)$$

$$\begin{aligned} \langle \mathbf{j}_p^\perp, \mathcal{T}_\pm^\parallel \{ \mathbf{j}_q^\parallel \} \rangle &= \langle \mathbf{j}_p^\perp, \mathcal{T}_{d\pm}^\parallel \{ \mathbf{j}_q^\parallel \} \rangle + \langle \mathbf{j}_p^\perp, \mathcal{T}_0^\parallel \{ \mathbf{j}_q^\parallel \} \rangle \\ \mathcal{T}_0^\parallel \{ \mathbf{j}_q^\parallel \} &= \frac{1}{ik^\pm} \gamma_q^\parallel \mathbf{j}_q^\parallel \rightarrow \\ &= \langle \mathbf{j}_p^\perp, \mathcal{T}_{d\pm}^\parallel \{ \mathbf{j}_q^\parallel \} \rangle + \frac{1}{ik^\pm} \gamma_q^\parallel \langle \mathbf{j}_p^\perp, \mathbf{j}_q^\parallel \rangle \\ &= \langle \mathbf{j}_p^\perp, \mathcal{T}_{d\pm}^\parallel \{ \mathbf{j}_q^\parallel \} \rangle \end{aligned} \quad (4.41)$$

$$\begin{aligned} \langle \mathbf{j}_p^\parallel, \mathcal{T}_\pm^\parallel \{ \mathbf{j}_q^\perp \} \rangle &= \langle \mathbf{j}_p^\parallel, \mathcal{T}_{d\pm}^\parallel \{ \mathbf{j}_q^\perp \} \rangle + \langle \mathbf{j}_p^\parallel, \mathcal{T}_0^\parallel \{ \mathbf{j}_q^\perp \} \rangle \\ \nabla_S \cdot \mathbf{j}_q^\perp &= 0 \rightarrow \mathcal{T}_\pm^\parallel \{ \mathbf{j}_q^\perp \} = 0 \\ &= 0 \end{aligned} \quad (4.42)$$

$$\begin{aligned} \langle \mathbf{j}_p^\parallel, \mathcal{T}_\pm^\parallel \{ \mathbf{j}_q^\parallel \} \rangle &= \langle \mathbf{j}_p^\parallel, \mathcal{T}_{d\pm}^\parallel \{ \mathbf{j}_q^\parallel \} \rangle + \langle \mathbf{j}_p^\parallel, \mathcal{T}_0^\parallel \{ \mathbf{j}_q^\parallel \} \rangle \\ \mathcal{T}_0^\parallel \{ \mathbf{j}_q^\parallel \} &= \frac{1}{ik^\pm} \gamma_q^\parallel \mathbf{j}_q^\parallel \rightarrow \\ &= \langle \mathbf{j}_p^\parallel, \mathcal{T}_{d\pm}^\parallel \{ \mathbf{j}_q^\parallel \} \rangle + \frac{1}{ik^\pm} \gamma_q^\parallel \langle \mathbf{j}_p^\parallel, \mathbf{j}_q^\parallel \rangle \\ &= \langle \mathbf{j}_p^\parallel, \mathcal{T}_{d\pm}^\parallel \{ \mathbf{j}_q^\parallel \} \rangle + \frac{1}{ik^\pm} \gamma_q^\parallel \delta_{pq} \|\mathbf{j}_q^\parallel\|^2 \end{aligned} \quad (4.43)$$

Regarding the second term, instead, it is possible to make the following simplifications

$$\begin{aligned} \langle \mathbf{j}_p^\perp, \mathcal{T}_\pm^\perp \{ \mathbf{j}_q^\perp \} \rangle &= \langle \mathbf{j}_p^\perp, \mathcal{T}_{d\pm}^\perp \{ \mathbf{j}_q^\perp \} \rangle + \langle \mathbf{j}_p^\perp, \mathcal{T}_0^\perp \{ \mathbf{j}_q^\perp \} \rangle \\ \mathcal{T}_0^\perp \{ \mathbf{j}_q^\perp \} &= ik^\pm \gamma_q^\perp \mathbf{j}_q^\perp \rightarrow \\ &= \langle \mathbf{j}_p^\perp, \mathcal{T}_{d\pm}^\perp \{ \mathbf{j}_q^\perp \} \rangle + ik^\pm \gamma_q^\perp \langle \mathbf{j}_p^\perp, \mathbf{j}_q^\perp \rangle \\ &= \langle \mathbf{j}_p^\perp, \mathcal{T}_{d\pm}^\perp \{ \mathbf{j}_q^\perp \} \rangle + ik^\pm \gamma_q^\perp \delta_{pq} \|\mathbf{j}_q^\perp\|^2 \end{aligned} \quad (4.44)$$

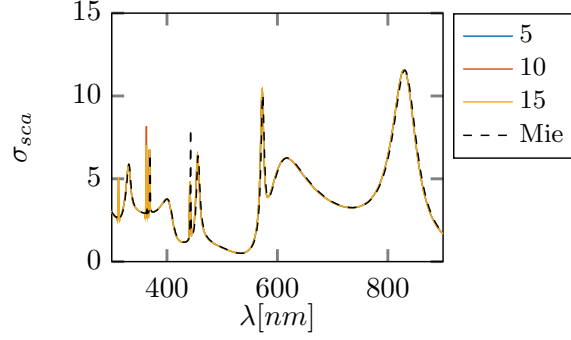


Figure 4.7 – Scattering efficiency σ_{sca} of a silicon particle with $R = 100\text{nm}$ excited by a linearly polarized plane wave in the visible spectral range evaluated by the PMCHWT with a static basis with an increasing number of longitudinal and transverse static modes with $N^{\parallel} = N^{\perp} = 5, 10, 15$. The reference Mie solution (black dashed line) is also shown for comparison.

$$\langle \mathbf{j}_p^{\perp}, \mathcal{T}_{\pm}^{\perp} \{ \mathbf{j}_q^{\parallel} \} \rangle = \langle \mathbf{j}_p^{\perp}, \mathcal{T}_{d\pm}^{\perp} \{ \mathbf{j}_q^{\parallel} \} \rangle + \langle \mathbf{j}_p^{\perp}, \mathcal{T}_0^{\perp} \{ \mathbf{j}_q^{\parallel} \} \rangle \quad (4.45)$$

$$\begin{aligned} \langle \mathbf{j}_p^{\parallel}, \mathcal{T}_{\pm}^{\perp} \{ \mathbf{j}_q^{\perp} \} \rangle &= \langle \mathbf{j}_p^{\parallel}, \mathcal{T}_{d\pm}^{\perp} \{ \mathbf{j}_q^{\perp} \} \rangle + \langle \mathbf{j}_p^{\parallel}, \mathcal{T}_0^{\perp} \{ \mathbf{j}_q^{\perp} \} \rangle \\ \mathcal{T}_0^{\perp} \{ \mathbf{j}_q^{\perp} \} &= ik^{\pm} \gamma_q^{\perp} \mathbf{j}_q^{\perp} \rightarrow \\ &= \langle \mathbf{j}_p^{\parallel}, \mathcal{T}_{d\pm}^{\perp} \{ \mathbf{j}_q^{\perp} \} \rangle + ik^{\pm} \gamma_q^{\perp} \langle \mathbf{j}_p^{\parallel}, \mathbf{j}_q^{\perp} \rangle \\ &= \langle \mathbf{j}_p^{\parallel}, \mathcal{T}_{d\pm}^{\perp} \{ \mathbf{j}_q^{\perp} \} \rangle \end{aligned} \quad (4.46)$$

$$\langle \mathbf{j}_p^{\parallel}, \mathcal{T}_{\pm}^{\parallel} \{ \mathbf{j}_q^{\parallel} \} \rangle = \langle \mathbf{j}_p^{\parallel}, \mathcal{T}_{d\pm}^{\parallel} \{ \mathbf{j}_q^{\parallel} \} \rangle + \langle \mathbf{j}_p^{\parallel}, \mathcal{T}_0^{\parallel} \{ \mathbf{j}_q^{\parallel} \} \rangle \quad (4.47)$$

where $\delta_{p,q}$ is the Kronecker delta. We point out that the numerical computation of the terms $\langle \mathbf{j}_p^{\parallel}, \mathcal{T}_{d\pm}^{\perp} \{ \mathbf{j}_q^{\perp} \} \rangle$ is straightforward, since their kernels are regular functions. These terms are the only ones depending on the operating frequency.

In conclusion, the decomposition of the Green function into the sum of a static term and of a regular difference term relieves us from the task of computing almost all the integrals with (integrable) singularity, which usually results in longer computational time compared to their regular counterpart. There are however two exceptions: $\langle \mathbf{j}_p^{\parallel}, \mathcal{T}_0^{\perp} \{ \mathbf{j}_q^{\perp} \} \rangle$ and $\langle \mathbf{j}_p^a, \mathcal{K}_0^{\perp} \{ \mathbf{j}_q^b \} \rangle$, $\forall a, b \in \perp, \parallel$. These terms are frequency-independent, thus when the calculation of the scattering response of an object for multiple frequencies of the exciting field is required they can be conveniently pre-calculated and stored away, while only the regular terms must be calculated for any frequencies.

4.3.4 Low-frequency analysis

As anticipated in Sec. 3.2 surface integral formulations may suffer from ill-conditioning due to low frequency breakdown. The low frequency breakdown phe-

nomenon manifests when the operating wavelength is much larger than the dimension of the object [83], and originates from the different frequency-scaling of the terms associated with the vector and the scalar potentials. In this section, we summarize the behaviour of the PMCHWT at very low frequencies. In this limit, the frequency dependence of the elements of the matrix Z follows different scaling laws, which are easily determined by following Ref. [89]

$$\begin{pmatrix} \underline{\underline{T}}_{\pm}^{\perp\perp} & \underline{\underline{T}}_{\pm}^{\parallel\perp} \\ \underline{\underline{T}}_{\pm}^{\perp\parallel} & \underline{\underline{T}}_{\pm}^{\parallel\parallel} \end{pmatrix} \xrightarrow{\omega \downarrow 0} \begin{pmatrix} -ik^{\pm}\underline{\underline{\Gamma}}_{\pm}^{\perp} & i(k^{\pm})^3\underline{\underline{T}}_2^{\parallel\perp} \\ i(k^{\pm})^3\underline{\underline{T}}_2^{\perp\parallel} & +\underline{\underline{\Gamma}}_{\pm}^{\parallel}/ik^{\pm} \end{pmatrix} \quad (4.48)$$

$$\begin{pmatrix} \underline{\underline{K}}_{\pm}^{\perp\perp} & \underline{\underline{K}}_{\pm}^{\perp\parallel} \\ \underline{\underline{K}}_{\pm}^{\parallel\perp} & \underline{\underline{K}}_{\pm}^{\parallel\parallel} \end{pmatrix} \xrightarrow{\omega \downarrow 0} \begin{pmatrix} (k^{\pm})^2\underline{\underline{K}}_2^{\perp\perp} & \underline{\underline{K}}_0^{\parallel\perp} \\ \underline{\underline{K}}_0^{\perp\parallel} & \underline{\underline{K}}_0^{\parallel\parallel} \end{pmatrix} \quad (4.49)$$

where $\underline{\underline{\Gamma}}^{\perp}$ and $\underline{\underline{\Gamma}}^{\parallel}$ are diagonal matrices,

$$\begin{aligned} \underline{\underline{\Gamma}}^{\perp} &= \text{diag} \left\{ \gamma_1^{\perp}, \gamma_2^{\perp}, \dots, \gamma_{N^{\perp}}^{\perp} \right\}, \\ \underline{\underline{\Gamma}}^{\parallel} &= \text{diag} \left\{ \gamma_1^{\parallel}, \gamma_2^{\parallel}, \dots, \gamma_{N^{\parallel}}^{\parallel} \right\}, \end{aligned} \quad (4.50)$$

$$T_2^{\parallel\perp} = \frac{1}{8\pi} \int_S \mathbf{j}_p^{\perp}(\mathbf{r}) \cdot \int_S |\mathbf{r} - \mathbf{r}'| \mathbf{j}_q^{\perp}(\mathbf{r}') dS dS', \quad (4.51)$$

$$K_2^{\perp\perp} = -\frac{1}{8\pi} \int_S \mathbf{j}_p^{\perp}(\mathbf{r}) \cdot \int_S \frac{(\mathbf{r} - \mathbf{r}')}{|\mathbf{r} - \mathbf{r}'|} \times \mathbf{j}_q^{\perp}(\mathbf{r}') dS dS' \quad (4.52)$$

Thus, by using Eqs. 4.48-4.49 it easy to prove that, in the static limit, the discrete matrix $\underline{\underline{Z}}$ approaches the matrix $\underline{\underline{Z}}_0$ which exhibits the following frequency dependence:

$$\underline{\underline{Z}}_0 \propto \begin{bmatrix} \mathcal{O}(\omega) & \mathcal{O}(\omega^3) & \mathcal{O}(\omega^2) & \mathcal{O}(1) \\ \mathcal{O}(\omega^3) & \mathcal{O}(\omega^{-1}) & \mathcal{O}(1) & \mathcal{O}(1) \\ \mathcal{O}(\omega^2) & \mathcal{O}(1) & \mathcal{O}(\omega) & \mathcal{O}(\omega^3) \\ \mathcal{O}(1) & \mathcal{O}(1) & \mathcal{O}(\omega^3) & \mathcal{O}(\omega^{-1}) \end{bmatrix} \quad (4.53)$$

The excitation vector associated with a plane wave exhibits the following dependencies [89]:

$$\begin{pmatrix} \mathbf{E}_0^{\perp} \\ \mathbf{E}_0^{\parallel} \\ \mathbf{H}_0^{\perp} \\ \mathbf{H}_0^{\parallel} \end{pmatrix} \propto \begin{pmatrix} \mathcal{O}(k_0) \\ \mathcal{O}(1) \\ \mathcal{O}(k_0) \\ \mathcal{O}(1) \end{pmatrix}. \quad (4.54)$$

Thus, following [89] we introduce the following rearrangement and scaling of the basis

$$\tilde{\underline{\underline{Z}}} = \underline{\underline{D}}_1 \underline{\underline{Z}} \underline{\underline{D}}_2, \quad (4.55)$$

where

$$\begin{aligned} \underline{\underline{D}}_1 &= \text{diag} \left\{ k_-^{-1} \mathbf{I}_{N^\perp}, \mathbf{I}_{N^\parallel}, k_-^{-1} \mathbf{I}_{N^\perp}, \mathbf{I}_{N^\parallel} \right\}, \\ \underline{\underline{D}}_2 &= \text{diag} \left\{ \mathbf{I}_{N^\perp}, ik_- \mathbf{I}_{N^\parallel}, \mathbf{I}_{N^\perp}, ik_- \mathbf{I}_{N^\parallel} \right\}. \end{aligned} \quad (4.56)$$

where \mathbf{I}_{N^\perp} is the the $N^\perp \times N^\perp$ identity matrix, and \mathbf{I}_{N^\parallel} is the $N^\parallel \times N^\parallel$ identity matrix. After the above rearrangement the matrix $\tilde{\underline{\underline{Z}}}$ is well-behaved.

4.4 Results and Discussion

We introduce a triangular surface mesh for S with N_n nodes and N_t triangular elements, then we precompute the longitudinal and static modes of a sphere, using $N^* = N_t - 1$ star and $N^\circ = N_n - 1$ loop functions respectively, by solving the auxiliary eigenvalue problems 4.20 and 4.21. We assembly a finite-dimensional basis by only considering the static modes associated to the low-order N^\parallel longitudinal and N^\perp transverse eigenvalues. The discrete PMCHWT impedance matrix \mathbf{Z} is then assembled, where static part of the operators lying on the block-diagonal are diagonalized. The resulting complex and non-hermitian matrix has dimension $2(N^\parallel + N^\perp)$ and it is inverted by LU decomposition (unless explicitly stated), once the excitation conditions are assigned.

4.4.1 Scattering from a sphere

We first consider the scattering from a sphere, which have an analytical solution [105, 15] and also analytical expression for the eigenvalues and for the static modes.

Generation of the static basis

Thus, with the help of Fig. 4.1 we study the convergence of the eigenvalues $\{\gamma_h^\parallel\}$ and $\{\gamma_k^\perp\}$ against their analytical counterpart as a function of the triangular mesh density. The convergence is good. From now on, we consider the static basis calculated using a triangular mesh with $N_n = 1000$, $N_t = 1996$. Thus, the longitudinal static modes are represented in terms of $N_t - 1 = 1995$ star functions, while the transverse static modes are represented by $N_p - 1 = 999$ loop functions.

Numerical Orthogonality and Gram matrices

In the discrete problem, the orthogonality between any pair of longitudinal modes and between any pair of transverse modes is always guaranteed, because the matrices $T^{\circ\circ}$ and T^{**} are real and symmetric. This property is indeed verified at the numerical level with machine precision. Instead, even if theoretically we expect that the mutual product between a transverse and a longitudinal static mode is vanishing, this fact is only approximately numerically verified, since the sub-domain basis function used to represent the longitudinal modes are no rigorously curl-free [85]. Thus, it is worth calculating the Gram matrix G , whose occurrences are defined as

$$g_{hk} = \langle \mathbf{j}_h^\perp, \mathbf{j}_k^\parallel \rangle \quad (4.57)$$

In Fig. 4.2 are reported the first 100×100 occurrences of the Gram Matrix. The maximum occurrence of this matrix is 0.024.

Gold sphere

We now use the static modes to solve the scattering problem from a gold sphere of radius $R = 100\text{nm}$ in the visible and near infrared spectral range $[300, 900]\text{nm}$. At these frequencies, a metal sphere may undergo plasmonic resonances, which have an electrostatic origin [94]. We describe the gold permittivity by interpolating experimental data [106]. The sphere is excited by a linearly polarized plane wave. We solve the PMCHWT by varying the numbers N^\parallel and N^\perp of employed longitudinal and transverse static functions, respectively. Figure 4.3 shows the scattering efficiency σ_{sca} as a function of the wavelength of the exciting plane wave. The scattering efficiency is defined as the scattering cross section normalized by the geometrical cross section G which, in this case, is $G = \pi R^2$ [15]. We consider different numerical solutions, obtained by increasing the truncation numbers, i.e. $N^\parallel = N^\perp = 5, 10, 15$. The reference Mie solution [15] (black dashed line) is also shown for comparison. For $N^\parallel = N^\perp = 5$, the numerical solution is in good agreement with the reference solution only in the long-wavelength regime, while it shows a slight disagreement when the operating wavelength becomes comparable with the sphere's radius. Increasing the truncation number to $N^\parallel = N^\perp = 10$, we obtain a good agreement over the whole investigated spectrum. In this latter case, the inversion of a 40×40 matrix is required (at each frequency). We now present a more systematic analysis of the error. In particular, we define the relative error on the scattering efficiency

$$\epsilon[\sigma_{sca}] = |\sigma_{sca} - \tilde{\sigma}_{sca}| / \tilde{\sigma}_{sca}, \quad (4.58)$$

where $\tilde{\sigma}_{sca}$ is the reference solution which computed by solving the PMCHWT problem by representing the electric and magnetic equivalent surface current in terms of $N^\circ = 999$ loop functions and $N^* = 1995$ star functions, associated with the same mesh used for the static modes generation, which correspond to 5998 degrees of freedom. In Fig. 4.4 (a) we plot $\epsilon[\sigma_{sca}]$ as a function of the wavelength of the incident field, by varying the truncation numbers $N^\parallel = N^\perp$. We note that for $N^\parallel = N^\perp \geq 10$ the achieved error is lower than 0.002 all over the investigated spectral range. The error does not appreciably decrease if the truncation number $N^\parallel = N^\perp$ is increased from 15 to 25. Then, we investigate the error in the evaluation of the equivalent surface currents induced on S, which are the unknowns of the PMCHWT problem. They are immediately related to the total electric field on the surface of the object, which has a great importance in nano-optics applications [27]. Thus, we define this relative error as:

$$\epsilon[\mathbf{J}] = \|\mathbf{J} - \tilde{\mathbf{J}}\|_2 / \|\tilde{\mathbf{J}}\|_2, \quad (4.59)$$

where $\tilde{\mathbf{J}}$ is the reference loop/star solutions and $\|\cdot\|_2$ is the Euclidean norm. In Fig. 4.4 (b), we show the quantity $\epsilon[\mathbf{j}]$ as a function of the wavelength. Compared to panel (a), it is apparent that more static basis functions are needed to reach smaller errors. Also in this case, we observe a saturation of the error. We further delve into error analysis by monitoring in Fig. 4.5 the same two relative errors $\epsilon[\sigma_{sca}]$ and $\epsilon[\mathbf{j}]$, by *independently* varying the truncation numbers N^\parallel and N^\perp . This analysis is carried out in correspondence of the σ_{sca} peak (see Fig. 4.3) occurring at $\lambda = 620\text{nm}$. The two colormaps are almost symmetric (along the principal diagonal): This fact suggests that for practical applications is convenient to keep $N^\parallel = N^\perp$. Figure 4.5 (a) shows that it is sufficient to consider $N^\parallel = N^\perp = 3$ (12 degrees of freedom in total) to achieve an error below 0.02. As in the previous analysis, given the same pair of truncation numbers N^\parallel, N^\perp , the error $\epsilon[\mathbf{j}]$ is higher than $\epsilon[\sigma_{sca}]$. Specifically, we need to consider $N^\parallel = N^\perp = 10$ (40 degrees of freedom in total) to achieve an error $\epsilon[\mathbf{j}]$ below 0.02. It also apparent from the colormaps that the error undergoes sudden "jumps" in correspondence to specific values of the truncation number, namely, when a specific static mode (needed for a correct description of the solution) is included in the current density expansion. We also observe a *saturation* of the error level for high values of N^\parallel, N^\perp , namely an increase of the number of static basis function does not correspond to an appreciable decrease of the error. In Fig. 4.6 (a), we show the condition number of the PMCHWT problem with and without the rearrangement of the basis described in section 4.3.4 as a function of the sphere radius R , while the wavelength of the exciting plane wave is kept constant to 620nm. It is apparent that without a basis rearrangement the PMCHWT problem experience

an exponential increase of the condition number which is symptomatic of the low-frequency breakdown problem. By rearranging the basis, the condition number is kept constant over the whole investigated range of size parameters. In Fig. 4.6 (b) the errors $\epsilon\{\sigma_{sca}\}$ and $\epsilon\{\mathbf{j}\}$ are shown as a function of the truncation number N^\perp , by assuming $N^\parallel = 2N^\perp$. This choice guarantees that when $N^\perp = 997$ $N^\parallel = 1994$, and almost all available basis functions are employed. This analysis is carried out in correspondence of the σ_{sca} peak at $\lambda = 620\text{nm}$. Both the errors exhibit a similar trend, showing a rapid decrease for $N^\perp < 10$, which is then followed by a region of very slow decrease (saturation). Eventually, for very large values of N^\perp , the error rapidly decreases again.

High-permittivity sphere

We now consider a high permittivity sphere, assumed to be homogeneous, isotropic, non-dispersive in time with relative permittivity $\epsilon_R = 16$. Sub-wavelength particles of sufficiently high permittivity - as the one under consideration - may support magnetostatic scattering resonances [96]. These resonances arise from the interplay of the polarization energy of the dielectric and the energy stored in the magnetic field [96, 98]. This fact allows us to explore the numerical accuracy of the static basis in a complementary regime to the one of the plasmonic resonances occurring in metals. In Fig. 4.7, we calculate the scattering efficiency σ_{sca} as a function of the wavelength of the exciting, linearly polarized, plane wave. We consider different solutions computed using increasing truncation numbers $N^\parallel = N^\perp$. We use as a reference the analytic Mie solution [105, 15], shown with a black dashed line. For $N^\parallel = N^\perp = 5$ even if a good agreement is found at low frequency, the accuracy of the solution rapidly deteriorates at higher frequencies, and it is unable to describe every peak of the scattering response. By increasing the truncation numbers to $N^\parallel = N^\perp = 10$, we obtain a very good agreement over the whole investigated spectrum.

We now quantify the errors in the scattering efficiency and in the surface currents made by solution in terms of static modes. In Fig. 4.8 (a) we plot $\epsilon[\sigma_{sca}]$ as a function of the incident wavelength, assuming different truncation numbers with the constraint $N^\perp = N^\parallel$. When $N^\perp = N^\parallel = 5$, the error is acceptable as long as the incident wavelength is much larger than the dimension of the object, then the error suddenly increases for wavelengths below 600nm. By assuming a truncation number $N^\perp = N^\parallel = 10$, we obtain a low error all over the investigated spectrum. Only in correspondence of the resonances the error slightly exceeds 0.01. A further increase in the number of basis functions improves the convergence, especially in the neighborhood of the resonance peaks. In the analysis carried out in Fig. 4.9 the error is evaluated

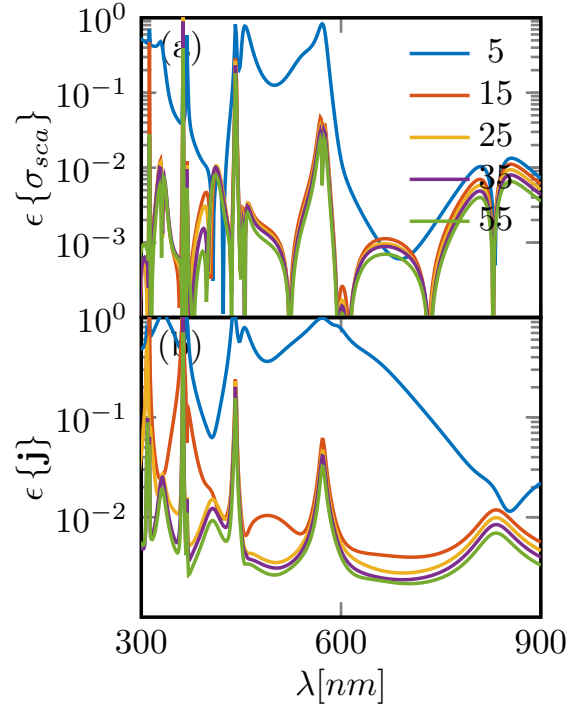


Figure 4.8 – Error ϵ in the evaluation of the scattering efficiency σ_{sca} (a) and of the equivalent surface currents \mathbf{j} (b) of a sphere with $\epsilon_R = 16$ and $R = 100\text{nm}$ by using a entire-domain basis constituted by $N^{\parallel} = N^{\perp} = 5, 10, 15$ static modes. The solution evaluated by using loop/star sub-domain basis function was assumed as a reference. In both cases a PMCHWT formulation is used (5998 degrees of freedom). The sphere is excited by a linearly polarized plane wave as a function of the wavelength λ .

as a function of two truncation numbers N^{\parallel} and N^{\perp} which are now assumed as independent. This analysis is carried out at the wavelength $\lambda = 620\text{nm}$, which corresponds to the low frequency peak (first peak from the right) of the scattering cross section, where the magnetic dipole mode resonates. In Fig. 4.9 (a) we show the error on the scattering efficiency $\epsilon[\sigma_{sca}]$, in 4.9 (b) the error on the equivalent surface currents $\epsilon[\mathbf{j}]$. The two colormaps are, with good approximation, symmetric with respect to the main diagonal. This fact suggests that for practical applications is reasonable to choose $N^{\parallel} = N^{\perp}$. For the scattering cross section by choosing $N^{\parallel} = N^{\perp} = 3$ we reach an error below 0.01. The error in the determination of the electric and magnetic currents is in general higher, and $N^{\parallel} = N^{\perp} = 8$ are needed to achieve $\epsilon[\mathbf{j}] < 0.1$. In both panels, we observe an error saturation for large truncation numbers. In Fig. 4.10 (a), we show the condition number of the PMCHWT problem with and without the rearrangement of the basis described in section 4.3.4 as a function of the sphere radius R , while the wavelength of the exciting plane wave is kept constant to 620nm. As for metal sphere, by rearranging the basis, we are able to keep the condition number constant over the whole investigated range of size parameters by rearranging and scaling of the basis. In Fig. 4.10 (b) the errors $\epsilon\{\sigma_{sca}\}$ and $\epsilon\{\mathbf{j}\}$ are shown as a function of the truncation number N^{\perp} , by assuming $N^{\parallel} = 2N^{\perp}$. This analysis is carried out in correspondence of the σ_{sca} peak at $\lambda = 620\text{nm}$. Both the errors exhibit a similar trend, showing a rapid decrease for $N^{\perp} > 10$, which is then followed by a region of very slow decrease (saturation). Eventually, for very large values of N^{\perp} , the error rapidly decreases.

4.4.2 Rod

We now consider a non-canonical shape, namely a three-dimensional rod. We model this shape as a superellipsoid, whose boundary has the implicit equation

$$\left(\frac{x}{a}\right)^r + \left(\frac{y}{b}\right)^r + \left(\frac{z}{c}\right)^r = 1, \quad (4.60)$$

with $b = 0.5a$, $c = 0.25a$, and $r = 6$. We used the public domain code developed by Per-Olof Persson and Gilbert Strang [107] to generate a surface mesh for this implicit surface. The resulting mesh that we consider thought this section features 1000 nodes, 1996 triangular elements. The first 16 longitudinal and 16 transverse static modes are shown in Fig. 4.11 and 4.12, respectively. The modes are shown in a lexicographic order, sorted accordingly to their static eigenvalue.

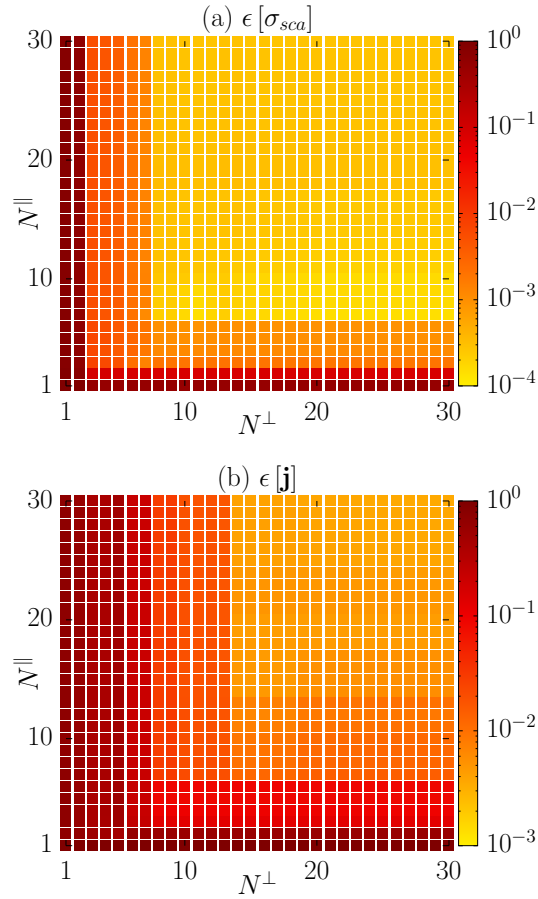


Figure 4.9 – Error ϵ in the evaluation of the scattering efficiency σ_{sca} (a) and of the equivalent \mathbf{j} surface currents (b) of a silicon particle with $R = 100\text{nm}$ computed by using an entire-domain basis constituted by $N^{\parallel} = N^{\perp} = 5, 10, 15$ static modes against corresponding quantities evaluated by using loop-star functions (5998 degrees of freedom). In both cases a PMCHWT formulation is used. The sphere is excited by a linearly polarized plane wave as a function of the wavelength λ .

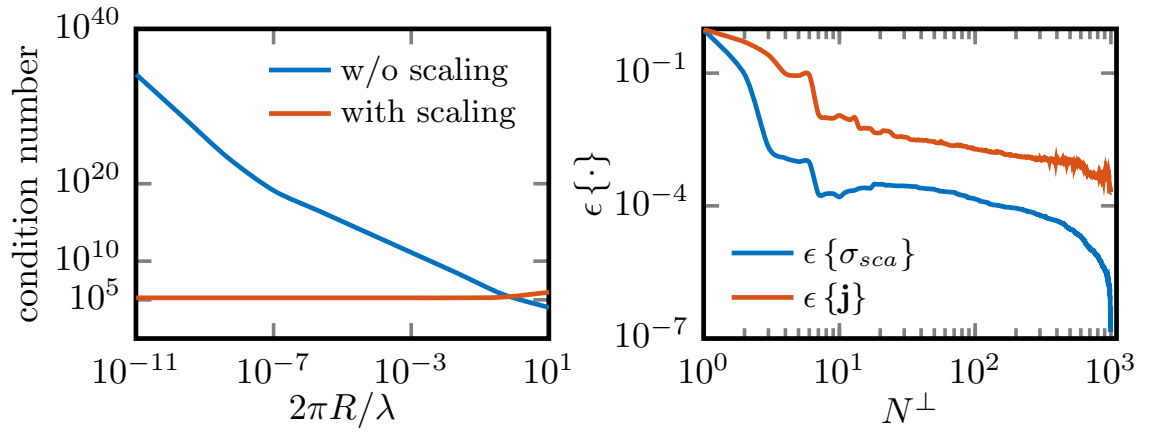


Figure 4.10 – (a) Condition number with and without basis rearrangement, as a function of the size parameter $2\pi R/\lambda$, assuming $N^{\parallel} = N^{\perp} = 15$. (b) Error ϵ in the evaluation of the scattering efficiency σ_{sca} (a) and of the equivalent currents \mathbf{j} as a function of the truncation number N^{\perp} (assuming $N^{\parallel} = 2N^{\perp}$). The error is evaluated against corresponding quantities obtained by using loop-star basis functions (5998 degrees of freedom). In both panels, we consider a Si sphere excited by a linearly polarized plane wave at $\lambda = 620\text{nm}$.

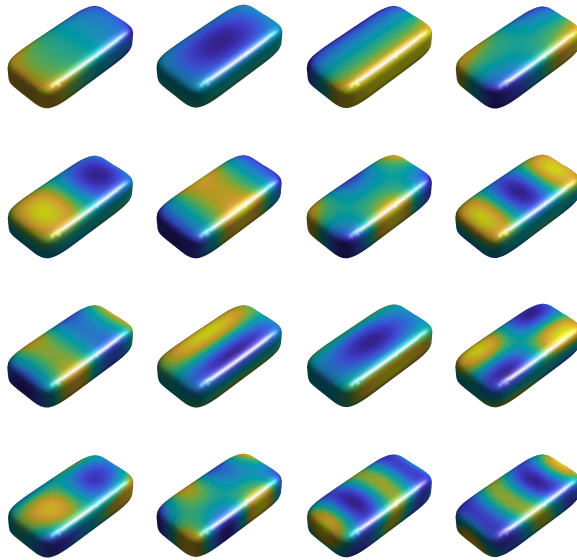


Figure 4.11 – Longitudinal static modes of a rod with semi-axis 1 : 0.5 : 0.25. The modes are shown in lexicographic order, sorted accordingly to their static eigenvalue. The first 16 modes are shown.

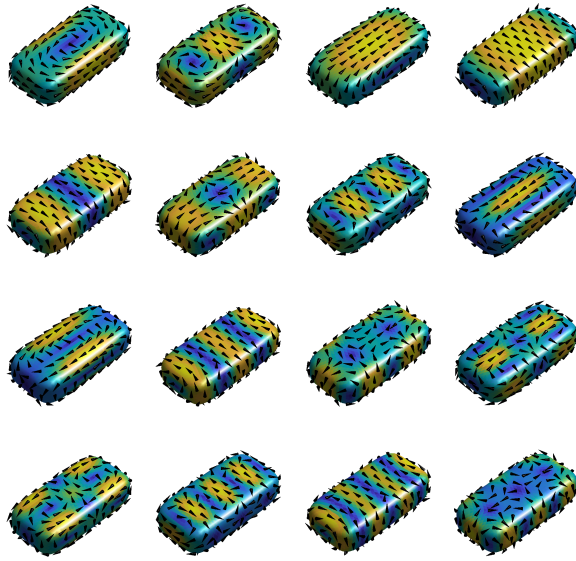


Figure 4.12 – Transverse static modes of a rod with semi-axis $1 : 0.5 : 0.25$. The modes are shown in a lexicographic order, sorted accordingly to their static eigenvalue. The first 16 modes are shown.

Plasmon Rod

First, we investigate a gold rod with $a = 100\text{nm}$, excited by a plane wave linearly polarized along the direction $(\hat{\mathbf{x}} + \hat{\mathbf{y}})/\sqrt{2}$ and propagating along the $\hat{\mathbf{z}}$ axis. The gold's dispersion relation ε_R^+ has been described using experimental data [106]. In Fig. 4.11 we plot the spectrum of the scattering efficiency σ_{sca} , obtained by increasing the truncation numbers $N^\perp = N^\parallel = 5, 10, 15$. We take as reference the loop/star solution obtained by describing the unknowns in terms of a total number of 5984 degrees of freedom. Only five longitudinal and transverse modes (20 total degrees of freedom) are sufficient to achieve a very good agreement with the reference solution over the whole investigated spectrum, demonstrating a drastic reduction of the total number of unknowns. In Fig. 4.14, we carry out a more systematic analysis of the error (a) on the scattering cross section $\epsilon[\sigma_{sca}]$, and (b) on the equivalent surface currents $\epsilon[\mathbf{j}]$. Overall, the errors are slightly higher than in the case of a sphere. Besides that, as in the previous numerical experiments, we conclude that i) the error on the surface currents are one order of magnitude higher than the error on the scattering efficiency, and ii) the different errors saturate for large values of the truncation number.

High-permittivity Rod

Eventually, we investigate a high-permittivity rod. The relative permittivity of the rod is assumed constant over the investigated frequency spectrum to the value $\varepsilon_R =$

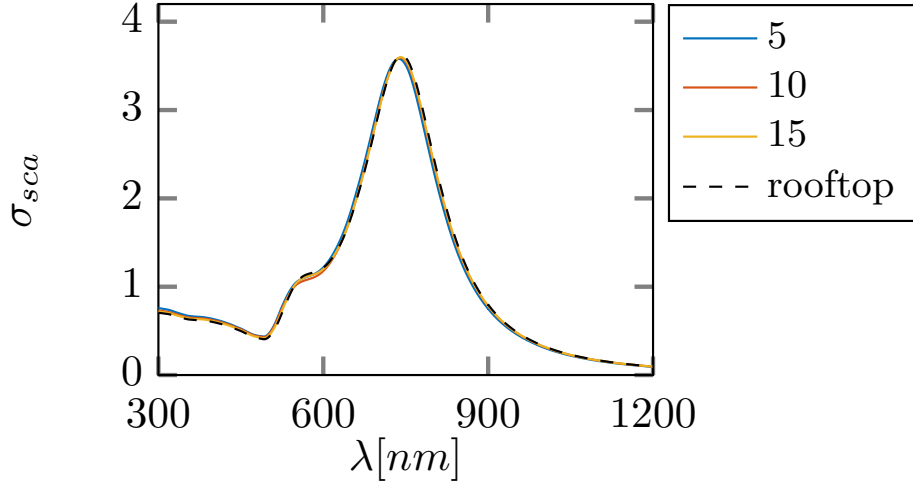


Figure 4.13 – Scattering efficiency σ_{sca} of gold rod with semi-axis $a = 100nm$, $b = 0.5a$, and $c = 0.25a$ evaluated with an increasing number of longitudinal and transverse static modes $N^{\parallel} = N^{\perp} = 5, 15, 25, 35, 55$. The rod is excited by a linearly polarized plane wave in the visible spectral range. The reference loop-star solution (black dashed line) is also shown for comparison.

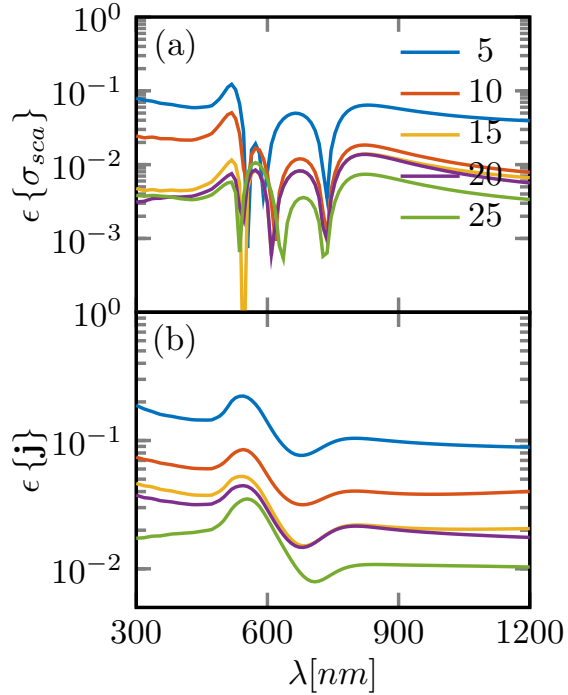


Figure 4.14 – Error ϵ in the evaluation of the scattering efficiency σ_{sca} and of the equivalent surface current density of a gold rod with semi-axis $a = 100nm$, $b = 0.5a$, and $c = 0.25a$ by using an increasing number of longitudinal and transverse static modes $N^{\parallel} = N^{\perp} = 5, 15, 20, 25$ ($4N^{\parallel}$ total degrees of freedom). The solution evaluated by using loop/star sub-domain basis function was assumed as a reference (5988 degrees of freedom).

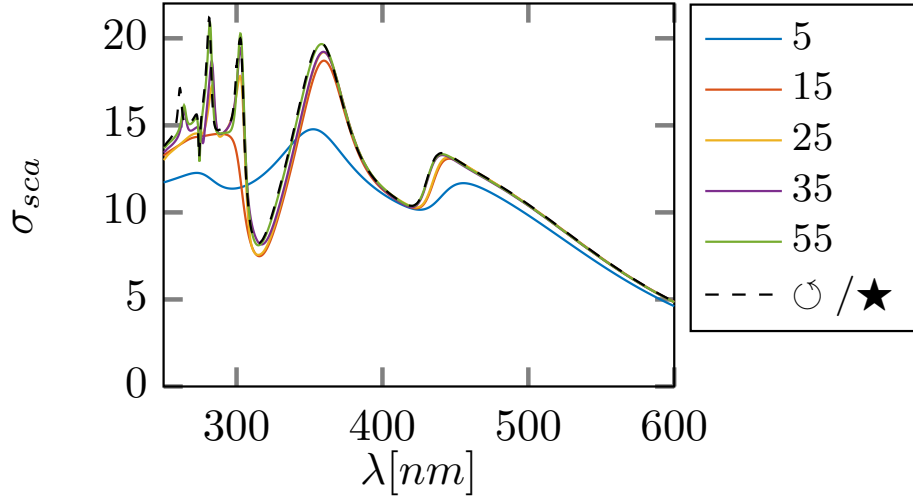


Figure 4.15 – Scattering efficiency σ_{sca} of dielectric rod with permittivity $\epsilon_R = 16$ and semi-axis $a = 100nm$, $b = 0.5a$, and $c = 0.25a$ evaluated with an increasing number of longitudinal and transverse static modes $N^{\parallel} = N^{\perp} = 5, 15, 25, 35, 55$. The rod is excited by a linearly polarized plane wave in the visible spectral range. The reference loop-star solution (black dashed line) is also shown for comparison (5988 degrees of freedom).

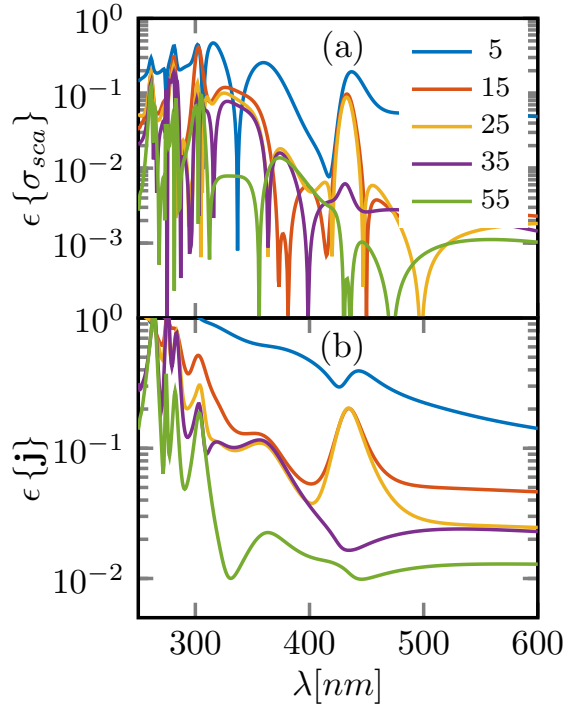


Figure 4.16 – Error ϵ in the evaluation of the scattering efficiency σ_{sca} and of the equivalent surface current density of a dielectric rod with permittivity $\epsilon_R = 16$ with semi-axis $a = 100nm$, $b = 0.5a$, and $c = 0.25a$ by using an increasing number of longitudinal and transverse static modes $N^{\parallel} = N^{\perp} = 5, 15, 25, 35, 55$. The solution evaluated by using loop/star basis function was assumed as a reference (5988 degrees of freedom).

16. In Fig. 4.15, we plot the σ_{sca} spectrum, obtained by increasing the truncation numbers $N^\perp = N^\parallel = 5, 15, 35, 55$. We use as reference the loop-star solution with 5984 degrees of freedom. If the wavelength is much larger than the dimension of the rod, the truncation numbers $N^\perp = N^\parallel$ equal to 15 are enough to correctly describe the scattering cross section. Nevertheless, the accuracy is lost as soon as the wavelength becomes comparable to the incident wavelength and high-frequency resonance peaks are not correctly described. Only by increasing the truncation number $N^\perp = N^\parallel$ to 55, all the resonance peaks, including the high-frequency ones, are correctly described. Figure 4.16 offers a more quantitative analysis of the errors (a) $\epsilon[\sigma_{sca}]$, (b) $\epsilon[\mathbf{j}]$. We note that while for large wavelength a truncation number $N^\perp = N^\parallel = 15$ is sufficient to have an error below $\epsilon[\sigma_{sca}] < 0.01$ and $\epsilon[\mathbf{j}] < 0.2$, if the wavelength becomes comparable to the rod largest dimension, as many as 55 basis function are needed to contain the error. Even in this case, the accuracy is deteriorated in the neighborhood of the resonance peaks. In conclusion, even if compared to the previously investigated scenarios, larger values of truncation numbers are needed to correctly describe the unknown current densities, the number of static modes needed to describe the solution still remains much smaller than the number of loop/star functions required to achieve a comparable accuracy.

4.5 Conclusions

We investigated the use of static modes to represent the unknowns and for the Galerkin projection of surface integral equations formulations of the electromagnetic scattering problem from penetrable objects. The static modes are composed by the union of *longitudinal* and *transverse* modes. Longitudinal modes are constituted by the irrotational eigenmodes of an electrostatic surface integral operator, which gives the scalar potential as a function of the surface charge density. Transverse modes are constituted by the solenoidal eigenmodes of a magnetostatic surface integral operator, which returns the vector potential as a function of the surface current distribution. These two sets are orthogonal. The static basis only depends on the shape of the object, thus, the same static basis can be used (and it brings the same advantages) regardless of the operating frequency and material of object. This fact enables the description of any scattering scenario involving one or more particle particles of a given shape, in terms of the same "alphabet" of basis function, regardless of the frequency of operation. Specifically, we demonstrate the effectiveness of this static basis for the Galerkin projection of the Poggio-Miller-Chang-Harrington-Wu-Tsai formulation of an electromagnetic scattering problem by a penetrable object. The choice

of static basis expansion regularizes the scattering operators, leading to an effective way to diagonalize the block-diagonal operators of the impedance matrix which are associated with the static Green function. We truncate the current density expansion to a finite number of static modes (called truncation number) by only considering the ones associated with the low-order eigenvalues. As a test case scenario, we considered the electromagnetic scattering from metal (plasmonic) objects and high permittivity dielectric objects, which exhibit resonances which are often challenging to model numerically. We monitor the accuracy of electric and magnetic equivalent surface currents densities and of the scattering efficiency as the truncation number is varied. We found that, in all the investigated cases, this method drastically reduces the number of unknowns compared to discretization in terms of sub-domain functions. The minimum truncation number required to obtain a prescribed level of accuracy does depend on the shape of the object, its material, and its characteristic dimension compared to the wavelength of operation. Our numerical experiments suggest that an accurate modeling of metal penetrable objects under plane wave excitation demands for fewer static modes than high-permittivity dielectric objects. This fact is due to the multitude of dielectric resonances that the high-permittivity objects exhibit as the frequency increases. As expected, far field observables, such as the scattering efficiency, are affected by smaller errors if compared to near field observables such as the equivalent electric and magnetic currents which are instead defined on the surface of the object. For all investigated scenarios, we also found a saturation of the error for large truncation numbers, because the addition of an additional longitudinal or transverse degrees mode to the expansion basis does not improve the quality of the solution. The results presented in this chapter may promote the use of the static basis in multiple scattering problems, including the numerical modeling of metasurfaces and metalens.

Chapter 5

Electromagnetic modes and resonances of two-dimensional objects

In this chapter, we investigate the electromagnetic modes and resonances of homogeneous, finite size, two-dimensional bodies in the frequency domain by a rigorous full wave approach based on an integro-differential formulation of the electromagnetic scattering problem. In particular, we introduce a modal expansion for the current density that disentangles the geometric and material properties of the body the integro-differential equation for the induced surface (free or polarization) current density field is solved. The current modes and the corresponding resonant values of the surface conductivity (eigenconductivities) are evaluated by solving a linear eigenvalue problem with a non-Hermitian operator. They are inherent properties of the body geometry and do not depend on the body material. The material only determines the coefficients of the modal expansion and hence the frequencies at which their amplitudes are maximum (resonance frequencies). The eigenconductivities and the current modes are studied in detail as the frequency, and the shape and the size of the body vary. Open and closed surfaces are considered. The presence of vortex current modes, in addition to the source-sink current modes (no whirling modes), which characterize plasmonic oscillations, is shown. Important topological features of the current modes, such as the number of sources and sinks, the number of vortices, and the direction of the vortices are preserved as the size of the body and the frequency vary. Unlike the source-sink current modes, in open surfaces the vortex current modes can be resonantly excited only in materials with a positive imaginary part of the surface conductivity. Eventually, as examples, the scattering by two-

dimensional bodies with either a positive or negative imaginary part of the surface conductivity is analyzed and the contributions of the different modes are examined.

In Section 5.3, the electromagnetic scattering problem is first formulated in the frequency domain by means of the integro-differential equation 5.4 governing the induced surface current density. Then, the general properties of the spectrum of the linear operator are examined and, at the end, the integro-differential equation is solved analytically by using the eigenfunctions (current modes) and eigenvalues (eigen-conductivities). Analytical expressions of the current modes and eigen-conductivities of an infinite plane are given.

In Sections 5.6 and 5.7, the current modes and the eigen-conductivities of circles, equilateral triangles, rectangles and spherical surfaces are analyzed in detail. The eigenfunctions and the eigenvalues of are evaluated numerically by applying a finite element method. In Section 5.8 eventually, the resonance behaviors of the scattering from 2D materials with either positive or negative imaginary part of the surface conductivity are examined. The solution (5.43) is validated by means of full wave numerical codes by comparing the scattering cross sections of a graphene disk and of a silicon disk.

5.1 Motivations

In the last ten years, two-dimensional materials have attracted a great amount of interest in the field of plasmonics and photonics (e.g., [108, 109, 110]). These materials constitute an attractive platform for the engineering of light-matter interactions across the visible, infrared, and terahertz spectral ranges, with new optical control beyond what can be done with bulk materials (e.g., [111, 112, 113, 114]). In terms of electrical properties, they range from the insulating hexagonal boron nitride and semiconducting transition metal dichalcogenides, to semi metallic graphene. They include multilayers, heterostructures and layered thin films whose thicknesses vary from one atomic layer to tens of nanometers. In general, when the thickness of the object is much smaller than the other two linear dimensions and than the wavelength of the electromagnetic field, only the in-plane electromagnetic response of the material is important and the electromagnetic scattering can be modeled by considering the object as two-dimensional (e.g., [115]). The understanding of the resonant electromagnetic behavior of a object is a fundamental prerequisite for the engineering of the electromagnetic field-matter interaction. In this chapter, we study the modes and the resonances in the electromagnetic scattering from two-dimensional (2D) objects by using the full Maxwell equations. Modes and resonances are determined by a rig-

orous full wave approach that naturally discriminates the role of the geometry, of the material, and of the incident electromagnetic field. This is a promising way to design separately the material, the geometry and the incident field for the desired object-electromagnetic field interaction. When the electromagnetic field is confined within a bounded domain (closed systems) the definition of resonant modes is straightforward. The mathematical model of such problems is characterized by self-adjoint Helmholtz operators leading to a countable infinite set of eigenfunctions, directly related to the resonances of the system. In contrast, when the electromagnetic field occupies the entire space (open systems) the definition of electromagnetic modes and resonance frequencies is more difficult. The electromagnetic scattering from finite size objects can be modeled in the frequency domain by means of full wave integral formulations in which the support of problem unknowns is bounded. These formulations, therefore, allow naturally surmounting the difficulties in the analysis of modes and resonances that arise when the spatial domain is unbounded. Different choices of the modes are possible. The quasi-normal modes (e.g., [116]) as well as the characteristic modes [18] are used to study open systems (e.g., [117], [118]). The quasi-normal modes are solution of an intrinsic nonlinear eigenvalue problem. They are not orthogonal in the usual sense; they depend on the material, shape and size of the scattering object. The characteristic modes have been recently evaluated for closed impedance surfaces [119]. They are real and satisfy a weighted orthogonality. The characteristic modes depend on frequency, the shape, size, and material composition of the scattering object. In this work the concept of material-independent mode [120, 121, 122] is applied for the first time to the study of the electromagnetic modes and resonances of an isotropic, homogeneous and not space dispersive 2D objects. The material-independent modes allow separating the role of geometry, material and incident electromagnetic field. This fact provides fundamental information on the resonant electromagnetic behaviors of 2D objects that other approaches hide. The surface (free or polarization) current density induced on the object surface is governed, in the frequency domain, by the full wave integro-differential equation (see 5.3 for more details)

$$\sigma^{-1}\mathbf{J}_s(\mathbf{r}_s) - \zeta_0\mathcal{L}\{\mathbf{J}_s\}(\mathbf{r}_s) = \mathbf{E}^{\parallel(0)}(\mathbf{r}_s) \text{ for any } \mathbf{r}_s \in S \quad (5.1)$$

where σ is the surface conductivity of the object, ζ_0 is the vacuum impedance, \mathcal{L} is the linear integro-differential operator that expresses the tangential component to of the induced electric field as function of the induced current density \mathbf{J}_s and $\mathbf{E}^{\parallel(0)}$ is the tangential component to S of the incident electric field. Equation (5.1) it is nothing but the constitutive relation of the material. It is very important to point out that the linear operator \mathcal{L} does not depend on the surface conductivity. The operator \mathcal{L}

is not Hermitian due to the retardation, hence its eigenfunctions are bi-orthogonal and the corresponding eigenvalues are complex (see Section 5.3 for more details). The eigenfunctions and the eigenvalues of \mathcal{L} only depend on the object geometry and the frequency. In this chapter, we analytically solve the equation (5.1) by using the eigenfunctions $\{\mathbf{J}_n\}$ and the eigenvalues $\{\sigma_n\}$ of the linear operator \mathcal{L} . The set of eigenfunctions $\{\mathbf{J}_n\}$ are used as basis to represent the surface current density. By exploiting the bi-orthogonality of the set $\{\mathbf{J}_n\}$ the solution of equation 5.1 is expressed as

$$\mathbf{J}_s(\mathbf{r}_s) = \sum_{n=1}^{\infty} \frac{\sigma_n}{\sigma_n - \zeta_0\sigma} \langle \mathbf{J}_n^*, \sigma \mathbf{E}^{\parallel(0)} \rangle \mathbf{J}_n(\mathbf{r}_s)$$

where $\langle \cdot, \cdot \rangle$ denotes the scalar product. This formula disentangles the geometric and material properties of the object and effectively predicts the resonant behavior of 2D objects as their shape, size and surface conductivity vary. The expansion coefficient of the n -th eigenfunction \mathbf{J}_n is proportional to $(\sigma_n - \zeta_0\sigma)$, hence the eigenvalue σ_n can be interpreted as the resonant value of the normalized surface conductivity for the mode \mathbf{J}_n . For these reasons $\{\sigma_n\}$ are called eigen-conductivities of the material independent current modes $\{\mathbf{J}_n\}$ of the 2D object. The real part of σ_n is always positive and it takes into account the radiation losses of the current mode, instead the imaginary part may be either positive or negative, depending on the mode and the linear dimension of the object normalized to the wavelength. The mode expansion, in the quasi-electrostatic limit, leads to the quasi-electrostatic modes described in [123], and in the weakly retarded limit to the corrections for the quasi-electrostatic modes proposed in [124, 125]. However, the approaches proposed in [94] can be only applied to objects whose linear dimensions are much smaller than the wavelength. Furthermore, these approaches disregard the presence of magnetic modes. Instead, the solution 5.1 can be applied for any value of the ratio between the linear dimensions of the object and the wavelength and properly takes into account the contribution of the magnetic modes. The presence of vortex current modes in addition to the no whirling modes that characterizes plasmonic oscillations in metals (called source-sink current modes in the chapter) is shown. These modes are disregarded in the approaches proposed in [123, 126, 127, 124, 125, 128]. The source-sink current modes, in the long wavelength limit, tend to the quasi-electrostatic modes, which characterize the plasmonic oscillations in metals. Instead, the vortex current modes, in the long wavelength limit, tend to the quasi-stationary magnetic modes, which cannot be described by the quasi-electrostatic approaches proposed in [123, 126, 127, 124, 125, 128]. Unlike the source-sink current modes, in open surfaces the vortex current

modes can be resonantly excited only in materials with positive imaginary part of the surface conductivity (i.e., dielectric materials). Cylindrical vector beams (e.g., [129]) can couple very efficiently with vortex current modes.

5.2 Electromagnetic scattering by two-dimensional objects

A thin object illuminated by a time harmonic electric field $\text{Re}[\mathbf{E}^{(0)}(\mathbf{r})e^{i\omega t}]$ is considered (\mathbf{r} is the position vector of a generic point of space with the origin at a given point). The object material is linear, isotropic, homogeneous and not space dispersive. The thickness of the object is smaller than its other two linear characteristic dimensions and than the wavelength of the electromagnetic field. In this limit only the in-plane electromagnetic response of the material is important and the object may be treated as it is two-dimensional (e.g., [115]). A 2D material may be characterized in the frequency domain either by the optical dielectric constant or, equivalently, by the optical surface conductivity

$$\sigma = i\omega (\varepsilon - \varepsilon_0) \Delta \quad (5.2)$$

In this chapter the surface conductivity is used. A simple analytical representation of the surface conductivity is

$$\sigma(\omega) = \frac{1}{\pi} \frac{S_f}{i\omega + \tau_f^{-1}} + \frac{1}{\pi} \frac{S_b}{i(\omega - \omega_b^2/\omega) + \tau_b^{-1}} \quad (5.3)$$

where the first (Drude) and second (Lorentz) terms represent, respectively, the contribution of the free and bound (polarization) charges. The surface conductivity of different 2D materials can be modeled with a suitable choice of the parameters: the weights and , the exciton/phonon frequency and the phenomenological relaxation times and (see in references [112] and [113]). The sign of the imaginary part of the surface conductivity depends on the material and on the frequency, while the real part is always positive for passive materials. For conducting materials the imaginary part of is always negative in the frequency ranges where the effects of interband transitions are negligible. For dielectric materials, the imaginary part of may be either positive or negative depending on the frequency. For examples, in suspended high doped (gated) single layer graphene (with chemical potentials of the order of hundred of eV) it results in the far and mid infrared ranges where (e.g., [130]), while in single layer transition metal dichalcogenides it results in the near infrared range (e.g.,

[130, 131]).

5.3 Mathematical model

The surface of the 2D object is denoted by S , \mathbf{r}_s is the position vector of a generic point of S and \mathbf{n} is the normal. The electromagnetic scattering by the 2D object is modeled by the following integro-differential equation for the induced surface current density:

$$\sigma^{-1}\mathbf{J}_s - \zeta_0\mathcal{L}\{\mathbf{J}_s\}(\mathbf{r}_s) = \mathbf{E}^{\parallel(0)}(\mathbf{r}_s) \quad \text{for any } \mathbf{r}_s \in S \quad (5.4)$$

The constitutive relation of the 2D material is

$$\mathbf{J}_s = \sigma\mathbf{T}\{\mathbf{E}\} \quad (5.5)$$

where \mathbf{J}_s is the induced surface current density, $\mathbf{T}\{\cdot\} = -\mathbf{n} \times [\mathbf{n} \times \{\cdot\}]$ is the projector that extracts the tangential component, σ is the surface conductivity of the object. On S , a surface charge arises whose density amplitude ρ_s is given by continuity equation

$$\nabla_s \cdot \mathbf{J}_s = -i\omega\rho_s \rightarrow \rho_s = -\frac{1}{i\omega}\nabla_s \cdot \mathbf{J}_s \quad (5.6)$$

The total electric field $\mathbf{E}(\mathbf{r})$ is expressed as

$$\mathbf{E}(\mathbf{r}) = \mathbf{E}^{(0)}(\mathbf{r}) + \mathbf{E}^{(S)}(\mathbf{r}) \quad (5.7)$$

where $\mathbf{E}^{(0)}$ and $\mathbf{E}^{(S)}$ are the amplitude of the incident electric field and scattered electric field respectively. On the other hand, the scattered fields can be expressed in terms of \mathbf{J}_s and ρ_s by the electromagnetic potentials in the Lorenz gauge, as seen in sec. 2.2

$$\begin{aligned} \mathbf{E}^{(S)}(\mathbf{r}) &= -\nabla\Phi^e(\mathbf{r}) - j\omega\mathbf{A}^e(\mathbf{r}) \\ &= -\frac{1}{\varepsilon_0}\nabla\int_S g(\mathbf{r},\mathbf{r}')\rho_s(\mathbf{r}')dS' - i\omega\mu_0\int_S g(\mathbf{r},\mathbf{r}')\mathbf{J}_s(\mathbf{r}')dS' \\ &= -\frac{1}{\varepsilon_0}\nabla\mathcal{G}\{\rho_s\}(\mathbf{r}) - i\omega\mu_0\mathcal{G}\{\mathbf{J}_s\}(\mathbf{r}) \\ \mathbf{H}^{(S)}(\mathbf{r}) &= +\frac{1}{\mu}\nabla\times\mathbf{A}^e(\mathbf{r}) \\ &= \nabla\times\int_S g(\mathbf{r},\mathbf{r}')\mathbf{J}_s(\mathbf{r}')dS' \\ &= \nabla\times\mathcal{G}\{\mathbf{J}_s\}(\mathbf{r}) \end{aligned} \quad (5.8)$$

where $\mathcal{G}\{\mathbf{f}\}$ is the integral operator

$$\mathcal{G}\{\mathbf{f}\}(\mathbf{r}) = \int_S g(\mathbf{r}, \mathbf{r}') \mathbf{f}(\mathbf{r}') dS'. \quad (5.9)$$

By combining the constitutive relation and the potential expression, the integro-differential equation that governs the induced surface current density field is obtained.

$$\begin{aligned} \mathbf{J}_s &= \sigma \mathbf{T}\{\mathbf{E}\} \\ &= \sigma \mathbf{T}\left\{-\frac{1}{\varepsilon_0} \nabla \mathcal{G}\left\{-\frac{1}{i\omega} \nabla_s \cdot \mathbf{J}_s\right\} - i\omega \mu_0 \mathcal{G}\{\mathbf{J}_s\}\right\} \\ &= \sigma \mathbf{T}\left\{\frac{1}{i\omega \varepsilon_0} \nabla \mathcal{G}\{\nabla_s \cdot \mathbf{J}_s\} - i\omega \mu_0 \mathcal{G}\{\mathbf{J}_s\}\right\} \\ &= \sigma \mathcal{L}\{\mathbf{J}_s\} \end{aligned} \quad (5.10)$$

where $\mathcal{L}\{\mathbf{f}\}$ is the integral operator

$$\mathcal{L}\{\mathbf{f}\}(\mathbf{r}) = \mathbf{T}\left\{\frac{1}{i\omega \varepsilon_0} \nabla \mathcal{G}\{\nabla_s \cdot \mathbf{f}\}(\mathbf{r}) - i\omega \mu_0 \mathcal{G}\{\mathbf{f}\}(\mathbf{r})\right\}. \quad (5.11)$$

The equation is solved with the boundary condition

$$\mathbf{J}_s \cdot \mathbf{m}\big|_{\partial\Sigma} = 0 \quad (5.12)$$

Once the induced current density has been evaluated by solving equation with the boundary condition, the expression 5.8 allows to evaluate the scattered electromagnetic field everywhere.

5.4 Auxiliary eigenvalue problem

The integro-differential equation can be reduced to an algebraic form by using, as basis functions for representing the surface current density, the eigenfunctions of \mathcal{L} that satisfy the boundary conditions. Therefore, the linear eigenvalue problem

$$\begin{cases} \mathcal{L}\{\mathbf{J}_n\} = \frac{1}{\sigma_n} \mathbf{J}_n \\ \mathbf{J}_n \cdot \mathbf{m}\big|_{\partial\Sigma} = 0 \end{cases} \quad (5.13)$$

is introduced, where σ_n is the "eigenvalue" associated to the eigenfunction \mathbf{J}_n and $n = 1, 2, \dots$. The eigenvalues $\{\sigma_n\}$ and eigenfunctions $\{\mathbf{J}_n\}$ are dimensionless quantities. In particular, for a given surface S, they only depend on its characteristic linear

dimension l_c , i.e., the radius of the smallest sphere enclosing the surface Σ , and on the wavenumber k through the normalized size of the object $kl_c = 2\pi\left(\frac{l_c}{\lambda}\right)$ (λ is the vacuum wavelength).

5.4.1 Properties

The eigenvalues and the eigenfunctions of the operator \mathcal{L} are characterized by the following properties

1. The eigenvalue σ_n is related to the electromagnetic field $(\mathcal{E}_n, \mathcal{H}_n)$. Indeed, it results that

$$\frac{\text{Re}\{\sigma_n\}}{|\sigma_n|^2} = -\frac{2S_n}{\langle \mathbf{J}_n, \mathbf{J}_n \rangle} \leq 0 \quad (5.14)$$

$$\frac{\text{Im}\{\sigma_n\}}{|\sigma_n|^2} = \frac{4\omega}{\langle \mathbf{J}_n, \mathbf{J}_n \rangle} (W_n^{(mag)} - W_n^{(ele)}) \quad (5.15)$$

where $W_n^{(mag)}$ and $W_n^{(ele)}$ are, respectively, the averaged magnetic and electric energies associated to $(\mathcal{E}_n, \mathcal{H}_n)$

$$W_n^{(mag)} = \frac{\mu_0}{4} \int_V |\mathcal{H}_n|^2 dV \quad (5.16)$$

$$W_n^{(ele)} = \frac{\varepsilon_0}{4} \int_V |\mathcal{E}_n|^2 dV \quad (5.17)$$

and S_n is the averaged power radiated toward the infinite

$$S_n = \frac{1}{2\zeta_0} \int_S |\mathcal{E}_n|^2 dS < 0 \quad (5.18)$$

The electric \mathcal{E}_n and magnetic field \mathcal{H}_n can be evaluated by the expression 5.8. Since S_n , $W_n^{(mag)}$ and $W_n^{(ele)}$ are positive quantities, it results $\text{Re}\{\sigma_n\} \leq 0$ while $\text{Im}\{\sigma_n\} \leq 0$ has not a definite sign.

2. In the long wavelength limit ($kl_c \rightarrow 0$), for the non-solenoidal eigenfunctions ($\nabla_S \cdot \mathbf{J}_n \neq 0$) it results

$$\mathcal{L}\{\mathbf{J}_s\} = \mathcal{E}^0\{\mathbf{J}_s\} = \frac{1}{ik} \mathbb{T}\{\nabla \mathcal{V}\{\nabla_s \cdot \mathbf{J}_s\}(\mathbf{r})\} \quad (5.19)$$

where

$$\mathcal{V}\{\mathbf{f}\}(\mathbf{r}) = \int_S g_0(\mathbf{r}, \mathbf{r}') \mathbf{f}(\mathbf{r}') dS'. \quad (5.20)$$

The linear operator \mathcal{E}^0 is skew-Hermitian. This is the electro-quasi static limit in which the eigenfunctions of \mathcal{L} are both non-solenoidal and irrotational and

the corresponding eigenvalues are purely imaginary with negative imaginary part. The electro-quasi static limit characterizes the plasmon oscillations in conducting materials.

3. In the long wavelength limit ($kl_c \rightarrow 0$), for the solenoidal eigenfunctions ($\nabla_S \cdot \mathbf{J}_n = 0$) it results

$$\mathcal{L}\{\mathbf{J}_s\} = \mathcal{H}^0\{\mathbf{J}_s\} = -ik\mathcal{V}\{\mathbf{J}_s\} \quad (5.21)$$

where

$$\mathcal{V}\{\mathbf{f}\}(\mathbf{r}) = \int_S g_0(\mathbf{r}, \mathbf{r}')\mathbf{f}(\mathbf{r}')dS'. \quad (5.22)$$

The linear operator \mathcal{H}^0 is skew-Hermitian. This is the magneto-quasi static limit in which the eigenfunctions of \mathcal{L} are both solenoidal and rotational.

4. Let us now consider an infinite plane surface S: in this limit, the spectrum of \mathcal{L} becomes continuous and its eigenvalues and eigenfunctions can be evaluated analytically by using the 2D Fourier transform and the convolution theorem. The eigenfunctions are

$$\mathbf{J}_q(\mathbf{r}_s) = \mathbf{U}_q \exp(-i\mathbf{q} \cdot \mathbf{r}_s) \quad \text{for any } \mathbf{q} \in \mathcal{R}^2 \quad (5.23)$$

where \mathbf{U}_q is the solution of the equation

$$\frac{1}{ik}[(k^2 - \mathbf{q}\mathbf{q})\tilde{g}(\mathbf{q}, k)]\mathbf{U}_q = \frac{1}{\sigma_q}\mathbf{U}_q \quad (5.24)$$

and

$$\tilde{g}(\mathbf{q}, k) = \frac{1}{2\sqrt{q^2 - k^2}} \quad (5.25)$$

is the 2D Fourier transform of $g(\mathbf{r}_s)$.

- For $q \geq k$: the function \tilde{g} is real and it describes evanescent waves in the orthogonal direction to the surface S with decay length

$$\frac{1}{\sqrt{q^2 - k^2}} \quad (5.26)$$

- For $q \leq k$: the function \tilde{g} is imaginary, with negative imaginary part. It describes waves radiated toward infinite with wavenumber

$$\sqrt{k^2 - q^2} \quad (5.27)$$

The vector \mathbf{U}_q is decomposed as the sum of \mathbf{U}_q^{\parallel} (parallel to \mathbf{q}) and \mathbf{U}_q^{\perp} (orthog-

onal to \mathbf{q}). Both \mathbf{U}_q^\parallel and \mathbf{U}_q^\perp are solution of eigenvalue equation (5.24). The eigenvalues are respectively

$$\sigma_q^\parallel = -\frac{2ik}{\sqrt{q^2 - k^2}} \quad (5.28)$$

$$\sigma_q^\perp = -\frac{2\sqrt{q^2 - k^2}}{ik} \quad (5.29)$$

The eigenfunctions \mathbf{J}_q^\parallel are curl free, while the eigenfunctions \mathbf{J}_q^\perp are divergence free. In the long wavelength limit $\frac{k}{q} \rightarrow 0$, $\sigma_q^\parallel = -i\left(\frac{2k}{q}\right)$ and $\sigma_q^\perp = i\left(\frac{2q}{k}\right)$. In the short wavelength limit $\frac{k}{q} \rightarrow \infty$, instead, $\sigma_q^\parallel = \sigma_q^\perp = -2$

The physical and mathematical meaning of eigenvalues and eigenfunctions of \mathcal{L} is the following. The operator $\zeta_0\mathcal{L}$ expresses the tangential component of the scattered electric field to S in terms of the induced surface current density. Consequently, the eigenfunction \mathbf{J}_n is the distribution of the surface current density that coincides with the tangential component to the surface S of the electric field it generates, apart from the multiplicative factor $\frac{1}{\sigma_n}$.

5.4.2 Frequency picture and material picture

By exploiting the bi-orthogonality of the set $\{\mathbf{J}_n\}$, the surface current density is given by expression

$$\mathbf{J}_s(\mathbf{r}_s) = \sum_{n=1}^{\infty} \frac{\sigma_n}{\sigma_n - \zeta_0\sigma} \langle \mathbf{J}_n^*, \sigma \mathbf{E}^{\parallel(0)} \rangle \mathbf{J}_n(\mathbf{r}_s) \quad (5.30)$$

This formula disentangles the geometric and material properties of the object and effectively predicts the resonant behavior of 2D objects as their shape, size and surface conductivity vary. The expansion coefficient of the n-th eigenfunction \mathbf{J}_n is proportional to

$$\frac{1}{\sigma_n - \zeta_0\sigma} \quad (5.31)$$

so the eigenvalue σ_n can be interpreted as the resonant value of the normalized surface conductivity for the mode \mathbf{J}_n . For assigned geometry and surface conductivity $\sigma(\omega)$ it is clear that if $\langle \mathbf{J}_n^*, \mathbf{E}^{\parallel(0)} \rangle \neq 0$, the amplitude of the current mode \mathbf{J}_n increases as $\zeta_0\sigma$ approaches σ_n . In this view, denoted as "frequency picture", the resonance frequency is the value of the frequency for which

$$\left| \sigma_n \left(\omega \frac{l_c}{c_0} \right) - \zeta_0\sigma(\omega) \right| = \min_{\omega} \quad (5.32)$$

This picture requires that both $\langle \mathbf{J}_n^*, \mathbf{E}^{\parallel(0)} \rangle \neq 0$ and \mathbf{J}_n vary very slowly on the frequency in the neighbors of the resonance frequencies. It is possible to introduce a complementary view, denoted as "material picture", where the geometry and the operating frequency are assigned and $\Gamma = \zeta_0 \sigma$ is considered as an independent parameter. In this case, the resonant conductivities are defined as the values of Γ for which

$$\left| \sigma_n \left(\omega \frac{l_c}{c_0} \right) - \Gamma \right| = \min_{\Gamma} \quad (5.33)$$

The material picture is particularly relevant because the conductivity of some 2D materials can be tuned chemically, electrostatically and by applying a magnetic field.

5.5 Results and discussion

The electromagnetic field scattered by an object depends on its shape, size, and material, as well as, on the incident electromagnetic field. The shape and the normalized size of the object determine the current modes and the corresponding eigen-conductivities. The material of the object determines the amplitudes of the current modes for a given incident field, according to equation 5.43. Clearly, the conditions for the mode to be resonantly excited are that the frequency satisfies "frequency picture". In this Section, the current modes and the corresponding eigen-conductivities of some canonical surfaces either open (circles, triangles, rectangles) or closed (spherical surfaces) are analyzed in detail. They are applied to the study of the resonances in the electromagnetic scattering from 2D materials with either positive or negative imaginary part of the surface conductivity and the contributions of the different current modes are examined. Due to some different behaviors the work distinguishes between open and closed surfaces. In the long wavelength limit $kl_c \rightarrow 0$, the eigen-conductivities are purely imaginary and the current modes split in two subsets

- the current modes that are at the same time non-solenoidal and irrotational, whose eigen-conductivities have negative imaginary part. They are characterized by sources and sinks.
- the current modes that are at the same time solenoidal and rotational, whose eigen-conductivities have positive imaginary part. They are characterized by loops that are transformed into vortices due to the retardation effects.

For these reasons, in the work the following classification is adopted: the current modes that in the long wavelength limit tend to non-solenoidal and irrotational fields

are called source-sink current modes and the current modes that in the long wavelength limit tend to solenoidal and rotational fields are called vortex current modes. In the first case, each source-sink current mode preserves the number of sources and sinks as the normalized size of the object varies. In the second one, each vortex current mode preserves the number of vortices together with their directions. The eigen-conductivities and the current modes have been evaluated by applying the Galerkin method and the Rao-Wilton-Glisson (RWG) functions have been used as basis functions to represent the surface current density. This choice guarantees the continuity of the normal component of the surface current density to any edge of the finite element mesh.

5.5.1 Source-sink current modes

The imaginary part of the eigen-conductivities of the source-sink current modes is always negative in the long wavelength limit. In this limit the source-sink current modes accounts for the plasmonic oscillations in 2D conducting materials. The eigen-conductivities of the source-sink current modes and the mode themselves are labeled in such a way that in the long wavelength limit it results

$$\text{Im}\{\sigma_1\} < \text{Im}\{\sigma_2\} < \text{Im}\{\sigma_3\} < \dots < 0 \quad (5.34)$$

5.5.2 Vortex current modes

The imaginary part of the eigen-conductivities of the vortex current modes is always positive in the long wavelength limit. Therefore, the eigen-conductivities of the vortex current modes and the mode themselves are labeled in such a way that in the long wavelength limit it results

$$0 < \text{Im}\{\sigma_1\} < \text{Im}\{\sigma_2\} < \text{Im}\{\sigma_3\} < \dots \quad (5.35)$$

5.6 Current modes and eigen-conductivities of open surfaces

The source-sink current modes and the corresponding eigen-conductivities of the circle and of the equilateral triangle are first analyzed. The radius of the circle and the length of the side of the triangle are indicated with the same symbol l .

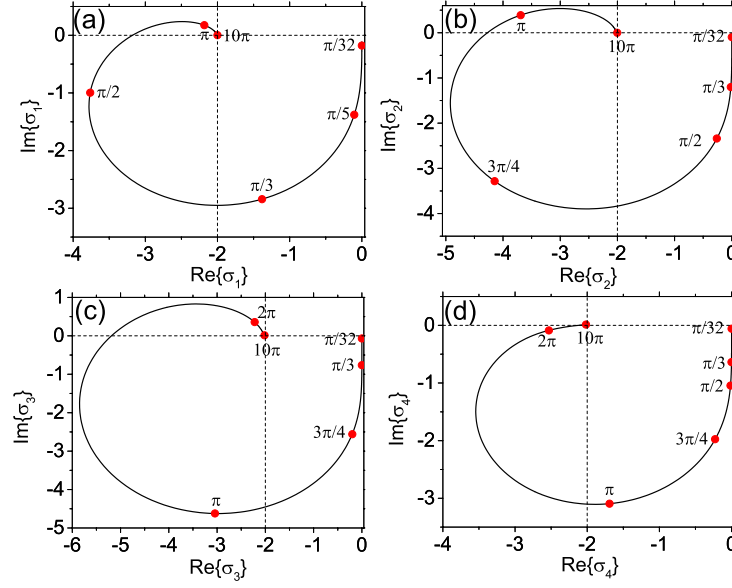


Figure 5.1 – Loci of the eigen-conductivities σ_1 (a), σ_2 (b), σ_3 (c) and σ_4 (d) of the first four source-sink current modes of the circle spanned on the complex plane as function of $x = 2\pi(l/\lambda)$; here l is the circle radius and λ is the wavelength in vacuum.

5.6.1 Circle

Source-sink current modes

Figures 5.1 show the behavior of the first four eigen-conductivities of the circle as function of the size parameter x : the graphs are the loci that each eigen-conductivity spans in the complex plane as x varies. The loci of the eigen-conductivities are open spirals that start at the point $(0,0)$ of the complex plane for $x = 0$ and move to the third quarter as x increases according to the general properties: both the real and the imaginary parts of the eigen-conductivities become negative and decrease. At certain values of x , depending on the specific current mode, the imaginary part of the eigen-conductivity starts to increase and later it changes its sign. The loci cross the real axis, go into the second quarter and end up at the point $(-2,0)$ of the complex plane. As for the infinite plane previously discussed, the real part of the eigen-conductivities approaches -2 for $x \rightarrow \infty$ and the imaginary part tend to zero but from the positive side. Figures 5.2, 5.3 and 5.4 show respectively the real part of the source-sink current modes 1&1', 2&2', 3&3' and 4 of the circle at $l/\lambda = 10^{-2}$, $l/\lambda = 1$ and $l/\lambda = 5$. The current modes on the same columns have the same eigen-conductivities, thus they are degenerate. For the circle at $l/\lambda = 10^{-2}$ in Figure 5.2, the source-sink current modes 1&1' have a strong dipolar character, the modes 2&2' have a quadrupolar character while the modes 3&3' have a sextupolar character. The

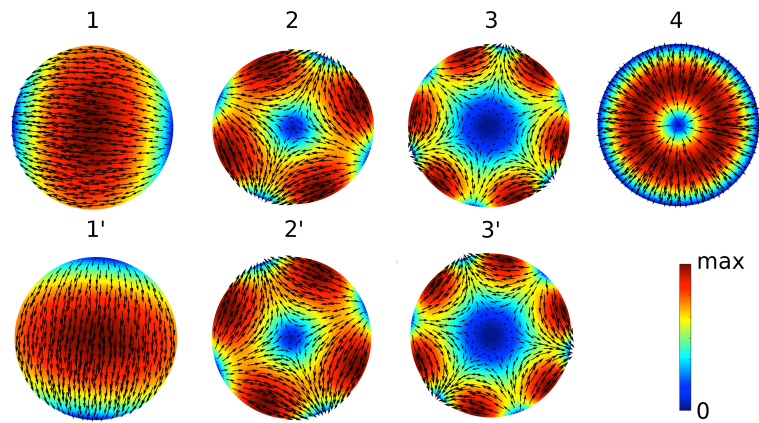


Figure 5.2 – Real part of the first four source-sink current modes of a circle at $l/\lambda = 10^{-2}$; here l is the circle radius and λ the wavelength in vacuum. The vectors are directed along $\text{Re}\{\mathbf{J}_n\}$ and the colors represent the intensity of $|\text{Re}\{\mathbf{J}_n\}|$

presence of degenerate modes is due to circular symmetry. The field lines of the mode 4 are radial. It is observed that as the l/λ ratio increases, the number of sources and sinks are conserved and the field patterns are nearly preserved (Figures 5.2-5.4).

Vortex current modes

Figure 5.5 show the behaviour of the eigen-conductivities of the first four vortex current modes for the circle as function of $x = 2\pi(l/\lambda)$. Unlike the loci of the eigen-conductivities of the source-sink current modes, these loci are always located in the second quarter of the complex plane, so the imaginary part is always positive and the real part is always negative. As x increases, both the real and imaginary parts decrease. More specifically, the loci of the eigen-conductivities of the vortex current modes start from the point $(0, +\infty)$ of the complex plane for $x = 0$, stay in the second quarter as x increases and end up into the point $(-2, 0)$ for $x \rightarrow 0$. Figures 5.6, 5.7 and 5.8 show respectively the real part of the vortex current modes 1, 2&2', 3 and 4 &4' of the circle at $l/\lambda = 10^{-2}$, $l/\lambda = 1$ and $l/\lambda = 5$. The current modes on the same columns have the same eigen-conductivities, thus they are degenerate. This is due to circular symmetry. For the circle at $l/\lambda = 10^{-2}$, the vortex current mode 1 has a strong magnetic dipolar character. Its magnetic dipole moment is oriented orthogonally to the surface. The vortex current modes 2&2' are composed of two identical sets of current vortices with antiparallel magnetic dipole moments. Instead, the vortex current modes 3&3' are composed of four identical sets of current vortices with alternating magnetic dipole moments. Lastly, the current mode 4 consists of concentric current vortices where the direction of current changes at a

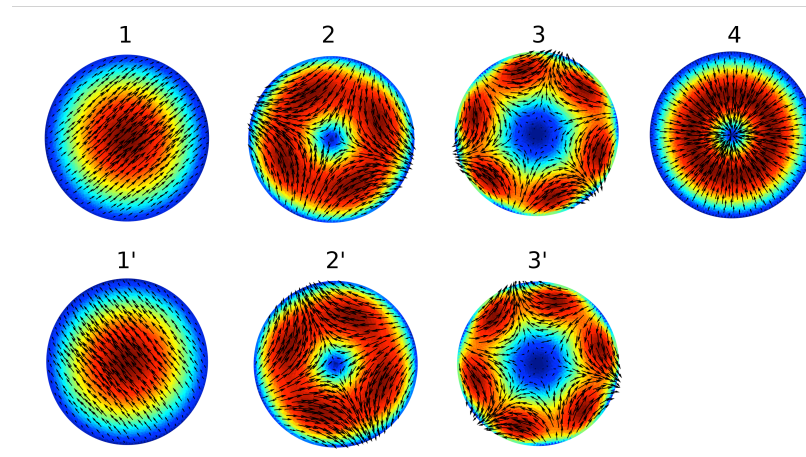


Figure 5.3 – Real part of the first four source-sink current modes of a circle at $l/\lambda = 1$; here l is the circle radius and λ the wavelength in vacuum. The vectors are directed along $\text{Re}\{\mathbf{J}_n\}$ and the colors represent the intensity of $|\text{Re}\{\mathbf{J}_n\}|$

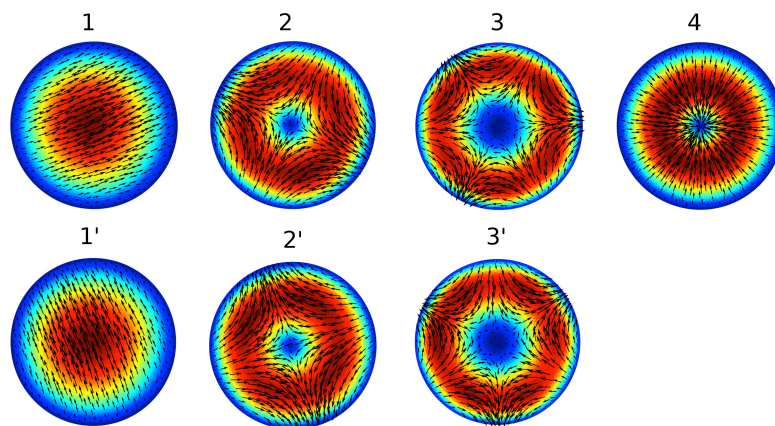


Figure 5.4 – Real part of the first four source-sink current modes of a circle at $l/\lambda = 5$; here l is the circle radius and λ the wavelength in vacuum. The vectors are directed along $\text{Re}\{\mathbf{J}_n\}$ and the colors represent the intensity of $|\text{Re}\{\mathbf{J}_n\}|$

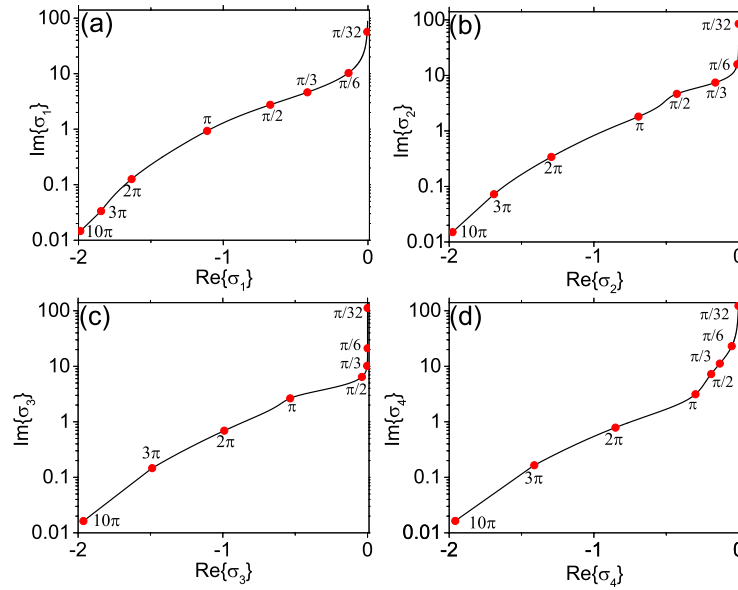


Figure 5.5 – Loci of the eigen-conductivities σ_1 (a), σ_2 (b), σ_3 (c) and σ_4 (d) of the first four vortex current modes of the circle spanned on the complex plane as function of $x = 2\pi(l/\lambda)$; here l is the circle radius and λ is the wavelength in vacuum.

certain radius. The number of vortices is conserved as l/λ increases and the mode patterns are substantially preserved.

5.6.2 Equilateral triangle

Source-sink current modes

Figures 5.9 show the behavior of the first four eigen-conductivities of the triangle as function of the size parameter x : the graphs are the loci that each eigen-conductivity spans in the complex plane as x varies. The loci of the eigen-conductivities are open spirals that start at the point $(0,0)$ of the complex plane for $x = 0$ and move to the third quarter as x increases according to the general properties: both the real and the imaginary parts of the eigen-conductivities become negative and decrease. At certain values of x , depending on the specific current mode, the imaginary part of the eigen-conductivity starts to increase and later it changes its sign. The loci cross the real axis, go into the second quarter and end up at the point $(-2,0)$ of the complex plane. As for the infinite plane previously discussed, the real part of the eigen-conductivities approaches -2 for $x \rightarrow \infty$ and the imaginary part tend to zero but from the positive side. Figures 5.10, 5.11 and 5.12 show respectively the real part of the source-sink current modes 1&1', 2, 3&3' and 4 &4' of the triangle at $l/\lambda = 10^{-2}$,

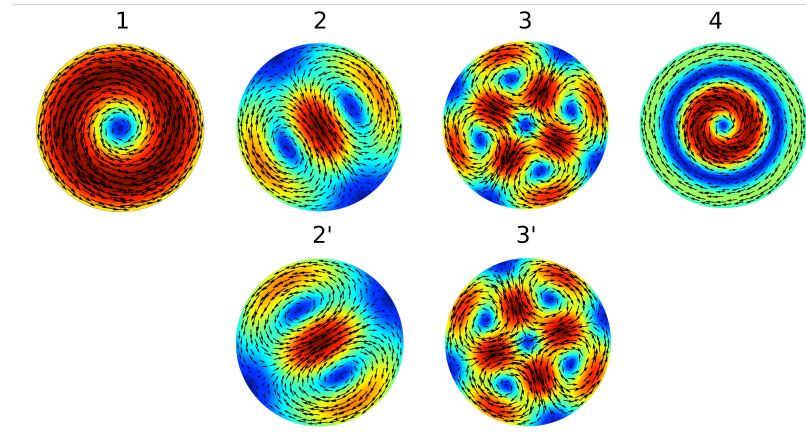


Figure 5.6 – Real part of the first four vortex current modes of a circle at $l/\lambda = 10^{-2}$; here l is the circle radius and λ the wavelength in vacuum. The vectors are directed along $\text{Re}\{\mathbf{J}_n\}$ and the colors represent the intensity of $|\text{Re}\{\mathbf{J}_n\}|$

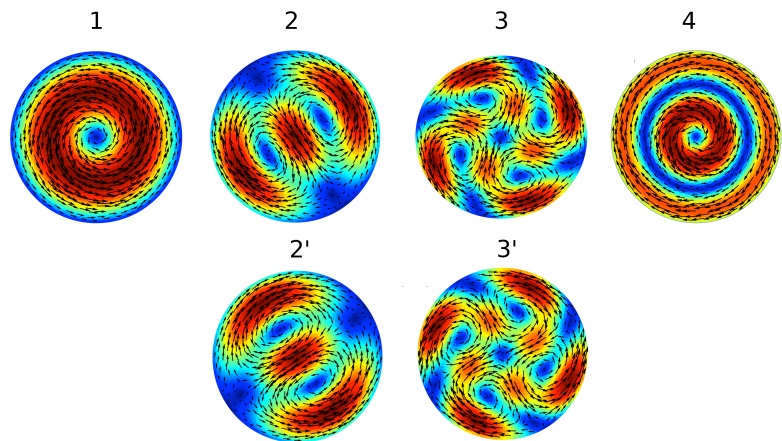


Figure 5.7 – Real part of the first four vortex current modes of a circle at $l/\lambda = 1$; here l is the circle radius and λ the wavelength in vacuum. The vectors are directed along $\text{Re}\{\mathbf{J}_n\}$ and the colors represent the intensity of $|\text{Re}\{\mathbf{J}_n\}|$

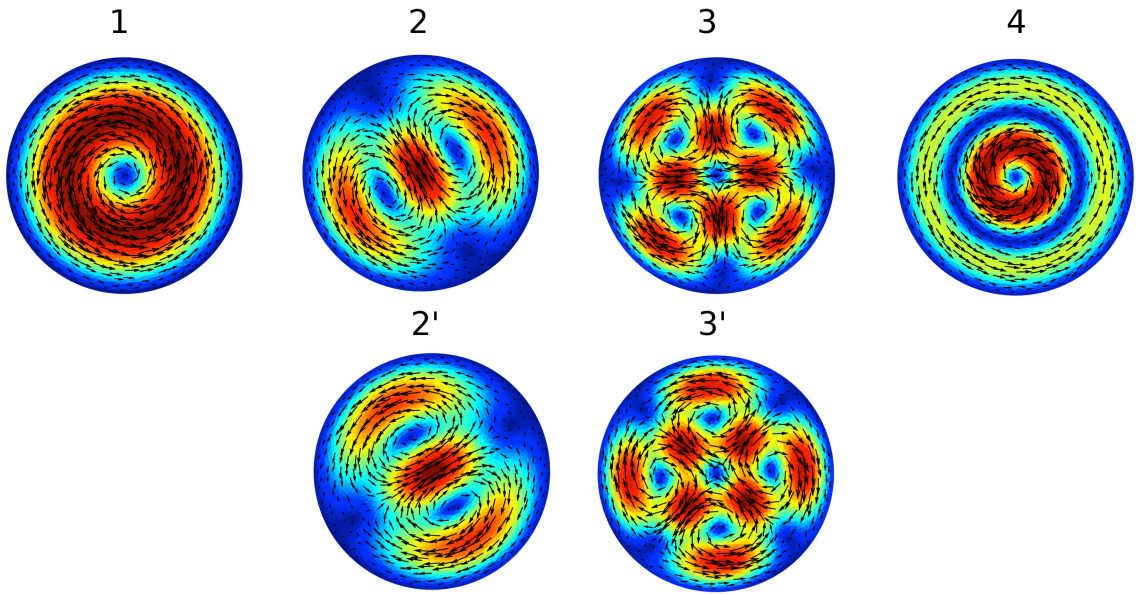


Figure 5.8 – Real part of the first four vortex current modes of a circle at $l/\lambda = 5$; here l is the circle radius and λ the wavelength in vacuum. The vectors are directed along $\text{Re}\{\mathbf{J}_n\}$ and the colors represent the intensity of $|\text{Re}\{\mathbf{J}_n\}|$

$l/\lambda = 1$ and $l/\lambda = 5$. The current modes on the same columns have the same eigen-conductivities, thus they are degenerate. For the triangle at $l/\lambda = 10^{-2}$ in Figure 5.10, the source-sink current modes 1&1' have a strong electric dipolar character and the mode 2 has a tripolar character. The current modes 3&3' and 4&4' have a strong dipolar component, too. The modes 1&1', 3&3' and 4&4' are degenerate because of symmetry of the equilateral triangle. As in the previous case, the number of sources and sinks are conserved as l/λ increases. But the field patterns change: the sources and the sinks that in the long wavelength limit are located in correspondence of the corners and edges of the triangle penetrate into it as l/λ increases.

Vortex current modes

Figure 5.13 show the behaviour of the eigen-conductivities of the first four vortex current modes for the triangle as function of $x = 2\pi(l/\lambda)$. The conclusions are absolutely similar to what we have seen in the case of vortex current modes for circle: the loci are always located in the second quarter of the complex plane, so the imaginary part is always positive and the real part is always negative. As x increases, both the real and imaginary parts decrease. More specifically, the loci of the eigen-conductivities of the vortex current modes start from the point $(0, +\infty)$ of the complex plane for $x = 0$, stay in the second quarter as x increases and end up into the point $(-2, 0)$ for $x \rightarrow \infty$. Figures 5.14, 5.15 and 5.16 show respectively

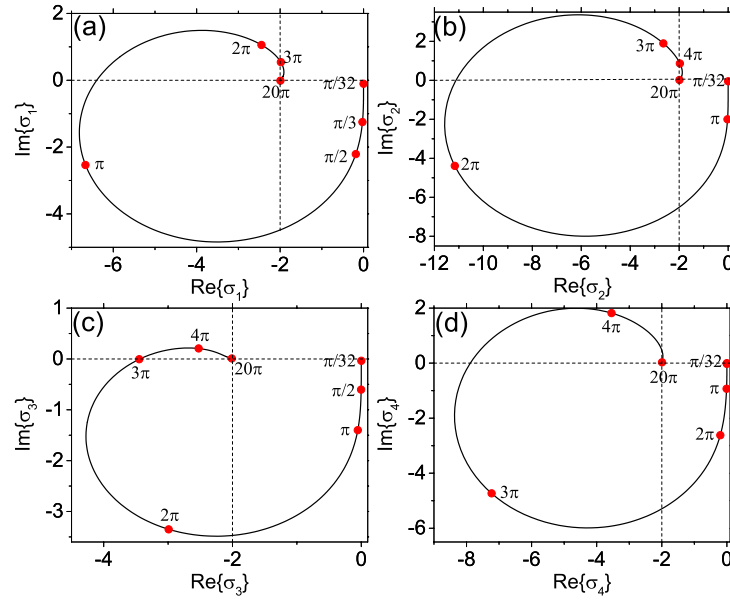


Figure 5.9 – Loci of the eigen-conductivities σ_1 (a), σ_2 (b), σ_3 (c) and σ_4 (d) of the first four source-sink current modes of the triangle spanned on the complex plane as function of $x = 2\pi(l/\lambda)$; here l is the length of the triangle and λ is the wavelength in vacuum.

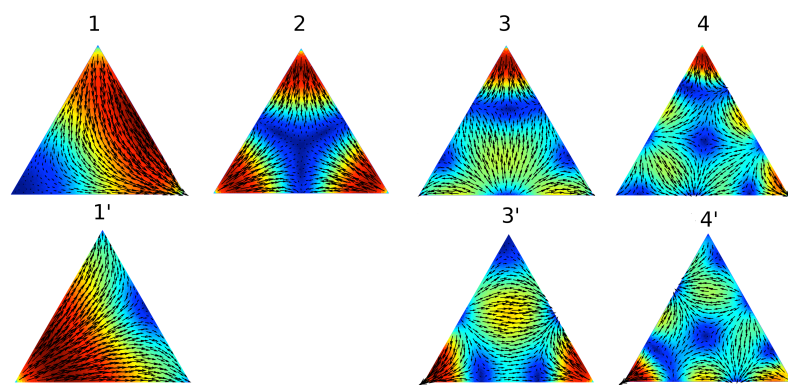


Figure 5.10 – Real part of the first four source-sink current modes of a triangle at $l/\lambda = 10^{-2}$; here l is the triangle side and λ the wavelength in vacuum. The vectors are directed along $\text{Re}\{\mathbf{J}_n\}$ and the colors represent the intensity of $|\text{Re}\{\mathbf{J}_n\}|$

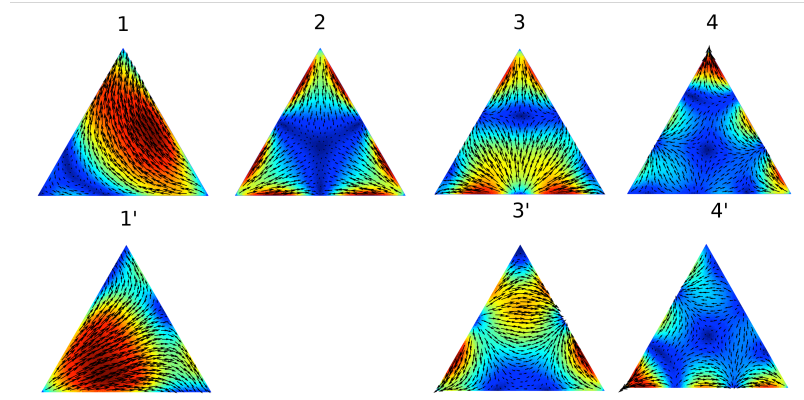


Figure 5.11 – Real part of the first four source-sink current modes of a triangle at $l/\lambda = 1$; here l is the triangle side and λ the wavelength in vacuum. The vectors are directed along $\text{Re}\{\mathbf{J}_n\}$ and the colors represent the intensity of $|\text{Re}\{\mathbf{J}_n\}|$

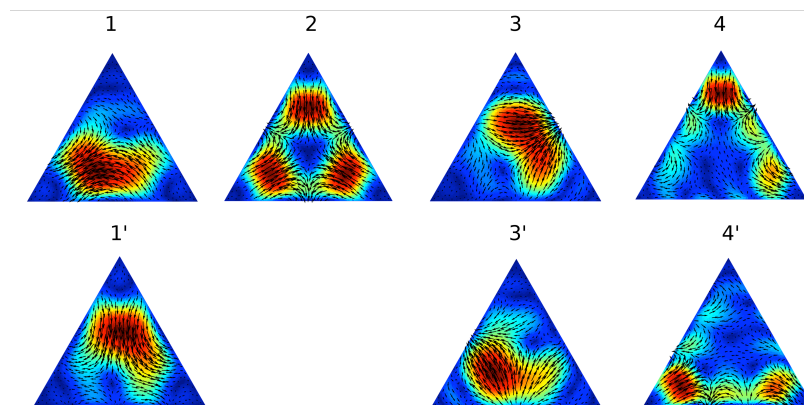


Figure 5.12 – Real part of the first four source-sink current modes of a triangle at $l/\lambda = 5$; here l is the triangle side and λ the wavelength in vacuum. The vectors are directed along $\text{Re}\{\mathbf{J}_n\}$ and the colors represent the intensity of $|\text{Re}\{\mathbf{J}_n\}|$

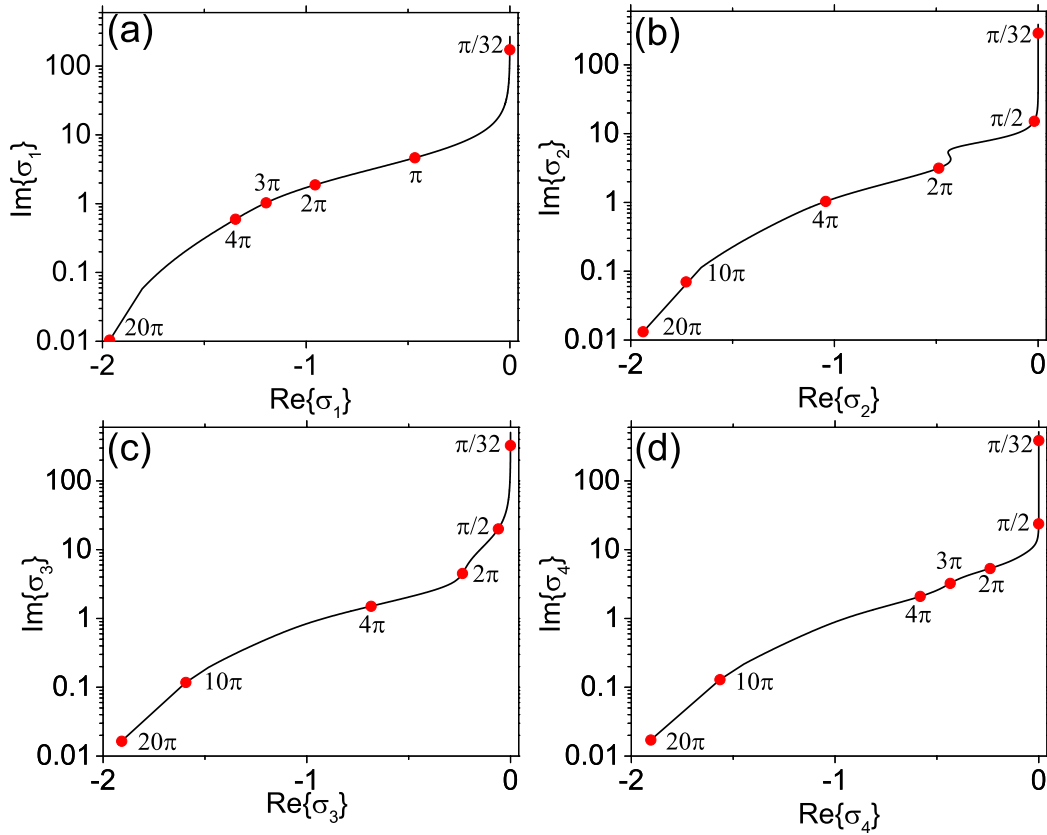


Figure 5.13 – Loci of the eigen-conductivities σ_1 (a), σ_2 (b), σ_3 (c) and σ_4 (d) of the first four vortex current modes of the triangle spanned on the complex plane as function of $x = 2\pi(l/\lambda)$; here l is the length of the triangle and λ is the wavelength in vacuum.

the real part of the vortex current modes 1, 2&2', 3 and 4 &4' of the triangle at $l/\lambda = 10^{-2}$, $l/\lambda = 1$ and $l/\lambda = 5$. The current modes on the same columns have the same eigen-conductivities, thus they are degenerate. As for the circle, the vortex current mode 1 of the equilateral triangle at $l/\lambda = 10^{-2}$ has a strong magnetic dipolar character. The modes 2&2' (degenerate) are composed of two different sets of current loops whose magnetic dipole moments are antiparallel. The modes 3&3' (degenerate) are composed of four identical sets of current loop with alternating magnetic dipole moments. Lastly, the vortex currents modes 4&4' are composed of two different sets of loops and show the same mirror symmetry of the mode 2&2'. Again, the number of vortices is conserved as l/λ increases and the mode patterns are preserved.

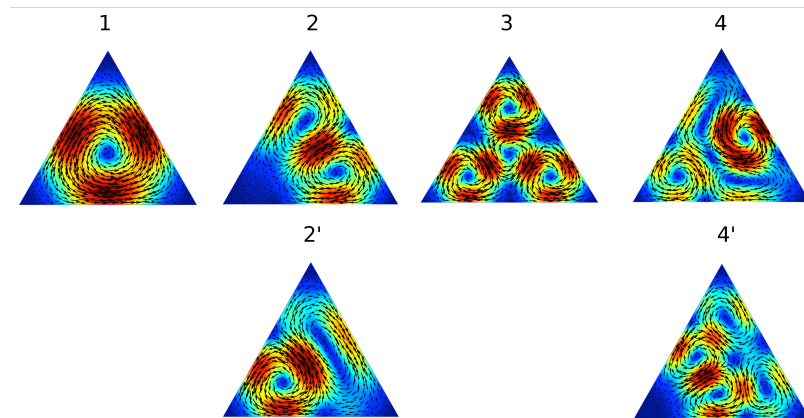


Figure 5.14 – Real part of the first four vortex current modes of a triangle at $l/\lambda = 10^{-2}$; here l is the triangle side and λ the wavelength in vacuum. The vectors are directed along $\text{Re}\{\mathbf{J}_n\}$ and the colors represent the intensity of $|\text{Re}\{\mathbf{J}_n\}|$

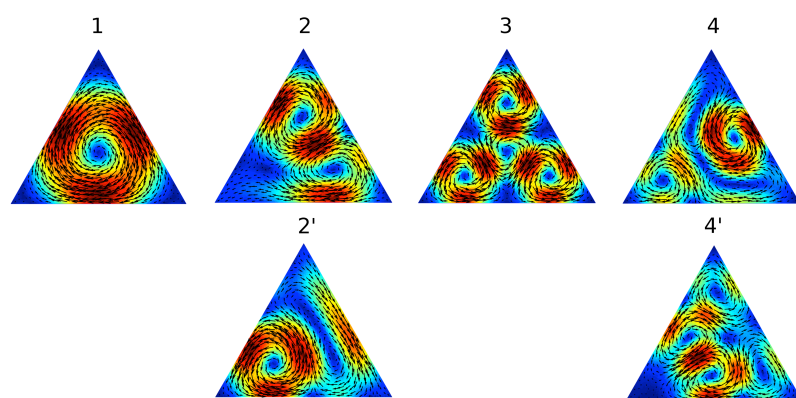


Figure 5.15 – Real part of the first four vortex current modes of a triangle at $l/\lambda = 1$; here l is the triangle side and λ the wavelength in vacuum. The vectors are directed along $\text{Re}\{\mathbf{J}_n\}$ and the colors represent the intensity of $|\text{Re}\{\mathbf{J}_n\}|$

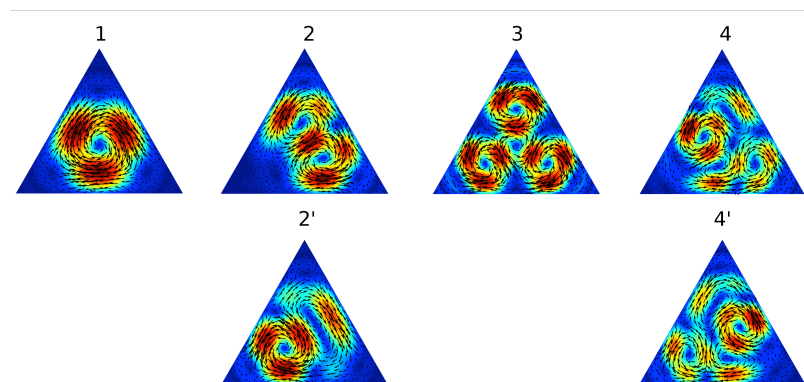


Figure 5.16 – Real part of the first four vortex current modes of a triangle at $l/\lambda = 5$; here l is the triangle side and λ the wavelength in vacuum. The vectors are directed along $\text{Re}\{\mathbf{J}_n\}$ and the colors represent the intensity of $|\text{Re}\{\mathbf{J}_n\}|$

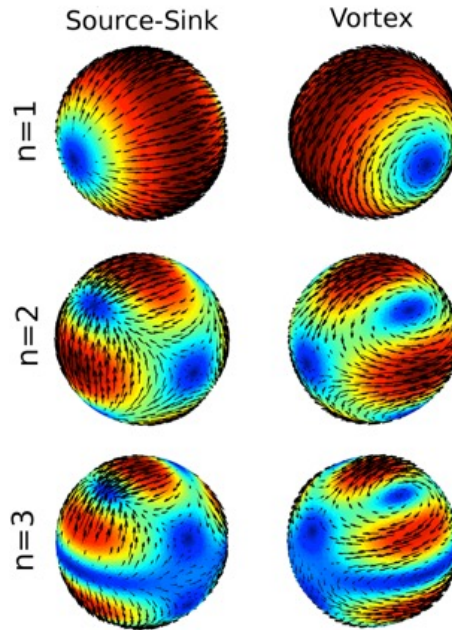


Figure 5.17 – Plots of the real part of source-sink and vortex current modes ($n = 1, 2, 3$) of a spherical surface. The direction of each arrow represents the direction of the mode at the corresponding point on the spherical surface, while the length of the arrow and the color describe its amplitude.

5.7 Current modes and eigen-conductivities for a closed surface

In this part, the behavior of the current modes and of the eigen-conductivities for a spherical surface is investigated.

Current modes

In Figure 5.17, the real parts of the first three source-sink and vortex current modes ($n = 1, 2, 3$) of a spherical surface are shown. In this case, the distributions of the current modes are independent of the frequency and spherical surface radius. The source-sink modes do not have a radial component of the magnetic field, while the vortex modes do not have a radial component of the electric field. They are therefore transverse magnetic (TM), and transverse electric (TE), respectively.

Eigen-conductivities

Now, the behavior of the eigen-conductivities as a function of the size parameter $x = 2\pi\left(\frac{l}{\lambda}\right)$ is shown, where l denotes the radius of the spherical surface. Figures

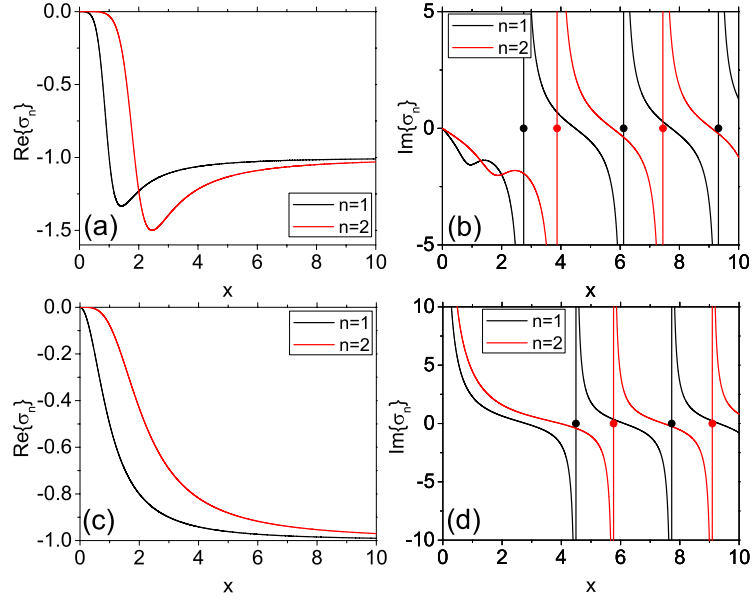


Figure 5.18 – Real and imaginary part of the eigen-conductivities σ_1 and σ_2 as a function of $x = 2\pi(\frac{l}{\lambda})$ for a spherical surface with radius l (λ is the wavelength in vacuum): source-sink current modes (a-b); vortex current modes (c-d). The black and red dots indicate the values of x in correspondence of which a spherical cavity bounded by a perfect electrical conductor resonates.

5.18(a) and 5.18(b) show, respectively, the behavior of the real part and imaginary parts of the eigen-conductivities of the first two source-sink current modes as x varies; Figures 5.18(c) and 5.18(d) show the same plots for the first two vortex current modes. Similarly to open surfaces, in the long wavelength limit both the source-sink and vortex modes exhibit negligible radiative losses, hence $\text{Re}\{\sigma_n\}$ approaches zero for $x \rightarrow 0$. For the source-sink current modes, $\text{Re}\{\sigma_n\}$ decreases as x increases and it exhibits a minimum at $x = 1.4$ for $n = 1$ and a minimum at $x = 2.4$ for $n = 2$, then it asymptotically approaches the value of -1 for $x \rightarrow \infty$. On the contrary, for the vortex current modes $\text{Re}\{\sigma_n\}$ monotonically decreases from 0 to -1 . Once again, this behaviour is analogous to the case of an open surface, where the $\text{Re}\{\sigma_n\}$ decreased monotonically for vortex modes and it had a minimum for source-sink modes. The behaviour of $\text{Im}\{\sigma_n\}$ is now described. It is possible to prove that, for a spherical surface, it results

$$\lim_{x \rightarrow 0} \text{Im}\{x^{-1}\sigma_n\} = -\frac{2n+1}{n(n+1)} \text{ for source-sink modes} \quad (5.36)$$

$$\lim_{x \rightarrow 0} \text{Im}\{x^{-1}\sigma_n\} = 2n+1 \text{ for vortex modes} \quad (5.37)$$

Therefore, for the source-sink current modes $\text{Im}\{\sigma_n\}$ approaches zero for $x \rightarrow 0$, while for the vortex current modes $\text{Im}\{\sigma_n\}$ diverge. This is consistent with the results obtained for open surfaces. In the end, note that $\text{Im}\{\sigma_n\}$ for both source-sink and vortex modes diverges in correspondence of an infinite countable set of the size parameters x , which coincide with the resonant values of the normalized radius of a spherical cavity bounded by a perfect electric conductor. Specifically, with black and red dots, figure 5.18 highlights the values of x in correspondence of which the cavity resonates. These values are given by the following expressions

$$\text{TM}_n \rightarrow \frac{d}{dx} \left[\sqrt{x} J_{n+\frac{1}{2}}(x) \right] = 0 \quad (5.38)$$

$$\text{TE}_n \rightarrow J_{n+\frac{1}{2}}(x) = 0 \quad (5.39)$$

where $J_v(x)$ is the Bessel function of first kind [132], [133]. As consequence, for closed surface the limit of $\text{Im}\{\sigma_n\}$ for $x \rightarrow \infty$ does not exist for both the source-sink and vortex current modes while $\text{Re}\{\sigma_n\} \rightarrow -1$ for $x \rightarrow \infty$. These behaviors differentiate the resonances of closed surfaces from the resonances of open surfaces.

5.8 Scattering from 2D object and resonant conditions

The width and the amplitude of the resonance peaks depend on the losses in the material and on the radiation losses. The real part of the eigen-conductivities of both types of current modes becomes negligible only in the long wavelength limit; otherwise, it is in the order of magnitude of 1. In order to simplify, the current mode expansion is used to study the scattering from a disk illuminated by a linearly polarized plane wave (with unitary amplitude), propagating normally to it.

$$\mathbf{J}_s(\mathbf{r}_s) = \sum_{n=1}^{\infty} \frac{\sigma_n}{\sigma_n - \zeta_0 \sigma} \langle \mathbf{J}_n^*, \sigma \mathbf{E}^{\parallel(0)} \rangle \mathbf{J}_n(\mathbf{r}_s) \quad (5.40)$$

In a graphene disk, source-sink current modes may be resonantly excited, while in a silicon disk vortex current modes may be resonantly excited.

5.8.1 Disk with negative imaginary part of the surface conductivity

Firstly an example of material with negative imaginary part of the surface conductivity is considered:

- a suspended high-doped (or gated) graphene disk
- radius of 100 nm
- the electromagnetic field scattered by the disk in a wavelength around $10\mu m$ is analyzed.
- the incident electromagnetic field is a plane wave linearly polarized, propagating normally to the disk

In this specific case (radius and wavelength), quantum effects can be considered negligible and interband transitions may be disregarded. The surface conductivity of the graphene is approximated as

$$\sigma = \frac{1}{R_0} \frac{\mu}{\hbar(j\omega + \frac{1}{\tau})} \quad (5.41)$$

where $R_0 = \pi\hbar/e^2$, μ is the chemical potential and τ is the electron relaxation time [?]. The chemical potential of the graphene is chosen in such a way that the disk resonates at $10\mu m$ on the first source-sink current mode, which has a strong dipolar character. Since $l/\lambda = 0.01$, the effects of the radiation losses are negligible. Around $10\mu m$, the effects of the graphene losses are negligible, too. Figure 5.19(a) shows the scattering efficiency. A very good agreement is found between the scattering cross sections obtained by using the analytical solution and the scattering cross section obtained by means of a full wave two-dimensional numerical code [87]. This fact validates the solution obtained with the suggested approach and the computation of the current modes and the eigen-conductivities. Besides the designed resonance at $10\mu m$, two Fano resonances emerge in both the spectra of the scattering efficiency and the near field amplitude. Figure 5.19(b) shows the maximum of the amplitude of the electric field on the disk surface. The 5.19(c) shows the resonant source-sink current modes excited in the graphene disk and the vertical dashed lines in Figures 5.19(a) and 5.19(b) indicate their resonant wavelengths evaluated by Eq. 5.32.

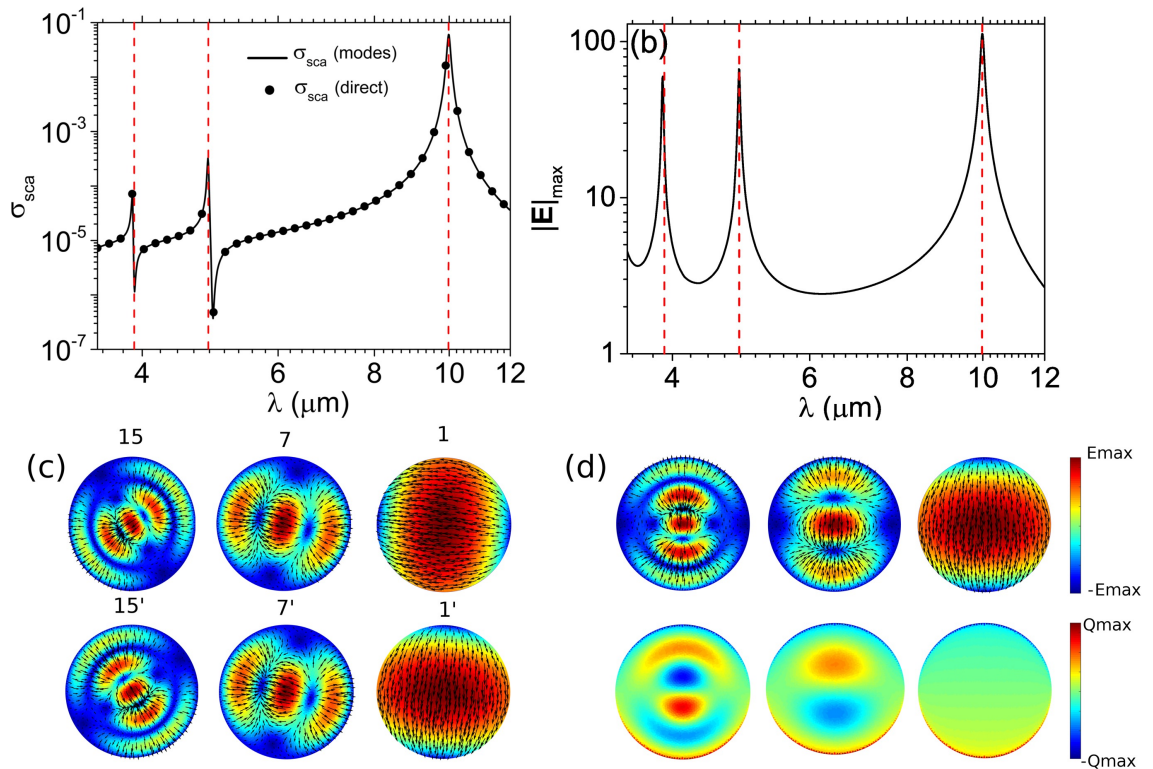


Figure 5.19 – Graphene disk with radius $l = 100$ nm, excited by a linearly polarized plane wave propagating normally to the disk. The graphene chemical potential has been designed to enforce the resonance of the electric dipolar mode at $\lambda = 10 \mu\text{m}$ (a) Spectra of scattering efficiency. The black points in the panel indicate the values of the scattering efficiency obtained by solving directly equation by a full wave 2D numerical code (b) Maximum amplitude of electric field on the surface The vertical dashed lines indicate the resonant wavelength (c) of the source-sink current modes (d) Distributions of the corresponding surface charge densities

5.8.2 Disk with positive imaginary part of the surface conductivity

Now an example of material with positive imaginary part of the surface conductivity is considered:

- a dielectric thin disk with relative permittivity $\varepsilon_r = 16$ (silicon)
- radius $l = 500\text{nm}$ and thickness $\Delta = 19.2\text{nm}$
- the electromagnetic field scattered by it in the wavelength range from $0.5\mu\text{m}$ to $1.25\mu\text{m}$ is considered
- the incident electromagnetic field is a plane wave linearly polarized, propagating normally to the disk.

Since the disk thickness Δ is much smaller than its radius and the wavelength, the thin disk may be represented as a circle with equivalent surface conductivity given by

$$\zeta_0\sigma = x\left(\frac{\Delta}{l}\right)(\varepsilon_r - 1)i \quad (5.42)$$

Given this expression, for the considered dielectric disk the imaginary part of $\zeta_0\sigma$ covers the interval (1.45,3.61). Figure 5.20(a) shows the scattering efficiency (black line). Again a very good agreement is found between the scattering cross sections obtained by using the expression 5.43 and the scattering cross section obtained by means of a full wave three-dimensional numerical code [82]. This fact again validates the solution obtained with the suggested approach and the computation of the current modes and the eigen-conductivities. Several current modes contribute to the scattered electromagnetic field. The vertical dashed lines in 5.20(a) indicate the values of the resonant wavelengths of the vortex current modes shown in Figure 5.20(c) $\lambda_2 = 980\text{ nm}$, $\lambda_6 = 696\text{ nm}$ and $\lambda_{13} = 556\text{ nm}$. Besides these resonant modes, the first two source-sink current modes of the disk contribute to the scattered field. These two degenerate modes are off resonance because their eigen-conductivities are bounded in the region of complex plane with the imaginary part belonging to the interval $(-2.95, 0.238)$, while the imaginary part of $\zeta_0\sigma$ varies between 1.45 and 3.61. Even if these modes are off resonance, their coupling amplitudes with the plane wave are very high because they have a strong electric dipole moment. To highlight the contribution of the most important current modes, figure 5.20(a) shows the partial scattering efficiencies defined as the scattering efficiency obtained by considering only

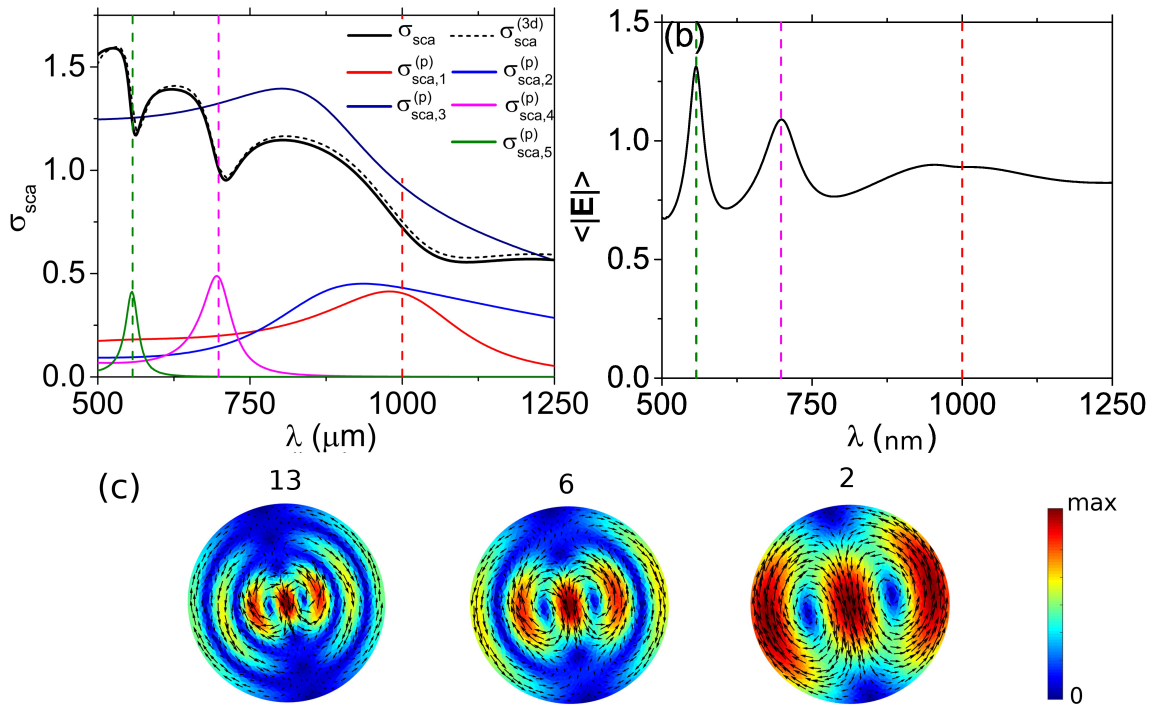


Figure 5.20 – silicon thin disk with radius $l = 500\text{nm}$ and thickness $\Delta = 19.2\text{nm}$, illuminated by a linearly polarized plane wave propagating normally to the disk. The vertical dashed lines indicate the positions of the resonant wavelengths (calculated in the “frequency picture”)

(a) Scattering efficiency and partial scattering efficiency

(b) Averaged near field enhancement

(c) Three vortex modes

The dashed line in the panel (a) indicates the values of the scattering efficiency $\sigma_{sca}^{(3d)}$ obtained by using a three dimensional full wave numerical code

one mode at a time [134]. The destructive interferences between the broad source-sink modes and one of the narrow vortex current mode shown in 5.20(c) give rise to the Fano resonances around $\lambda = 1106$ nm, $\lambda = 711$ nm and $\lambda = 563$ nm Figure 5.20(b) shows the averaged amplitude of the electric field on the disk surface. The vertical dashed lines always indicate the values of the resonant wavelengths of the vortex current modes shown in Figure 5.20(c).

5.9 Conclusions

The electromagnetic modes and resonances in the full wave electromagnetic scattering from 2D objects have been investigated. The current modes and the corresponding eigen-conductivities are solution of a linear eigenvalue problem. More specifically, the eigen-conductivity σ_n corresponding to the current modes \mathbf{J}_n is the value that the surface conductivity of the object (normalized to the vacuum admittance) should have so that the current mode \mathbf{J}_n is a free-source solution.

It was observed that as kl_c varies both source-sink current modes and vortex current modes preserve some topological features. The source –sink current modes, which in the long wavelength limit are irrotational, are characterized by a number of sources and sinks of the field lines that is conserved. Similarly, the vortex current modes, which in the long wavelength limit are solenoidal, are characterized by a number of vortexes of the field lines that is conserved. The surface current density induced on the object by an external excitation has been represented in terms of the current modes as follow

$$\mathbf{J}_s(\mathbf{r}_s) = \sum_{n=1}^{\infty} \frac{\sigma_n}{\sigma_n - \zeta_0 \sigma} \langle \mathbf{J}_n^*, \sigma \mathbf{E}^{\parallel(0)} \rangle \mathbf{J}_n(\mathbf{r}_s) \quad (5.43)$$

From the analysis of expansion coefficients, two different "picture" have been defined

- frequency picture
- material picture

Some representative examples for open surfaces (disk, equilateral triangle) and a closed surface (spherical surface) have been provided. Of each surface the diagrams on the complex plane of the loci of the eigen-conductivities and the related eigenfunctions have been analyzed. Finally, the scattering by two-dimensional objects with either positive or negative imaginary part of the surface conductivity is analyzed and the contributions of the different modes are examined.

Appendix A

Galerkin Theory

A.1 Hilbert Spaces

It is considered an inner-product space $(\mathbf{H}, (\cdot, \cdot))$, that is a linear space equipped with a symmetric bilinear form (\cdot, \cdot) characterized by the property

$$\begin{cases} (\mathbf{v}, \mathbf{v}) \geq 0 \quad \forall \mathbf{v} \in \mathbf{H} \\ (\mathbf{v}, \mathbf{v}) = 0 \leftrightarrow \mathbf{v} = 0 \end{cases} \quad (\text{A.1})$$

It is a Hilbert Space when the space $(\mathbf{H}, \|\cdot\|)$ is complete with respect to the distance function induced by the inner product.

$$\|\mathbf{v}\| = \sqrt{(\mathbf{v}, \mathbf{v})} \quad (\text{A.2})$$

The norm properties (positive definiteness and non-negative, absolute homogeneity, triangle inequality) are inherited from bilinear form properties. The completeness, instead, is expressed by the Cauchy criterion: the space \mathbf{H} is complete if every Cauchy sequence converges with respect to this norm to an element in the space. In short, it is possible to generalize the geometric methods from the two-dimensional and three-dimensional euclidean spaces to infinite-dimensional spaces. Geometric intuition plays an important role in many aspects of Hilbert space.

For instance, we consider the Pythagorean theorem

$$\|\mathbf{u} + \mathbf{v}\|^2 = (\mathbf{u} + \mathbf{v}, \mathbf{u} + \mathbf{v}) = (\mathbf{u}, \mathbf{u}) + 2(\mathbf{u}, \mathbf{v}) + (\mathbf{v}, \mathbf{v}) \quad (\text{A.3})$$

$$(\mathbf{u}, \mathbf{v}) = 0 \rightarrow \|\mathbf{u} + \mathbf{v}\|^2 = \|\mathbf{u}\|^2 + \|\mathbf{v}\|^2 \quad (\text{A.4})$$

and the parallelogram law

$$\|\mathbf{u} + \mathbf{v}\|^2 + \|\mathbf{u} - \mathbf{v}\|^2 = 2(\|\mathbf{u}\|^2 + \|\mathbf{v}\|^2) \quad (\text{A.5})$$

The inner-product allows to define, in addition to the distance function, the orthogonality between subsets. We define the following orthogonal complements

$$\mathbf{x}^\perp = \{\mathbf{v} \in H : (\mathbf{v}, \mathbf{x}) = 0\} \quad (\text{A.6})$$

$$M^\perp = \{\mathbf{v} \in H : (\mathbf{v}, \mathbf{x}) = 0 \quad \forall \mathbf{x} \in M\} \quad (\text{A.7})$$

A.1.1 Hilbert Projection Theorem

If M is a subspace of the Hilbert space H ($M \subset H$), $\mathbf{v} \in H \setminus M$ and

$$\delta = \inf\{\|\mathbf{v} - \mathbf{w}\| : \mathbf{w} \in M\} \quad (\text{A.8})$$

there exists $\mathbf{w}_0 \in M$ such that

- $\|\mathbf{v} - \mathbf{w}_0\| = \delta$
- $(\mathbf{v} - \mathbf{w}_0) \in M^\perp$

This theorem leads to the following observation: any Hilbert Space H can be written as direct sum via a subspace and the orthogonal complement

$$H = M \oplus M^\perp \quad (M \subset H) \quad (\text{A.9})$$

or, in extended form

$$\forall \mathbf{v} \in H \quad \exists! \mathbf{u} \in M, \mathbf{w} \in M^\perp : \mathbf{v} = \mathbf{u} + \mathbf{w} \quad (\text{A.10})$$

A.2 Sobolev Space

In order to tackle a problem numerically, the spaces C^k usually adopted appear appear do not appear suitable since they are based on a classical "local" definition of derivative, involving information about the function u only near the point x . This choice proves to be too restrictive since pointwise values of derivatives are not needed. As a result, it is necessary to develop a different "global" notion of derivative more suited to our aim: the so-called weak derivative. The function spaces associated with the weak derivative are the Sobolev spaces.

A.2.1 Weak Derivative

The key idea is to compare a not-so-smooth function with a very-smooth-function, definitely differentiable. In particular, g is said to be the weak derivative of order α of a given function $f \in L^1_{loc}(\mathbf{I})$ if

$$\int_{\mathbf{I}} g(x)\phi(x)dx = (-1)^{|\alpha|} \int_{\mathbf{I}} f(x)\phi^{(\alpha)}(x)dx \quad \forall \phi \in \mathcal{D}(\mathbf{I}) \rightarrow D_w^\alpha f = g \quad (\text{A.11})$$

where

- $\mathcal{D}(\mathbf{I})$ is the set of $C^\infty(\mathbf{I})$ functions with compact support in $\mathbf{I} = [a, b]$
- $L^1_{loc}(\mathbf{I})$ is the set of locally integrable functions

$$L^1_{loc}(\mathbf{I}) = \left\{ f : f \in L^1(\mathbf{K}) \quad \forall \text{ compact } \mathbf{K} \subset \text{interior } \mathbf{I} \right\} \quad (\text{A.12})$$

The weak derivative is characterized by the following properties

1. the new definition is consistent with the old one: if u is differentiable in the conventional (strong) sense, then its weak derivative is identical to its conventional strong derivative.
2. if two functions are weak derivatives of the same function, they are equal except on a set with Lebesgue measure zero, i.e., they are equal almost everywhere. As a result, if we consider equivalence classes of functions such that two functions are equivalent if they are equal almost everywhere, then the weak derivative is unique.
3. the classical rules for derivatives also hold for the weak derivative.

A.2.2 Sobolev Norm

Starting with the definition of weak derivatives, it is possible to define the following norm

$$\|f\|_{W^k_p(\mathbf{I})} = \left(\sum_{|\alpha| \leq k} \|D_w^\alpha f\|_{L^p(\mathbf{I})}^p \right)^{\frac{1}{p}} \quad 1 \leq p < \infty \quad (\text{A.13})$$

$$\|f\|_{W^\infty(\mathbf{I})} = \max_{|\alpha| \leq k} \|D_w^\alpha f\|_{L^\infty(\mathbf{I})} \quad p = \infty \quad (\text{A.14})$$

This enables the definition of the Sobolev Space

$$W^k_p(\mathbf{I}) = \left\{ f \in L^1_{loc}(\mathbf{I}) : \|f\|_{W^k_p(\mathbf{I})} < \infty \right\} \quad (\text{A.15})$$

These spaces have properties that make them particularly appealing, such as inclusion relations that provide some sort of ordering

$$k \leq m \rightarrow W_p^m(\mathbf{I}) \subset W_p^k(\mathbf{I}) \quad 1 \leq p \leq \infty \quad (\text{A.16})$$

$$1 \leq p \leq q \leq \infty \rightarrow W_q^k(\mathbf{I}) \subset W_p^k(\mathbf{I}) \quad 1 \leq k \leq \infty \quad (\text{A.17})$$

The fundamental reason why Sobolev spaces are so effective is that they are Hilbert spaces, consequently it is possible to exploit some tools providing existence and uniqueness results to weak formulated equations too.

A.3 Galerkin Theory

In order to explain the problem in its most general form, we give the following definitions

A bilinear form $a(\cdot, \cdot)$ on a normed linear space H is said to be bounded if

$$\exists C < \infty : |a(\mathbf{v}, \mathbf{w})| \leq C \|\mathbf{v}\|_H \|\mathbf{w}\|_H \quad \forall \mathbf{v}, \mathbf{w} \in H \quad (\text{A.18})$$

A bilinear form $a(\cdot, \cdot)$ on a normed linear space H is said to be coercive on $V \subset H$ if

$$\exists \alpha > 0 : a(\mathbf{v}, \mathbf{v}) \geq \alpha \|\mathbf{v}\|_H^2 \quad \forall \mathbf{v} \in V \quad (\text{A.19})$$

A.3.1 Formulation of Variational Problems

Suppose that the following conditions are valid

- $(H, (\cdot, \cdot))$ is a Hilbert space
- V is a (closed) subspace of H
- $a(\cdot, \cdot)$ is a bilinear form on V , not necessarily symmetric
- $a(\cdot, \cdot)$ is bounded on V
- $a(\cdot, \cdot)$ is coercive on V

Then the Variational Problem is the following:

$$\text{Given } F \in V', \text{ find } \mathbf{u} \in V \text{ such that } a(\mathbf{u}, \mathbf{v}) = F(\mathbf{v}) \quad \forall \mathbf{v} \in V \quad (\text{A.20})$$

If $a(\cdot, \cdot)$ is a symmetric bilinear form, the conditions ensure that it represents an inner product on V , so $(V, a(\cdot, \cdot))$ is a Hilbert Space. The Riesz Representation Theorem demonstrates the existence and uniqueness of the solution (*well-posedness*).

Only in this case, it is possible to prove the equivalence between the variational formulation and the following minimization problem:

$$\text{find } \mathbf{u} \in V \text{ such that } J(\mathbf{u}) \leq J(\mathbf{v}) \quad \forall \mathbf{v} \in V \quad (\text{A.21})$$

where $J(\mathbf{v})$ is the quadratic functional $J(\mathbf{v}) = a(\mathbf{v}, \mathbf{v}) - 2F(\mathbf{v})$. In the more general case, however, where there is no symmetry condition, the existence and uniqueness are assured by the Lax Milgram Theorem and the problem is *well-posed*.

A.3.2 Matrix form of Galerkin's equation

Starting from the problems just defined, it is possible to formulate an approximated problem: this possibility represents the *trait d'union* between the original formulation and the numerical one.

Ritz-Galerkin approximation problem: Given a finite-dimensional subspace $V_h \subset V$ and $F \in V'$, find $\mathbf{u}_h \in V_h$ such that $a(\mathbf{u}_h, \mathbf{v}) = F(\mathbf{v}) \quad \forall \mathbf{v} \in V_h$

It is important to underline two aspects about the approximate problem

- Under the conditions of Symmetric Variational Problem or more generally of Non-Symmetric Variational problems, $(V_h, a(\cdot, \cdot))$ is a Hilbert Space in its own right. As a result, Riesz Representation Theorem (Symmetric) and Lax-Milgram Theorem (Non-Symmetric) ensure the existence and uniqueness of the solution: the *well-posedness* (in the sense of Hadamard) of the Galerkin problem is inherited from the well-posedness of the original problem [135].
- While the equation has remained unchanged, the spaces have changed: reducing the problem to a finite-dimensional vector subspace allows us to numerically compute u_n as a finite linear combination of the basis vectors in V_h .

Let $\{\mathbf{e}_1, \mathbf{e}_2, \dots, \mathbf{e}_{N_n}\}$ be a basis for V_h

$$\mathbf{u}_h = \sum_{j=1}^{N_n} U_j \mathbf{e}_j \rightarrow a(\mathbf{u}_h, \mathbf{v}) = a\left(\sum_{j=1}^{N_n} U_j \mathbf{e}_j, \mathbf{v}\right) = F(\mathbf{v}) \quad (\text{A.22})$$

$$\sum_{j=1}^{N_n} U_j a(\mathbf{e}_j, \mathbf{v}) = F(\mathbf{v}) \quad (\text{A.23})$$

$$\mathbf{v} = \sum_{i=1}^{N_n} \alpha_i \mathbf{e}_i \rightarrow \sum_{j=1}^{N_n} U_j a \left(\mathbf{e}_j, \sum_{i=1}^{N_n} \alpha_i \mathbf{e}_i \right) = \mathbf{F} \left(\sum_{i=1}^{N_n} \alpha_i \mathbf{e}_i \right) \quad (\text{A.24})$$

$$\sum_{i=1}^{N_n} \alpha_i \sum_{j=1}^{N_n} U_j a(\mathbf{e}_j, \mathbf{e}_i) = \sum_{i=1}^{N_n} \alpha_i \mathbf{F}(\mathbf{e}_i) \quad (\text{A.25})$$

$$\sum_{j=1}^{N_n} U_j a(\mathbf{e}_j, \mathbf{e}_i) = \mathbf{F}(\mathbf{e}_i) \rightarrow \underline{\underline{\mathbf{A}}} \cdot \mathbf{U} = \mathbf{F} \quad (\text{A.26})$$

In summary, the method converts a continuous infinite-dimensional integral equation into a discrete finite-dimensional matrix equation where

- $\underline{\underline{\mathbf{A}}}$ is the system matrix
- \mathbf{F} is the excitation vector
- \mathbf{U} contains the unknown coefficients to be determined

Bibliography

- [1] M. Khorasaninejad, F. Aieta, P. Kanhaiya, M. A. Kats, P. Genevet, D. Rousso, and F. Capasso, “Achromatic Metasurface Lens at Telecommunication Wavelengths,” *Nano Letters*, vol. 15, pp. 5358–5362, Aug. 2015.
- [2] W. C. Chew, J.-M. Jin, E. Michielssen, and J. Song, eds., *Fast and Efficient Algorithms in Computational Electromagnetics*. Boston: Artech House, July 2000.
- [3] O. M. Bucci and G. D. Massa, “Use of characteristic modes in multiple-scattering problems,” *Journal of Physics D: Applied Physics*, vol. 28, p. 2235, Nov. 1995.
- [4] G. Angiulli, G. Amendola, and G. D. Massa, “Characteristic Modes in Multiple Scattering by Conducting Cylinders of Arbitrary Shape,” *Electromagnetics*, vol. 18, pp. 593–612, Nov. 1998. Publisher: Taylor & Francis _eprint: <https://doi.org/10.1080/02726349808908615>.
- [5] B. Cockburn, G. E. Karniadakis, and C.-W. Shu, *Discontinuous Galerkin Methods: Theory, Computation and Applications*. Springer Science & Business Media, Dec. 2012. Google-Books-ID: uOhrCAAAQBAJ.
- [6] S. Rao, D. Wilton, and A. Glisson, “Electromagnetic scattering by surfaces of arbitrary shape,” *IEEE Transactions on Antennas and Propagation*, vol. 30, pp. 409–418, May 1982. Conference Name: IEEE Transactions on Antennas and Propagation.
- [7] A. Bossavit, *Computational electromagnetism: variational formulations, complementarity, edge elements*. Academic Press, 1998.
- [8] R. Albanese and G. Rubinacci, “Integral formulation for 3D eddy-current computation using edge elements,” *IEE Proceedings A (Physical Science, Measurement and Instrumentation, Management and Education, Reviews)*, vol. 135, no. 7, pp. 457–462, 1988.

- [9] G. Rubinacci and A. Tamburrino, "A broadband volume integral formulation based on edge-elements for full-wave analysis of lossy interconnects," *IEEE transactions on antennas and propagation*, vol. 54, no. 10, pp. 2977–2989, 2006.
- [10] D. Wilton, J. Lim, and S. Rao, "A novel technique to calculate the electromagnetic scattering by surfaces of arbitrary shape," *URSI Radio Science Meeting*, p. 322, 1993.
- [11] W.-L. Wu, A. W. Glisson, and D. Kajfez, "A study of two numerical solution procedures for the electric field integral equation at low frequency," *Applied Computational Electromagnetics Society Journal*, vol. 10, no. 3, pp. 69–80, 1995.
- [12] L. Trintinalia and H. Ling, "First Order Triangular Patch Basis Functions for Electromagnetic Scattering Analysis," *Journal of Electromagnetic Waves and Applications*, vol. 15, pp. 1521–1537, Jan. 2001. Publisher: Taylor & Francis
_eprint: <https://doi.org/10.1163/156939301X00085>.
- [13] A. Buffa and S. H. Christiansen, "A Dual Finite Element Complex on the Barycentric Refinement," *Mathematics of Computation*, vol. 76, no. 260, pp. 1743–1769, 2007. Publisher: American Mathematical Society.
- [14] R. Graglia, D. Wilton, and A. Peterson, "Higher order interpolatory vector bases for computational electromagnetics," *IEEE Transactions on Antennas and Propagation*, vol. 45, pp. 329–342, Mar. 1997. Conference Name: IEEE Transactions on Antennas and Propagation.
- [15] C. F. Bohren and D. R. Huffman, *Absorption and Scattering of Light by Small Particles*. Wiley, 1998.
- [16] L.-W. Li, X.-K. Kang, and M.-S. Leong, *Spheroidal Wave Functions in Electromagnetic Theory*. John Wiley & Sons, Apr. 2004.
- [17] P. H. Moon, *Field Theory Handbook: Including Coordinate Systems, Differential Equations, and Their Solutions*. World Publishing Corporation, 1991. Google-Books-ID: 2oZPcAAACAAJ.
- [18] R. Garbacz, "Modal expansions for resonance scattering phenomena," *Proceedings of the IEEE*, vol. 53, no. 8, pp. 856–864, 1965.
- [19] Y. Chang and R. Harrington, "A surface formulation for characteristic modes of material bodies," *IEEE Transactions on Antennas and Propagation*, vol. 25,

- pp. 789–795, Nov. 1977. Conference Name: IEEE Transactions on Antennas and Propagation.
- [20] R. Harrington, J. Mautz, and Yu Chang, “Characteristic modes for dielectric and magnetic bodies,” *IEEE Transactions on Antennas and Propagation*, vol. 20, pp. 194–198, Mar. 1972.
- [21] Y. Chen and C.-F. Wang, *Characteristic Modes: Theory and Applications in Antenna Engineering*. John Wiley & Sons, June 2015. Google-Books-ID: suob-BgAAQBAJ.
- [22] M. Faenzi, G. Minatti, D. González-Ovejero, F. Caminita, E. Martini, C. Della Giovampaola, and S. Maci, “Metasurface Antennas: New Models, Applications and Realizations,” *Scientific Reports*, vol. 9, p. 10178, July 2019.
- [23] C. Forestiere, G. Gravina, G. Miano, M. Pascale, and R. Tricarico, “Electromagnetic modes and resonances of two-dimensional bodies,” *Phys. Rev. B*, vol. 99, p. 155423, Apr. 2019.
- [24] C. Forestiere, G. Gravina, G. Miano, G. Rubinacci, and A. Tamburrino, “Static surface mode expansion for the full-wave scattering from penetrable objects,” *arXiv:2201.11058 [cond-mat, physics:physics]*, Jan. 2022. arXiv: 2201.11058.
- [25] S. A. Maier, *Plasmonics: fundamentals and applications*. Springer Science & Business Media, 2007.
- [26] U. Kreibig and M. Vollmer, *Optical properties of metal clusters*, vol. 25. Springer Science & Business Media, 2013.
- [27] J. A. Schuller, E. S. Barnard, W. Cai, Y. C. Jun, J. S. White, and M. L. Brongersma, “Plasmonics for extreme light concentration and manipulation,” *Nat. Mater.*, vol. 9, pp. 193–204, 2010.
- [28] J. N. Anker, W. P. Hall, O. Lyandres, N. C. Shah, J. Zhao, and R. P. Van Duyne, “Biosensing with plasmonic nanosensors,” *Nature materials*, vol. 7, no. 6, pp. 442–453, 2008.
- [29] M. Kauranen and A. V. Zayats, “Nonlinear plasmonics,” *Nature Photonics*, vol. 6, no. 11, pp. 737–748, 2012.
- [30] H. A. Atwater and A. Polman, “Plasmonics for improved photovoltaic devices,” *Nature materials*, vol. 9, no. 3, pp. 205–213, 2010.

- [31] A. Aubry, D. Y. Lei, A. I. Fernández-Domínguez, Y. Sonnefraud, S. A. Maier, and J. B. Pendry, “Plasmonic Light-Harvesting Devices over the Whole Visible Spectrum,” *Nano Letters*, vol. 10, pp. 2574–2579, July 2010.
- [32] N. Engheta and R. W. Ziolkowski, *Metamaterials: Physics and Engineering Explorations*. John Wiley & Sons, June 2006.
- [33] D. R. Smith, J. B. Pendry, and M. C. K. Wiltshire, “Metamaterials and Negative Refractive Index,” *Science*, vol. 305, pp. 788–792, Aug. 2004.
- [34] A. Sihvola, “Metamaterials in electromagnetics,” *Metamaterials*, vol. 1, pp. 2–11, Mar. 2007.
- [35] A. Alù and N. Engheta, “Achieving transparency with plasmonic and metamaterial coatings,” *Phys. Rev. E*, vol. 72, p. 016623, July 2005. Publisher: American Physical Society.
- [36] A. Alù and N. Engheta, “Multifrequency Optical Invisibility Cloak with Layered Plasmonic Shells,” *Physical Review Letters*, vol. 100, p. 113901, Mar. 2008.
- [37] A. Nicolet and F. Zolla, “Cloaking with Curved Spaces,” *Science*, vol. 323, pp. 46–47, Jan. 2009.
- [38] A. Sihvola, “Enabling Optical Analog Computing with Metamaterials,” *Science*, vol. 343, pp. 144–145, Jan. 2014.
- [39] A. Silva, F. Monticone, G. Castaldi, V. Galdi, A. Alù, and N. Engheta, “Performing mathematical operations with metamaterials,” *Science*, vol. 343, no. 6167, pp. 160–163, 2014.
- [40] F. Zangeneh-Nejad, D. L. Sounas, A. Alù, and R. Fleury, “Analogue computing with metamaterials,” *Nature Reviews Materials*, vol. 6, pp. 207–225, Mar. 2021.
- [41] J. B. Pendry, “Negative Refraction Makes a Perfect Lens,” *Physical Review Letters*, vol. 85, pp. 3966–3969, Oct. 2000.
- [42] S. Kawata, Y. Inouye, and P. Verma, “Plasmonics for near-field nano-imaging and superlensing,” *Nature Photonics*, vol. 3, pp. 388–394, July 2009.
- [43] A. Nicolet, F. Zolla, and C. Geuzaine, “Transformation Optics, Generalized Cloaking and Superlenses,” *IEEE Transactions on Magnetics*, vol. 46, pp. 2975–2981, Aug. 2010.

- [44] A. Alu and N. Engheta, “Physical insight into the "growing" evanescent fields of double-negative metamaterial lenses using their circuit equivalence,” *IEEE Transactions on Antennas and Propagation*, vol. 54, pp. 268–272, Jan. 2006.
- [45] J. B. Khurgin, “How to deal with the loss in plasmonics and metamaterials,” *Nature nanotechnology*, vol. 10, no. 1, pp. 2–6, 2015.
- [46] A. B. Evlyukhin, C. Reinhardt, A. Seidel, B. S. Luk’yanchuk, and B. N. Chichkov, “Optical response features of Si-nanoparticle arrays,” *Phys. Rev. B*, vol. 82, p. 045404, July 2010.
- [47] A. B. Evlyukhin, C. Reinhardt, and B. N. Chichkov, “Multipole light scattering by nonspherical nanoparticles in the discrete dipole approximation,” *Phys. Rev. B*, vol. 84, p. 235429, Dec. 2011.
- [48] A. García-Etxarri, R. Gómez-Medina, L. S. Froufe-Pérez, C. López, L. Chantada, F. Scheffold, J. Aizpurua, M. Nieto-Vesperinas, and J. J. Sáenz, “Strong magnetic response of submicron Silicon particles in the infrared,” *Opt. Express*, vol. 19, pp. 4815–4826, Mar. 2011.
- [49] A. I. Kuznetsov, A. E. Miroshnichenko, M. L. Brongersma, Y. S. Kivshar, and B. Luk’yanchuk, “Optically resonant dielectric nanostructures,” *Science*, vol. 354, no. 6314, 2016.
- [50] S. Kruk and Y. Kivshar, “Functional meta-optics and nanophotonics govern by Mie resonances,” *ACS Photonics*, vol. 4, no. 11, pp. 2638–2649, 2017.
- [51] J. V. Bladel, “The Excitation of Dielectric Resonators of Very High Permittivity,” *IEEE Transactions on Microwave Theory and Techniques*, vol. 23, pp. 208–217, Feb. 1975.
- [52] H. C. van de Hulst, “Light scattering by small particles. New York (John Wiley and Sons), London (Chapman and Hall),” 1957.
- [53] G. Videen and W. S. Bickel, “Light-scattering resonances in small spheres,” *Physical Review A*, vol. 45, no. 8, p. 6008, 1992.
- [54] R. J. Cava, “Dielectric materials for applications in microwave communications—Basis of a presentation given at Materials Discussion No. 3, 26–29 September, 2000, University of Cambridge, UK.,” *Journal of Materials Chemistry*, vol. 11, no. 1, pp. 54–62, 2001.

- [55] R. K. Mongia and P. Bhartia, “Dielectric resonator antennas—a review and general design relations for resonant frequency and bandwidth,” *International Journal of Microwave and Millimeter-Wave Computer-Aided Engineering*, vol. 4, no. 3, pp. 230–247, 1994.
- [56] I. M. Reaney and D. Iddles, “Microwave Dielectric Ceramics for Resonators and Filters in Mobile Phone Networks,” *Journal of the American Ceramic Society*, vol. 89, no. 7, pp. 2063–2072, 2006.
- [57] H. Schlicke, “Quasi-Degenerated Modes in High-eps Dielectric Cavities,” *Journal of Applied Physics*, vol. 24, no. 2, pp. 187–191, 1953.
- [58] G. Rupprecht and R. O. Bell, “Dielectric Constant in Paraelectric Perovskites,” *Phys. Rev.*, vol. 135, pp. A748–A752, Aug. 1964.
- [59] J. Sethares and S. Naumann, “Design of microwave dielectric resonators,” *IEEE Transactions on Microwave Theory and Techniques*, vol. 14, no. 1, pp. 2–7, 1966.
- [60] A. B. Evlyukhin, S. M. Novikov, U. Zywietz, R. L. Eriksen, C. Reinhardt, S. I. Bozhevolnyi, and B. N. Chichkov, “Demonstration of magnetic dipole resonances of dielectric nanospheres in the visible region,” *Nano letters*, vol. 12, no. 7, pp. 3749–3755, 2012.
- [61] A. I. Kuznetsov, A. E. Miroshnichenko, Y. H. Fu, J. Zhang, and B. Luk’Yanchuk, “Magnetic light,” *Scientific Reports*, vol. 2, p. 492, 2012.
- [62] D. Smirnova and Y. S. Kivshar, “Multipolar nonlinear nanophotonics,” *Optica*, vol. 3, pp. 1241–1255, Nov. 2016.
- [63] M. K. Schmidt, R. Esteban, J. J. Sáenz, I. Suárez-Lacalle, S. Mackowski, and J. Aizpurua, “Dielectric antennas - a suitable platform for controlling magnetic dipolar emission,” *Opt. Express*, vol. 20, pp. 13636–13650, June 2012.
- [64] B. Rolly, B. Bebey, S. Bidault, B. Stout, and N. Bonod, “Promoting magnetic dipolar transition in trivalent lanthanide ions with lossless Mie resonances,” *Phys. Rev. B*, vol. 85, p. 245432, June 2012.
- [65] T. Feng, Y. Xu, Z. Liang, and W. Zhang, “All-dielectric hollow nanodisk for tailoring magnetic dipole emission,” *Opt. Lett.*, vol. 41, pp. 5011–5014, Nov. 2016.

- [66] J. Li, N. Verellen, and P. Van Dorpe, “Enhancing Magnetic Dipole Emission by a Nano-Doughnut-Shaped Silicon Disk,” *ACS Photonics*, vol. 4, no. 8, pp. 1893–1898, 2017.
- [67] D. G. Baranov, R. S. Savelev, S. V. Li, A. E. Krasnok, and A. Alù, “Modifying magnetic dipole spontaneous emission with nanophotonic structures (Laser Photonics Rev. 11(3)/2017),” *Laser & Photonics Reviews*, vol. 11, no. 3, pp. 1770031–n/a, 2017.
- [68] I. Staude, A. E. Miroschnichenko, M. Decker, N. T. Fofang, S. Liu, E. Gonzales, J. Dominguez, T. S. Luk, D. N. Neshev, I. Brener, and others, “Tailoring directional scattering through magnetic and electric resonances in subwavelength silicon nanodisks,” *ACS nano*, vol. 7, no. 9, pp. 7824–7832, 2013.
- [69] J. v. d. Groep, T. Coenen, S. A. Mann, and A. Polman, “Direct imaging of hybridized eigenmodes in coupled silicon nanoparticles,” *Optica*, vol. 3, pp. 93–99, Jan. 2016.
- [70] P. Kapitanova, V. Ternovski, A. Miroschnichenko, N. Pavlov, P. Belov, Y. Kivshar, and M. Tribelsky, “Giant field enhancement in high-index dielectric subwavelength particles,” *Scientific Reports*, vol. 7, no. 1, p. 731, 2017.
- [71] B. Luk’yanchuk, N. I. Zheludev, S. A. Maier, N. J. Halas, P. Nordlander, H. Giessen, and C. T. Chong, “The Fano resonance in plasmonic nanostructures and metamaterials,” *Nature materials*, vol. 9, no. 9, pp. 707–715, 2010.
- [72] C. Forestiere, G. Miano, M. Pascale, and R. Tricarico, “A Full-Retarded Spectral Technique for the Analysis of Fano Resonances in a Dielectric Nanosphere,” in *Fano Resonances in Optics and Microwaves: Physics and Applications* (E. Kamenetskii, A. Sadreev, and A. Miroschnichenko, eds.), pp. 185–218, Cham: Springer International Publishing, 2018.
- [73] A. Taflove and S. C. Hagness, *Computational Electrodynamics: The Finite-Difference Time-Domain Method*. Artech House Publishers, 3rd ed. ed., 2005.
- [74] J. G. Van Bladel, *Electromagnetic fields*, vol. 19. John Wiley & Sons, 2007.
- [75] J. R. Mautz and R. F. Harrington, “Electromagnetic Scattering from a homogeneous material body of revolution,” *Arch. Elektron. Uebertraeg.*, vol. 33, pp. 71–80, 1979.

- [76] P. Yla-Oijala and M. Taskinen, “Electromagnetic scattering analysis with combined field integral equations,” in *Antennas and Propagation Society International Symposium, 2007 IEEE*, pp. 4869–4872, June 2007.
- [77] C. Muller, *Foundations of the Mathematical Theory of Electromagnetic Waves*. New York: Springer, 1969.
- [78] P. Yla-Oijala and M. Taskinen, “Well-conditioned Muller formulation for electromagnetic scattering by dielectric objects,” *Antennas and Propagation, IEEE Transactions on*, vol. 53, pp. 3316–3323, Oct. 2005.
- [79] R. F. Harrington, “Boundary Integral Formulations for Homogeneous Material Bodies,” *Journal of Electromagnetic Waves and Applications*, vol. 3, no. 1, pp. 1–15, 1969.
- [80] A. Zhu and S. Gedney, “Comparison of the Muller and PMWCHT surface integral formulations for the locally corrected Nystrom method,” in *Antennas and Propagation Society International Symposium, 2004. IEEE*, vol. 4, pp. 3871 – 3874 Vol.4, June 2004.
- [81] P. Yla-Oijala and M. Taskinen, “Application of combined field Integral equation for electromagnetic scattering by dielectric and composite objects,” *Antennas and Propagation, IEEE Transactions on*, vol. 53, pp. 1168–1173, Mar. 2005.
- [82] C. Forestiere, G. Iadarola, G. Rubinacci, A. Tamburrino, L. D. Negro, and G. Miano, “Surface integral formulations for the design of plasmonic nanostructures,” *JOSA A*, vol. 29, pp. 2314–2327, Nov. 2012.
- [83] D. R. Wilton and A. W. Glisson, “On improving the electric field integral equation at low frequencies,” (Los Angeles, CA), pp. 22–24, June 1981.
- [84] M. Burton and S. Kashyap, “A study of a recent, moment-method algorithm that is accurate to very low frequencies,” *Applied Computational Electromagnetics Society Journal*, vol. 10, pp. 58–68, 1995. Publisher: APPLIED COMPUTATIONAL ELECTROMAGNETICS SOCIETY INC.
- [85] G. Vecchi, “Loop-star decomposition of basis functions in the discretization of the EFIE,” *IEEE Transactions on Antennas and Propagation*, vol. 47, pp. 339–346, Feb. 1999. Conference Name: IEEE Transactions on Antennas and Propagation.

- [86] F. P. Andriulli, “Loop-Star and Loop-Tree Decompositions: Analysis and Efficient Algorithms,” *IEEE Transactions on Antennas and Propagation*, vol. 60, pp. 2347–2356, May 2012. Conference Name: IEEE Transactions on Antennas and Propagation.
- [87] G. Miano and F. Villone, “A surface integral formulation of Maxwell equations for topologically complex conducting domains,” *IEEE Transactions on Antennas and Propagation*, vol. 53, pp. 4001–4014, Dec. 2005. Conference Name: IEEE Transactions on Antennas and Propagation.
- [88] J.-S. Zhao and W. C. Chew, “Integral equation solution of Maxwell’s equations from zero frequency to microwave frequencies,” *IEEE Transactions on Antennas and Propagation*, vol. 48, pp. 1635–1645, Oct. 2000. Conference Name: IEEE Transactions on Antennas and Propagation.
- [89] S. Chen, W. C. Chew, J. Song, and J.-S. Zhao, “Analysis of low frequency scattering from penetrable scatterers,” *IEEE Transactions on Geoscience and Remote Sensing*, vol. 39, pp. 726–735, Apr. 2001. Conference Name: IEEE Transactions on Geoscience and Remote Sensing.
- [90] P. Ylä-Oijala, H. Wallén, D. C. Tzarouchis, and A. Sihvola, “Surface Integral Equation-Based Characteristic Mode Formulation for Penetrable Bodies,” *IEEE Transactions on Antennas and Propagation*, vol. 66, pp. 3532–3539, July 2018. Conference Name: IEEE Transactions on Antennas and Propagation.
- [91] M. Taskinen and P. Ylä-Oijala, “Current and charge Integral equation formulation,” *IEEE Transactions on Antennas and Propagation*, vol. 54, pp. 58–67, Jan. 2006. Conference Name: IEEE Transactions on Antennas and Propagation.
- [92] Z. G. Qian and W. C. Chew, “An augmented electric field integral equation for high-speed interconnect analysis,” *Microwave and Optical Technology Letters*, vol. 50, no. 10, pp. 2658–2662, 2008. [_eprint: https://onlinelibrary.wiley.com/doi/pdf/10.1002/mop.23736](https://onlinelibrary.wiley.com/doi/pdf/10.1002/mop.23736).
- [93] R. F. Harrington, *Field computation by moment methods*. Wiley-IEEE Press, 1993.
- [94] I. D. Mayergoyz, D. R. Fredkin, and Z. Zhang, “Electrostatic (plasmon) resonances in nanoparticles,” *Phys. Rev. B*, vol. 72, p. 155412, Oct. 2005.

- [95] G. Miano, G. Rubinacci, and A. Tamburrino, “Numerical Modeling for the Analysis of Plasmon Oscillations in Metallic Nanoparticles,” *IEEE Transactions on Antennas and Propagation*, vol. 58, no. 9, pp. 2920–2933, 2010.
- [96] C. Forestiere, G. Miano, G. Rubinacci, M. Pascale, A. Tamburrino, R. Tricarico, and S. Ventre, “Magnetoquasistatic resonances of small dielectric objects,” *Phys. Rev. Research*, vol. 2, p. 013158, Feb. 2020.
- [97] C. Forestiere, G. Miano, M. Pascale, and R. Tricarico, “Quantum theory of radiative decay rate and frequency shift of surface plasmon modes,” *Physical Review A*, vol. 102, p. 043704, Oct. 2020. Publisher: American Physical Society.
- [98] C. Forestiere, G. Miano, and G. Rubinacci, “Resonance frequency and radiative Q-factor of plasmonic and dielectric modes of small objects,” *Phys. Rev. Research*, vol. 2, p. 043176, Nov. 2020.
- [99] C. Forestiere and G. Miano, “Time-domain formulation of electromagnetic scattering based on a polarization-mode expansion and the principle of least action,” *Physical Review A*, vol. 104, p. 013512, July 2021. Publisher: American Physical Society.
- [100] G. Vecchi, L. Matekovits, P. Pirinoli, and M. Orefice, “Hybrid spectral-spatial method for the analysis of printed antennas,” *Radio Science*, vol. 31, pp. 1263–1270, Sept. 1996. Conference Name: Radio Science.
- [101] G. Vecchi, L. Matekovits, P. Pirinoli, and M. Orefice, “A numerical regularization of the EFIE for three-dimensional planar structures in layered media (invited article),” *International Journal of Microwave and Millimeter-Wave Computer-Aided Engineering*, vol. 7, no. 6, pp. 410–431, 1997.
_eprint: <https://onlinelibrary.wiley.com/doi/pdf/10.1002/%28SICI%291522-6301%28199711%297%3A6%3C410%3A%3AAID-MMCE4%3E3.0.CO%3B2-R>.
- [102] A. Nosich, “The method of analytical regularization in wave-scattering and eigenvalue problems: foundations and review of solutions,” *IEEE Antennas and Propagation Magazine*, vol. 41, pp. 34–49, June 1999. Conference Name: IEEE Antennas and Propagation Magazine.
- [103] H. Golub and C. F. V. Loan, *Matrix Computations*. Baltimore, MD: Johns Hopkins University Press, 1983.

- [104] R. Graglia, “On the numerical integration of the linear shape functions times the 3-D Green’s function or its gradient on a plane triangle,” *Antennas and Propagation, IEEE Transactions on*, vol. 41, pp. 1448–1455, Oct. 1993.
- [105] G. Mie, “Beiträge zur Optik trüber Medien, speziell kolloidaler Metallösungen,” *Annalen der physik*, vol. 330, no. 3, pp. 377–445, 1908.
- [106] P. B. Johnson and R. W. Christy, “Optical Constants of the Noble Metals,” *Phys. Rev. B*, vol. 6, pp. 4370–4379, Dec. 1972.
- [107] P.-O. Persson and G. Strang, “A Simple Mesh Generator in Matlab,” *SIAM Review*, vol. 46, no. 2, pp. 329–345, 2004. Publisher: Society for Industrial and Applied Mathematics.
- [108] F. Xia, H. Wang, D. Xiao, M. Dubey, and A. Ramasubramaniam, “Two-dimensional material nanophotonics,” *Nature Photonics*, vol. 8, pp. 899–907, Dec. 2014. Number: 12 Publisher: Nature Publishing Group.
- [109] K. S. Novoselov, A. Mishchenko, A. Carvalho, and A. H. C. Neto, “2D materials and van der Waals heterostructures,” *Science*, July 2016. Publisher: American Association for the Advancement of Science.
- [110] Y. Li, Z. Li, C. Chi, H. Shan, L. Zheng, and Z. Fang, “Plasmonics of 2D Nanomaterials: Properties and Applications,” *Advanced Science*, vol. 4, no. 8, p. 1600430, 2017. [_eprint: https://onlinelibrary.wiley.com/doi/pdf/10.1002/advs.201600430](https://onlinelibrary.wiley.com/doi/pdf/10.1002/advs.201600430).
- [111] Z. Sun, A. Martinez, and F. Wang, “Optical modulators with 2D layered materials,” *Nature Photonics*, vol. 10, pp. 227–238, Apr. 2016. Number: 4 Publisher: Nature Publishing Group.
- [112] D. N. Basov, M. M. Fogler, and F. J. G. d. Abajo, “Polaritons in van der Waals materials,” *Science*, Oct. 2016. Publisher: American Association for the Advancement of Science.
- [113] T. Low, A. Chaves, J. D. Caldwell, A. Kumar, N. X. Fang, P. Avouris, T. F. Heinz, F. Guinea, L. Martin-Moreno, and F. Koppens, “Polaritons in layered two-dimensional materials,” *Nature Materials*, vol. 16, pp. 182–194, Feb. 2017. Number: 2 Publisher: Nature Publishing Group.

- [114] K. F. Mak and J. Shan, “Photonics and optoelectronics of 2D semiconductor transition metal dichalcogenides,” *Nature Photonics*, vol. 10, pp. 216–226, Apr. 2016. Number: 4 Publisher: Nature Publishing Group.
- [115] R. Harrington and J. Mautz, “An impedance sheet approximation for thin dielectric shells,” *IEEE Transactions on Antennas and Propagation*, vol. 23, pp. 531–534, July 1975.
- [116] P. Lalanne, W. Yan, K. Vynck, C. Sauvan, and J.-P. Hugonin, “Light Interaction with Photonic and Plasmonic Resonances,” *Laser & Photonics Reviews*, vol. 12, no. 5, p. 1700113, 2018.
- [117] D. A. Powell, “Resonant dynamics of arbitrarily shaped meta-atoms,” *Physical Review B*, vol. 90, p. 075108, Aug. 2014.
- [118] J. Mäkitalo, M. Kauranen, and S. Suuriniemi, “Modes and resonances of plasmonic scatterers,” *Phys. Rev. B*, vol. 89, 2014.
- [119] P. Ylä-Oijala, J. Lappalainen, and S. Järvenpää, “Characteristic Mode Equations for Impedance Surfaces,” *IEEE Transactions on Antennas and Propagation*, vol. 66, pp. 487–492, Jan. 2018. Conference Name: IEEE Transactions on Antennas and Propagation.
- [120] D. J. Bergman and D. Stroud, “Theory of resonances in the electromagnetic scattering by macroscopic bodies,” *Physical Review B*, vol. 22, no. 8, p. 3527, 1980.
- [121] C. Forestiere and G. Miano, “Material-independent modes for electromagnetic scattering,” *Phys. Rev. B*, vol. 94, p. 201406, Nov. 2016.
- [122] C. Forestiere, G. Miano, G. Rubinacci, A. Tamburrino, R. Tricarico, and S. Ventre, “Volume Integral Formulation for the Calculation of Material Independent Modes of Dielectric Scatterers,” *IEEE Transactions on Antennas and Propagation*, vol. 66, no. 5, pp. 2505–2514, 2018.
- [123] D. R. Fredkin and I. D. Mayergoyz, “Resonant Behavior of Dielectric Objects (Electrostatic Resonances),” *Physical Review Letters*, vol. 91, p. 253902, Dec. 2003.
- [124] L. Hung, S. Y. Lee, O. McGovern, O. Rabin, and I. Mayergoyz, “Calculation and measurement of radiation corrections for plasmon resonances in nanopar-

- ticles,” *Physical Review B*, vol. 88, p. 075424, Aug. 2013. Publisher: American Physical Society.
- [125] R. Yu, L. M. Liz-Marzán, and F. J. G. d. Abajo, “Universal analytical modeling of plasmonic nanoparticles,” *Chemical Society Reviews*, vol. 46, pp. 6710–6724, Nov. 2017. Publisher: The Royal Society of Chemistry.
- [126] W. Wang, T. Christensen, A.-P. Jauho, K. S. Thygesen, M. Wubs, and N. A. Mortensen, “Plasmonic eigenmodes in individual and bow-tie graphene nanotriangles,” *Scientific Reports*, vol. 5, p. 9535, Apr. 2015. Number: 1 Publisher: Nature Publishing Group.
- [127] R. Yu, J. D. Cox, J. R. M. Saavedra, and F. J. García de Abajo, “Analytical Modeling of Graphene Plasmons,” *ACS Photonics*, vol. 4, pp. 3106–3114, Dec. 2017. Publisher: American Chemical Society.
- [128] I. Silveiro, J. M. P. Ortega, and F. J. G. d. Abajo, “Plasmon wave function of graphene nanoribbons,” *New Journal of Physics*, vol. 17, p. 083013, Aug. 2015.
- [129] Q. Zhan, “Cylindrical vector beams: from mathematical concepts to applications,” *Advances in Optics and Photonics*, vol. 1, pp. 1–57, Jan. 2009. Publisher: Optica Publishing Group.
- [130] Y. V. Morozov and M. Kuno, “Optical constants and dynamic conductivities of single layer MoS₂, MoSe₂, and WSe₂,” *Applied Physics Letters*, vol. 107, p. 083103, Aug. 2015. Publisher: American Institute of Physics.
- [131] U. Wurstbauer, B. Miller, E. Parzinger, and A. W. Holleitner, “Light–matter interaction in transition metal dichalcogenides and their heterostructures,” *Journal of Physics D: Applied Physics*, vol. 50, p. 173001, Mar. 2017. Publisher: IOP Publishing.
- [132] J. Stratton, I. Antennas, and P. Society, *Electromagnetic Theory*. An IEEE Press classic reissue, Wiley, 2007.
- [133] P. Debye, “Der lichtdruck auf kugeln von beliebigem material,” *Annalen der physik*, vol. 335, no. 11, pp. 57–136, 1909.
- [134] A. Doicu, T. Wriedt, and Y. A. Eremin, *Light Scattering by Systems of Particles: Null-Field Method with Discrete Sources: Theory and Programs*. Springer Series in Optical Sciences, Berlin Heidelberg: Springer-Verlag, 2006.

- [135] S. Brenner and R. Scott, *The Mathematical Theory of Finite Element Methods*. Springer Science & Business Media, Dec. 2007. Google-Books-ID: kGFW2uWYU0YC.